1 Polarization dynamics in mode-locked fiber lasers

S. V. Sergeyev, C. Mou, H. Kbashi, S.A. Kolpakov

Contents

1.1 INTRODUCTION

Dissipative vector solitons (DVSs) in mode-locked fiber lasers compose a train of stabilized ultrashort pulses with the specific shape and state of polarization (SOP) driven by a complex interplay between the effects of gain/loss, dispersion, nonlinearity, and linear and circular birefringence (Grelu 2012, Haus 1999, S. C.-C. Cundiff 1999, L. T. Zhao 2008, Zhang 2009, Tang 2008, S. V. Sergeyev 2014, Mou 2011, Boscolo 2014, S. Sergeyev 2014). Given the SOP of the solitons can be locked or evolved at different time scales, the DVSs stability is an important issue to be addressed in the context of applications in metrology (Udem 2002, X. L. Zhao 2018, Pupeza 2021), spectroscopy (Mandon 2009, Picqué 2019) and high-speed fiber-optic communication (Hillerkuss 2011, Geng 2022). Also, the flexibility in the control of dynamic SOPs is of interest for trapping and manipulation of atoms and nanoparticles (Jiang 2010, Tong 2010, Spanner 2001, MacPhail-Bartley 2020, Misawa 2016), and control of magnetization (Kanda 2011, Kimel 2019).

The stability and evolution of vector solitons at a time interval from a few to thousands of

cavity round trips is defined by asymptotic states (attractors) which the laser SOP approaches at a long time scale, *viz.* fixed point, periodic, quasi-periodic, and chaotic dynamics. High signal-to-noise ratio (>40dB) measurement in the case of mode-locked lasers and application of a polarimeter, gives an opportunity for direct observation of attractors embedded in 3D space in terms of the Stokes parameters S_1, S_2, and S_3 (S. Sergeyev 2014, S. V. Sergeyev 2014, Mou 2011). In this section, we review our recent experimental study of the single soliton polarization dynamics in Er-doped mode-locked fiber lasers at time scales from one to a hundred thousand roundtrips. To characterize the dynamics theoretically, we review our new vector model in sections 1.9-1.11.

1.2 FUNDAMENTAL SOLITON POLARIZATION DYNAMICS (EXPRIMENT)

1.2.1 Experimental set-up

Figure 1.1a illustrates the Er-doped fiber laser (EDFL) mode-locked by the carbon nanotubes (CNT) saturable absorber (SA). The EDFL gain medium has of 2 m of high-concentrated Er-doped fiber (EDF Er80-8/125 from Liekki) which is pumped by 980 nm laser diode (LD) through 980nm/1550nm wavelength division multiplexing (WDM). The external and in-cavity polarization controllers are used to adjust the pump wave and lasing states of polarization. An optical isolator (OISO) provides a unidirectional lasing signal propagation in the laser cavity. The output coupler (OUTPUT C) redirects of 10 % of light outside the cavity. The total length of the laser cavity is 7.83 m with an average anomalous dispersion (group velocity dispersion (GVD) parameter for erbium fiber $\beta_{2,EDF}$=*-19.26 fs^2 /mm*) that will result in soliton output. To characterize the output lasing, auto-correlator (Pulsecheck), oscilloscope (Tektronix), optical spectrum analyzer (ANDO AQ6317B), and in-line polarimeter (Thorlabs, IPM5300) are used.

The EDFL is pumped at 178mW that resulting in 3mW of averaged lasing power.

Figure 1.1b shows an output optical spectrum of the output lasing signal centered at 1560 nm and having a full-width half-maximum (FWHM) spectral bandwidth of 3.72 nm. The Kelly sidebands indicate the fundamental soliton shape of the output pulses. A pulse train has a period of 38.9 ns or the repetition rate of 25.7 MHz (Figure 1.1c). The measured autocorrelation trace corresponding to the pulse duration of 583 fs is shown in Figure 1.1d.

<Figure 1.1 here>

Figure 1.1. Experimental set-up. EDF: high concentration erbium-doped fiber, SM: single-mode fiber with anomalous dispersion, POC: polarization controller, WDM: a wavelength division multiplexing coupler, OISO: an optical isolator, CNT: a fast saturable absorber (carbon nanotubes), OUTPUT C: an output coupler, AC; autocorrelator, OSA: optical spectrum analyzer, PD: photodetector, OSC: oscilloscope, ESA: electrical spectrum analyzer, IPM: inline polarimeter. (Adapted from Sergeyev, Sergey V., Mou, Ch., Turitsyna, E.G., Rozhin, A., Turitsyn, S.K. and Blow, K. 2014. "Spiral attractor created by vector solitons." Light: Science & Applications 3(1): e131-e131.)

The polarimeter has a resolution of 1 μs and a measurement interval of 1 ms (25 – 25000 round trips) and detects the normalized Stokes parameters s_1, s_2, s_3 and the degree of polarization (DOP) which are to the output powers of two linearly cross-polarized SOPs, $|u|^2$ and $|v|^2$, and the phase difference between them $\Delta\phi$:

$$S_0 = |u|^2 + |v|^2,\ S_1 = |u|^2 - |v|^2,\ S_2 = 2|u||v|\cos\Delta\varphi,\ S_3 = 2|u||v|\sin\Delta\varphi,$$

$$s_i = \frac{S_i}{\sqrt{S_1^2+S_2^2+S_3^2}},\quad DOP = \frac{\sqrt{S_1^2+S_2^2+S_3^2}}{S_0}, (i = 1,2,3) \qquad (1.1)$$

1.2.2 Experimentally observed fundamental soliton's polarization attractors

By adjusting in-cavity and pump polarization controllers, we observed vector solitons with SOPs slowly evolving at the surface of the Poincare sphere on a double spiral trajectory (Figure 1.2a). The slow dynamics includes residence near the orthogonal states of polarization for approximately 200 μs and relaxation oscillations with a period of about 8 μs. This new type of vector soliton, *viz.* polarization precessing vector soliton, has a spiral structure quite similar to the attractors demonstrated theoretically for dye laser (S. Sergeyev 1999), vertical-cavity semiconductor laser (Willemsen 2001), and degenerate two-level optical medium (Byrne 2003).

By tuning the intra-cavity and pump LD polarization controllers, we have also observed a polarization attractor in the form of a fixed point shown in Figure 1.2b that corresponds to the polarization locked vector soliton with a very high degree of polarization of 92% (Mou 2011) .

By increasing the pump current to 330 mA and tuning the polarization controllers, we have also found a new polarization attractor in the form of a double semi-circle (Figure 1.2c). In view of polarimeter's photodetector resolution of 1 μs this attractor is a results of the signal dynamics averaging over 25 round trips.

<Figure 1.2 here>

Figure 1.2. Polarization attractors at the Poincaré sphere: a) spiral attractor; b) locked SOP; c) double arc. Parameters: time frame of 25-25000 round trips (1 μs – 1 ms); a), b) Pump current I_p*=310 mA;* c) I_p*=330 mA* (Sergeyev, Sergey V., Mou, Ch., Turitsyna, E.G., Rozhin, A., Turitsyn, S.K. and Blow, K. 2014. "Spiral attractor created by vector solitons." Light: Science & Applications 3(1): e131-e131).

1.3 VECTOR MULTIPULSING SOLITON DYNAMICS (EXPERIMENT)

By tuning an in-cavity polarization controller (POC) and POC for the pump laser (Fig. 1 a), we have found a new type of vector solitons with precessing SOPs for multipulsing operations at a time scale of 25-25000 roundtrips (S. V. Sergeyev 2012). In addition to slow polarimeter IPM5300 with 1 μs resolution we used a fast polarimeter inline polarimeter (OFS TruePhase® IPLM)[13] optimized for the high-speed operation (Fig. 3) (Tsatourian V 2013). The polarimeter comprises four tilted fiber gratings (TFBGs) inscribed in the core of polarization-maintaining (PM) fiber. Each TFBG scatters 1% of incoming light on the detector and four detectors' voltages were recorded simultaneously by oscilloscope (Tektronix DPO7254). The polarimeter has 3 dB bandwidth of 550 MHz with a maximum DOP error of around ±4%. Self-calibration procedure has been used to convert the detectors signals voltage to Stokes parameters.

<Figure 1.3 here>

Figure 1.3. Inline polarimeter: OFS TruePhase® IPLM. (Tsatourian V, Sergeyev, S.V., Mou, C., Rozhin, A., Mikhailov, V., Rabin, B., Westbrook, P.S. and Turitsyn, S.K. 2013. "Polarisation dynamics of vector soliton molecules in mode locked fibre laser." Scientific reports 3(1): 1-8.)

In the experiment, the pump current has been changed from 306 mA to 355 mA, and the in-cavity polarization and pump polarization controller have been adjusted. All auto-correlation traces have been averaged over 16 samples to mitigate the auto-correlator sensitivity to the input SOP.

With the pump current of 306 mA, double-pulsing was observed (Figure 1.4a-f). The output optical spectrum shown in Figure 1.4a is centered at 1560 nm with Kelly sidebands indicating the fundamental soliton shape. The pulses doubling shown in Figure 1.4b is the result of the interplay between the laser cavities' bandwidth constraints and the energy quantization associated with the

resulting mode-locked pulses (F. W. Li 2010). With increased pump power, the peak power increases, and the pulse width (inversely proportional to the spectral bandwidth) decreases according to the are theorem (F. W. Li 2010). The increase in the mode-locked spectral bandwidth is limited by the gain bandwidth of the cavity. This constraint can be overcome by a further single pulse split into two pulses with energy divided between two pulses within the gain bandwidth. Given this, a double pulsing with the period T=38.9 ns, pulse width T_p=247 fs, and output power I≈ 0.55 mW was observed (Figure 1.4b). Averaging over 16 auto-correlation traces is enough to obtain a smooth soliton autocorrelation trace (Figure 1.4c). The slow dynamics recorded by IPM5300 polarimeter demonstrates that the anti-phase dynamics of oscillations for two cross-polarized SOPs lead to cw operation for the total output power (Figure 1.4d). The low value of DOP oscillations at 12 % indicate that polarization dynamics is faster than the polarimeter's resolution of 1 μs (Figure 1.4 e). The residual trace of the fast oscillations in Figure 1.4e takes the form of the fast phase difference jumps and so polarization attractor at the Poincaré sphere has a polyline shape winding around a circle (Figure 1.4f).

<Figure 1.4 here>

Fig. 4 Vector soliton with a slowly evolving state of polarization for two-pulse operation. (a) output optical spectrum, (b) single pulse train, (c) measured autocorrelation trace. Polarization dynamics in the time frame of 25-25 000 round trips (1 μs – 1 ms) in terms of (d) optical power of orthogonally polarized modes I_x (solid line) and I_y (dashed line), total power $I=I_x+I_y$ (dotted line), (e) phase difference and degree of polarization, and (f) Stokes parameters at Poincaré sphere. Parameters: pump current I_p=306 mA, period T=38.9 ns, pulse width T_p=247 fs, output power I≈ 0.55 mW.

When the pump power current of 320 mA, the optical spectrum shown in Figure 1.5a preserves the soliton shape and five-pulse soliton dynamics with period T=38.9 ns, pulse width T_p=292 fs, output power I≈ 0.65 mW emerges (Figure 1.5b). As follows from Figure 1.5c, the fast dynamics of the output SOP results in nonsmoothed autocorrelation trace even after averaging over 16 samples. Given the powers of two cross-polarized SOPs slightly deviate from the anti-phase dynamics, the total output power is oscillating with a small amplitude (Figure 1.5d). Similar to the previous case (Figure 1.4e), DOP is oscillating around the low value of 30 % that also indicates the presence of fast SOP oscillations faster than 1 μs that can be also justified by phase difference dynamics (Figure 1.5e). Combination of the fast dynamics in the form of the phase jumps between cross polarized SOPs and slow SOP evolution takes the form of a polyline with an outline in the form of a circle at the Poincaré sphere (Figure 1.5f).

<Figure 1.5 here>

Fig. 5 Vector soliton with slowly evolving state of polarization for five-pulse operation. (a) output optical spectrum, (b) single pulse train, (c) measured auto-correlation trace. Polarization dynamics in the time frame of 25-25 000 round trips (1 μs – 1 ms) in terms of (d) optical power of orthogonally polarized modes I_x (solid line) and I_y (dashed line), total power $I=I_x+I_y$ (dotted line), (e) phase difference and degree of polarization, and (f) Stokes parameters at Poincaré sphere. Parameters: pump current I_p=320 mA, period T=38.9 ns, pulse width T_p=292 fs, output power I≈ 0.65 mW.

In this experiment with the fast polarimeter, OFS TruePhase® IPLM, the pump current was 355 mA, and the in-cavity polarization and pump polarization controllers have been tuned to obtain the polarization attractors shown in Figure 1.6. The two-pulses polarization dynamics shown in Figure 1.6a,b takes the form of polarization switching between cross polarized SOPs with the period equal to the pulse round trip in the laser cavity. A four-pulse soliton operation is shown in Figure 1.6c,d. The polarization dynamics shown in Figure 1.6d demonstrates slow pulse-to-pulse evolution of the laser SOP with the period of 335 ns corresponding to 8 round trips of the laser cavity. Unlike the previous case, the vector soliton shown in Figure 1.6d demonstrates slow cyclic SOP evolution with the circle trajectories at the Poincaré sphere (Figure 1.6d). It has been also found for two cases that DOP is oscillating around 90% that indicates the SOPs of the two adjacent pulses within one round trip are the same (Tsatourian V. 2013).

<Figure 1.6 here>

Figure 1.6. Vector soliton for two- (a, b) and four-pulse (c, d) operation. (a, c) pulse train collected from four polarimeter photodetectors, (b, d) polarization attractors at Poincaré sphere.

1.4 POLARIZATION DYNAMICS OF BOUND STATE SOLITONS (EXPERIMENT)

Unlike multipulsing with the pulse separation of nanoseconds, the bound states originate from short-range interaction through the overlapping of solitons tails or soliton-dispersive wave interaction results and results in double pulses with the spacing of the few pulse widths and phase differences of $0, \pi$ or $\pm \pi/2$. The tightly BS solitons have been experimentally observed in fiber

lasers with different mode-locking techniques including nonlinear polarization rotation (Wang 2020), figure-of-eight (Seong 2002), carbon nanotubes (CNT) (Mou Ch. 2013, Tsatourian V 2013, Wu 2011, Gui 2013) and graphene based mode locked fiber lasers (X. L. Li 2012) . In addition, various types of different bound states have been studied theoretically and experimentally including vibrating bound states, oscillating bound states (Soto-Crespo 2007) bound states with flipping and independently evolving phase (Zavyalov 2009, Ortac 2010). Stable bound states – soliton molecules can be used for coding and transmission of information in high-level modulation formats when multiple bits are transmitted per clock period, increasing capacity of communication channels beyond binary coding limits (Rohrmann 2012). In this section, we review our recent experimental results on a new type BS solitons, namely vector BS soliton with evolving states of polarization (Mou Ch. 2013, Tsatourian V 2013). All results are obtained based on slow (IPM5300) and fast inline polarimeters.

The BS solitons with different pulse separation and a phase shift can be found from optical spectra analysis. For two-soliton BS with pulse separation τ and a phase shift φ, the amplitude takes the form $f(t) + f(t+\tau)\, exp(\, i\varphi)$ and so the optical spectral power can be found as follows (Tsatourian V 2013):

$$S(\nu) = |F(\nu) + F(\nu)\, exp(-i2\pi[\tau\nu + \varphi])|^2 = 2|F(\nu)|^2(1 + cos(2\pi\nu\tau - \varphi)), \quad (1.2)$$

Here $F(\nu) = FFT\big(f(t)\big)$ is the Fourier transform. The results are found in Figure 7a-d. As follows from Figure 1.7a-d, the optical spectrum is modulated with the frequency $\Delta\nu = 1/\tau$, symmetry of spectrum depends on the phase shift, and the minimum of the spectral power is zero. Though some authors associate the loss of spectral fringes' contrast with so-called vibrating solitons (Soto-Crespo 2007), the interleaving of two two-pulse bound states with the phase shifts (0 and $-\pi/2$ or π and $\pi/2$) supported by harmonic mode locking can lead to reduced fringes' contrast (Figure 1.7

e, f (Tsatourian V 2013)). For anomalous dispersion, pulse shape is a hyperbolic-secant-squared with the time-bandwidth product of 0.315. So, the pulse width ΔT and separation τ can be found from an optical spectrum as follows

$$\Delta T = \frac{0.315 n \lambda^2}{c \Delta \lambda}, \quad \tau = \Delta T / N. \tag{1.3}$$

Here *n=1.44* is a refractive index of silica fiber, λ is the central wavelength in optical spectrum, *c* is the speed of light, and *N* is the number of minima in optical spectrum.

<Figure 1.7 here>

Figure 1.7. Spectra of two-soliton bound states with phase shift of: (a) 0, (b) π, (c) , $-\pi/2$, (d) $\pi/2$; (e, f) interleaving of two-soliton bound states with phase shifts of: (e) 0 and $-\pi/2$, (f) π and $\pi/2$.

During the experiment with slow IPM5300 polarimeter, the pump current has been varied from 240 mA to 355 mA while both intra-cavity polarization and pump polarization controllers have been adjusted to reveal polarization attractors shown in Figures 1.8-1.11. To reduce the sensitivity of the auto-correlator to the input SOP, all auto-correlation traces were averaged over 16 samples.

Figure 1.8 shows the experimental results for pump current of 240 mA. The output optical spectrum with fringes shown in Figure 1.8a justifies the formation of a bound state soliton with π phase difference (Mou Ch. 2013). The three-peaks autocorrelation structure shown in Figure 1.8b has the peaks' separation of 2.5 ps that is five times of the pulse duration of 494 fs and so presents the evidence of the tightly bound soliton (Wu 2011). The pulse train with the repetition rate of 25.7 MHz demonstrates that the laser is operating in a fundamental soliton regime (Figure 1.8c). The output power is oscillating with a small amplitude (Figure 1.8 d), the output SOP has the fixed phase difference of 1.125π between x and y SOPs, and oscillating DOP is high of 85% that

indicates the slow polarization dynamics (Figure 1.8e).

<Figure 1.8 here>

Figure 1.8 Polarization locked vector bound state soliton. (a) output optical spectrum, (b) measured auto-correlation trace, (c) single pulse train. Polarization dynamics in the time frame of 25-25 000 round trips (1 μs – 1 ms) in terms of (d) optical power of orthogonally polarized modes I_x (dotted line) and I_y (dashed line), total power $I=I_x+I_y$ (solid line), (e) phase difference and degree of polarization, and (f) Stokes parameters at Poincaré sphere. Parameters: pump current I_p=240 mA, period T=38.9 ns, pulse width T_p=494 fs, output power I= 0.25 mW, phase difference $\Delta\varphi \approx 1.125\pi$.

By tuning the PCs, we achieved bistable operation in the form of switching between bound state soliton (thin lines in Figures 1.9a and 1.9c) with pulse separation of 10 ps and twin pulse operation with separation of few ns (thick lines in Figures 1.9a and 1.9c). For bound state soliton, pulse separation is oscillating and so fringe contrast in Fig. 3(a) is suppressed (Soto-Crespo 2007). For the two-pulse regime, uncorrelated pulses can't produce fringes in optical spectrum (Figure 1.9a). Therefore, we would only see a single peak autocorrelation trace rather than three peaks. As follows from Figs. 1.9c and 1.9d, the pulse period is of 38.9 ns, pulse width of 494 fs and output power of 0.25 mW. Given the pulse separation is more than five times of the pulse width, the BS soliton is loosely BS one (Wu 2011). As shown in Figures 1.9e and 1.9f, the bistable operation results in polarization switching between two cross polarized SOPs related to. loosely bound state and twin pulse.

<Figure 1.9 here>

Figure 1.9 Vector soliton switching between loosely bound state and twin pulse. (a) output optical spectrum of bound soliton (thin solid line) and twin pulse operation (thick solid line), (b) measured auto-correlation trace for bound soliton, (c) single pulse train of bound soliton (dashed line) and twin pulse operation (solid line). Polarization dynamics in the time frame of 25-25 000 round trips (1 μs – 1 ms) in terms of (d) optical power of orthogonally polarized modes I_x (dotted line) and I_y (dashed line), total power $I=I_x+I_y$ (solid line), (e) phase difference and degree of polarization, and (f) normalized Stokes parameters at Poincaré sphere. Parameters: pump current I_p=240 mA, period T=38.9 ns, pulse width T_p=494 fs, output power I≈ 0.25 mW.

In the experiment with the fast OFS TruePhase® IPLM, pump current was about 300 mA, and the in-cavity and pump polarization controllers was adjusted to obtain the polarization attractors shown in Figures 1.10-1.13 (Tsatourian V 2013). Figure 1.10a shows a spectrum of tightly two-pulse bound state soliton with phase shift of π according to Figure 1.7b. The polarization dynamics in Figure 1.10b shows polarization switching between two SOPs with period equal to two round trips.

<Figure 1.10 here>

Figure 1.10 Polarization dynamics of bound state soliton in the form of polarization switching between two orthogonal SOPs. (a) Output optical spectrum indicates π shift bound state with 370

fs pulse width and 1.5 ps pulse separation, (b) Stokes parameters on the Poincaré sphere. Each point in Figure 1.10b corresponds to a single laser pulse.

Pulse width and pulse separation have been found from Equation 1.3 and Figure 1.10a as 370 fs and 1.5 ps. Given the high contrast of spectral fringes in Figure 10a and the pulse separation is less than five pulse widths, BS is a tightly bound soliton having fixed phase shift and pulse separation (Tsatourian V 2013).

<Figure 1.11 here>

Figure 1.11 Polarization dynamics of bound state soliton in the form of polarization switching between three SOPs. (a) Output optical spectrum indicates π shift bound state with 370 fs pulse width and 1.5 ps pulse separation, (b) Stokes parameters on the Poincaré sphere. Each point in Figure 1.11b corresponds to a single laser pulse.

The other type of polarization dynamics of BS soliton is shown in Figure 1.11. The spectra in Figure 1.11a and Figure 1.10a are similar and so BS in Figure 1.11 is a tightly BS soliton with fixed phase shift of π and pulse separation of 1.5 ps (Tsatourian V 2013). The polarization dynamics in Figure 1.11b shows polarization switching between three SOPs with period equal to three round trips. Spectra in Figures 1.10a and 1.11a demonstrate the presence of slight asymmetry that can be caused by hopping between π - and $-\pi/2$-shifted bound states driven by changing the erbium gain spectrum under long-term fluctuations of ambient temperature (Gui 2013). High contrast of fringes and small asymmetry of spectrum justifies that lifetime in π-shifted BS is much longer than lifetime in $-\pi/2$-shifted BS.

<Figure 1.12 here>

Figure 1.12 Polarization dynamics of bound state soliton in the form of superposition of polarization switching between three SOPs and SOP precession. (a) Output optical spectrum indicates $\pi/2$ shift bound state with 370 fs pulse width and 1.5 ps pulse separation; (b) Stokes parameters on the Poincaré sphere. Each point in Figure 1.12b corresponds to a single laser pulse.

Finally, the spectrum in Figure 1.12a demonstrates close to the $-\pi/2$-shifted tightly BS with pulse width of 370 fs and pulse separation of 1.5 ps. The SOP evolution compises a combination of switching between three SOPs with a precession on a circle located on Poincaré sphere with the periods of 3 and 20 round trips (Figure 1.12 b).

<Figure 1.13 here>

Figure 1.13 Polarization dynamics of bound state soliton in the form of superposition popularization switching between two SOPs of two interleaved BSs and SOP precession. (a) Output optical spectrum indicates interleaved BSs with phase shifts of $\pi/2$ and π, 740 fs pulse width and 1.5 ps pulse separation; (b) Stokes parameters on the Poincaré sphere. Each point in Figure 1.13b corresponds to a single laser pulse.

As follows from Figure 1.13a, and Figure 1.7e, the spectrum indicates an interleaving of independent tightly bound states with phase shifts of $\pi/2$ and π. The SOPs of two interleaved

BSs are slightly different and so we have superposition of the SOP switching with cyclic trajectory on the Poincaré sphere with the period of 14 round trips (Figure 1.13b).

1.5 VECTOR SOLITON RAIN (EXPERIMENT)

It was demonstrated in previous sections that short-range interaction through the overlapping of solitons tails or soliton-dispersive wave interaction results in soliton bound states formation with the spacing of the few pulse widths and SOP evolution at different trajectories on the Poincaré sphere (Tsatourian V 2013) . Unlike this, long-range interactions driven, for example, by Casimir-like (Sulimany 2018, Weill 2016) , optoacoustic (Sergeyev S 2021, Liu 2019, Pang 2015) [11-13], and polarization effects [19] can lead to multi-pulsing in the form of harmonic mode-locking (Sergeyev S 2021, Liu 2019, Pang 2015), breathers (Kbashi 2020), and the soliton rain (SR) (Kbashi H.J. 2019, Sulimany 2018, Chouli 2010, Niang 2014).

The SR is a bunch of small soliton pulses randomly distributed and drifting nearby the main pulse and complemented by a continuous wave (cw) background. The SR was studied experimentally and theoretically for different fiber lasers fiber lasers mode-locked based on nonlinear polarization rotation (NPR), nonlinear amplified loop mirror (NALM), the figure of eight cavity, graphene, and single-wall carbon nanotubes (SWCNT) (Kbashi H.J. 2019, Sulimany 2018, Chouli 2010, Niang 2014).

To extend the knowledgebase on SRs, in this section, we review our recent experimental results on the polarization dynamics mediated by the soliton rain evolution in the laser cavity. The mode-locked is slightly different as compared to the laser shown in Fig. 1. Unlike the previous case, it has a 14 m long ring cavity and so a photon round trip time of 70 ns (fundamental frequency of 14.28 MHz). The cavity comprises 13 m of SMF-28 with $\beta_2 = -22\ ps^2 km^{-1}$ and a 1 m of Er-doped fiber (EDF: Liekki Er80-8/125). Instead of using the general approach of splicing fibers in the ring cavity, all the components are attached through APC fiber connectors. The signal was detected by photodetector with a bandwidth of 17 GHz (InGaAsUDP-15-IR-2 FC) connected to a 2.5 GHz sampling oscilloscope (Tektronix DPO7254). An

in-line polarimeter (Thorlabs IPM5300) was used to record the state and degree of polarization (SOP and DOP), respectively.

The results on the fast dynamics are shown in Figure 1.14a-f. The results have been obtained without adjustment of polarization controllers and with changing pump current J as follows: J=220 mA (a, d), 190 ma (b, e), and 260 mA (c, f). As follows from Figure 1.14, the SR takes the forms of the condensed phase (Figure 1.14a, b) and a burst with cw component shown in Figure 1.14c,f.

<Figure 1.14 here>

Figure 1.14. Fast dynamics. Oscillograms (a-c), and corresponding optical spectra (d-f). Parameters: Pump current J=220 mA (a, d); 190 mA (b, e); 260 mA (c, f).

To study the soliton rain pulses' effect on the state of polarization, we use IPM5300 polarimeter to measure the normalized Stokes parameters s_1, s_2, s_3, and degree of polarization (DOP) and to find the output powers of two linearly cross-polarized SOPs I_x, I_y, total power $I = I_x + I_y$ and the phase difference between them $\Delta\varphi$. The results are shown in Figure 1.15a-i. The slow dynamics corresponds to the cases of the fast dynamics, i.e., Figure 1.15a, d, g – to Figure 1.14a, d, Figure 1.15b, e, h – to Figure 1.14b, e, and Figure 1.15c, f, i – to Figure 1.14c, f. As follows from Figure 1.15a,b, spiral attractors can emerge in almost isotropic cavity as a result of polarization symmetry breaking (S. Sergeyev 2014, S. V. Sergeyev 2014). In terms of the dynamics of the cross-polarized modes and the phase difference, the spiral attractor demonstrates the antiphase dynamics of the polarized SOPs the phase difference oscillations and switching between states of $\pi/2$ and $3\pi/2$ (Figure 1.15d,g). The high DOP of about 90% justifies that polarization evolution is can be mapped with 1 ms resolution (Figure 1.15g). Emergence of small repulsing of the SR satellite pulses from the main pulse (Figure 1.14b) results in small modification of polarization dynamics (Figure 1.15b, e, h). The dropped DOP to 80% is a proof that dynamics is faster than 1 ms. With the

increased number and the distance of the satellite pulses from the main pulse (Figure 1.14 c, f), polarization attractor transforms from spiral to circle, as shown in Figure 1.15c. The of x and y SOP are oscillating in antiphase whereas the phase difference dynamics is oscillating between states of $\pi/2$ and $3\pi/2$ (Figure 1.15 f, i). The high DOP of 95% is an indication of slow dynamics with a resolution of 1 ms (Figure 1.15i).

<Figure 1.15 here>

Figure 1.15 Slow polarization dynamics: a)- c) trajectories on the Poincaré sphere.); d) - f) The output power vs time for two linearly cross-polarized SOPs I_x (thin black line) and I_y (grey line) and total power $I=I_x+I_y$ (thick black line); g-f) DOP (black) and the phase difference (grey) vs time. Parameters: Pump current J=220 mA (a, d, g); 190 ma (b, e, h); 260 mA (c, f, i).

The theoretical model for characterization of the vector soliton rain is found in section 1.12.

1.6 VECTOR BRIGHT-DARK ROGUE WAVES (EXPERIMENT)

The extreme events (rogue waves, RWs) can have an anomalously high amplitude and can emerge and disappear unpredictably. The RWs have initially observed in oceanography (Kharif 2008) [1] and further in such fields as financial markets (Yan 2010) [2], nonlinear optics and laser physics (Sergeyev S. 2018, Onorato 2013, Solli 2007, Kbashi H. 2018, Dudley 2014, Akhmediev 2016, Baronio 2012, Chen 2014). To be considered as RWs, extreme events should have probability higher than probabilities for Gaussian or Rayleigh distributions and amplitudes more than twice as large as the significant wave height (SWH). The SWH was initially defined as the mean amplitude of the highest third of the waves (Kharif 2008) and, at present, it is more common to use SWH definition as amplitude equals to the four times of the standard deviation of the amplitude's variations (Onorato 2013).

The scarcity of RWs and the inability to perform full-scale experiments in real-world scenarios are the major obstacles for developing techniques for RWs prediction and mitigation. Given mode-locked fiber lasers (MLFLs) ability to generate pico- and femtosecond pulses with MHz repetition rates, more data on rogue waves in the short time (compared to the time scale of RWs in other systems, such as in the ocean and financial market **(Kharif 2008, Yan 2010)**) can be collected under laboratory-controlled conditions . Previously it has been found that RW can emerge in mode-locked lasers in the form of the soliton rain at the time scale of a round-trip time (Sergeyev S. 2018, Onorato 2013, Solli 2007, Kbashi H. 2018, Dudley 2014, Akhmediev 2016).

All of the above experimental observations report the existence of either bright or dark rogue waves. The co-existence of the bright-dark rogue waves (BDRWs) has been predicted theoretically using coupled nonlinear Schrödinger equation (NLSE) systems (Baronio 2012, Chen 2014), but has never been observed experimentally in optics. In this section, we review our experimental results on a new mechanism of bright-dark rogue wave caused by desynchronization of the linear states of polarizations (SOPs) (Sergeyev S. 2018, Kbashi H. 2018).

Unlike the previous design, an Er-doped fiber laser mode-locked by CNT comprises 1.1m long Er-doped fiber (EDF) with absorption of 80dB/m at 1530nm and the group velocity dispersion (GVD) of +59 ps^2/km. A standard 70:30 output coupler (OUTPUT C) redirected of 30% of the laser light out of the cavity. Also, the laser cavity has 1.22m of OFS980 fiber and 4.4m of SMF 28 fiber with the GVD of -0.04 ps^2/nm. The POC1 and POC2 have been adjusted to find conditions for RWs emergence. To find the probability distribution histograms, the output voltage V for oscilloscope and output power for polarimeter is normalized as $V_n=(V-\text{median}(V))/\sigma(V)$, and so the RW criterion looks as $V_n > 8$.

To eliminate the soliton-soliton and soliton-dissipative wave interactions at the fast (round-trip time) scale, we decreased the pump power P=18.4 mW and tuned POC1 and POC2 to suppress soliton rain. As a result, we observed the dark-bright rogue waves as shown in Figure 1.16a-d. Unlike the previous cases shown in Figures 1.14 and 1.15, the output power is randomly changing from pulse to pulse (Figure 16a, d)) and is satisfying the BDRWs criteria (Figure 1.16c). The slow polarization dynamics measured by IP5300 is shown in Figure 1.17a-c. As follows from the Figure 1.17a, b, the anomalous spikes in the output power satisfy the RWs criteria and are accompanied by transitions between orthogonally polarized SOPs, i.e. the phase difference jumps in π (Figure 1.17a, b). Thus, the experimental data demonstrate BDRWs appearance at the fast (round trip scale) and slow (tens of thousands of round trips) time scales for P=18.4 mW.

<Figure 1.16 here>

Figure 1.16 Laser dynamics demonstrating the emergence of the bright-dark rogue waves at pump power of 18.4 mW. (a) oscilloscope traces (32 GHz resolution); (b) Spatio-temporal dynamics (roundtrip time vs a number of round trips); (c) PDF histogram; d) part of the oscillogram demonstrating the absence of the soliton rain.

<Figure 1.17 here>

Figure 1.17 Polarization laser dynamics at the time scale of tens of thousands of round trips. a) – c) polarization measurements (1 μs resolution, i.e. averaging over approximately 33 round trips, 16 slices with 1024 points per slice): a) the output power vs time (blue) and the phase differences (red); and b) trajectories in normalized Poincaré sphere. c) Probability distribution histogram for the total output power $I=I_x+I_y$. The output power I is normalized as shown in Fig.1. Parameters: a) – c) P=18.4 mW.

The mechanism of BDRWs emergence based on desynchronization of orthogonally polarized SOPs is justified in the section 1.13 with the help of new vector model which is different from the previously developed models based on coupled Schrödinger or Ginzburg-Landau equations (Sergeyev S. 2018, Kbashi H. 2018).

1.7 VECTOR RESONANCE MULTIMODE INSTABILITY (EXPERIMENT)

Modulation instability (MI) is a mechanism driving the emergence of spatial and temporal patterns in fluids, granular media, plasma, nonlinear optics and lasers (Tlidi 2014, Agrawal 2013, Zakharov 2009, Benjamin 1967, Faraday 1831, Szwaj 1998, Turitsyna 2013, Onorato M. 2009, Perego 2016). One of the MI cases, the Benjamin-Feir instability (BFI), is related to the origin of the structures with the wave numbers k and $-k$ due and their synchronization with homogeneous mode of $k=0$ trough nonlinearity (Tlidi 2014, Benjamin 1967). For Faraday instability, emerging spatial structures are result of an external uniform modulation (Tlidi 2014, Faraday 1831). The other type of MI, namely dissipative parametric instability (DPI) (Perego 2016), is driven by periodic antiphase modulation of spectrally dependent losses towards formation of stable one- and two-dimensional patterns. Unlike MI, the main feature of multimode Risken-Nummedal-Graham-Haken (RNGH) instability is the presence of the second lasing threshold exceeding the first in nine times in terms of the pump power (Risken 1968, Graham 1968). For the pump power above the second threshold, excitation of the large number of the longitudinal spatial modes leads to generating the pulse train with period of the cavity round-trip time. Since 1968, when RNGH instability was discovered, it was found that a new second lasing threshold is close to the first threshold for Er-doped fiber lasers (Fontana 1995, E. B. Pessina 1997, E. P. Pessina 1999, Voigt 2004, Lugiato 2015). Also, it was recently found that with accounting for the vector nature of the fiber laser dynamics a new type of RNGH instability, vector resonance multimode instability (VRMI), can emerge (Sergeyev S.V. 2017). In this section, we review our recent results on VRMI (Sergeyev S.V. 2017). The increased in-cavity birefringence strength causes spatial SOP modulation of the in-cavity lasing field (with a period of the beat length) and emergence of the additional satellite

frequencies with the frequency splitting proportional to the birefringence strength. When the splitting is approaching the frequency difference between the longitudinal modes, parametric resonance results in longitudinal modes synchronization and locking similar to the injection locking (S. Y. Cundiff 2003). In the experiments, the special laser configuration exclude mode locking based on nonlinear polarization rotation (Lee 2010).

Unlike the previous laser setups, the schematic in Figure 1.18a includes 1m of Er-doped fiber (Liekki Er80-8/125) and 614m of single mode fiber SMF-28. The 80/20 fiber coupler was used to redirect the part of the signal outside the cavity. The cavity was pumped via a 1480/1550 WDM by using a 1480 nm laser diode (FOL14xx series) with an in-built isolator. The first lasing threshold for the continuous wave (CW) regime was found for 16 mW pump power whereas the second threshold of the multimode instability was for 18 mW. The angles of the orientations of the paddles of POC1 and POC2 (θ_1 and θ_2) were measured from the vertical position. The θ_1=-59^0 whereas θ_2 was set at four different positions θ_2=-80^0,-78^0,-74^0,-69^0.

The results for polarization dynamics are shown in Figure 1.18b, c. As follows from the Figure 1.18b, decreasing the size of the spot by adjusting θ_2 indicates that N-fold beat length is converging to the cavity length. As follows from Figure 1.18c, small oscillations of the output power S_0 and the phase difference $\Delta\varphi$ and small DOP of 40% justifies that the laser dynamics is faster than 1 μs for POC2 setting at θ_2=-80^0. The further tuning the POC2 from θ_2=-78^0 to θ_2=-69^0 demonstrates the constant outputs and high (over 80%) DOP results in stable mode and SOP locking caused by matching N-fold beat length to the cavity length.

Adjustment of the in-cavity polarization controller was resolved better in the case of 1000th harmonic and so the radiofrequency (RF) spectrum evolution was recorded for frequencies of around 325.2 MHz (Figure 1.19a1-d1). The RF spectrum in Figure 1.19a1-d1 has three types of peaks, including the 1000th harmonic (central peak), two satellites adjustable with the help of the POC2 and two close peaks closely position of which is independent on POC2 adjustment. The origin of the satellite frequencies is discussed further in the theoretical part. As follows from Fig.

19 (a2-d2), the adjustment of POC2 results in regime stabilization similar to mode-locking when satellite frequencies match the main line (Fig. 19 (d2)). For RHGM instability, two-mode operation is oscillations close the harmonic with the photon round trip time period (Fontana 1995, E. B. Pessina 1997, E. P. Pessina 1999, Voigt 2004, Lugiato 2015). Unlike this, as follows form Figure 1.19d2, the pulse width is of 40 ns vs the round-trip time of 3 μs. So, many longitudinal modes are phase synchronized (Sergeyev S.V. 2017).

<Figure 1.18 here>

Figure 1.18 (a) Erbium doped fiber laser. EDF: erbium-doped fiber; LD: l480 nm laser diode for pump; POC1 and POC2: polarization controllers, OISO: optical isolator; WDM: wavelength division multiplexer (WDM), OUTPUT C: 80:20 output coupler. (b) The map of the states of polarization on the Poincaré sphere (b) output power (S_0) (c left) and corresponding phase difference between linearly polarized modes and DOP (c right) for different setting of the POC2: θ_2=-80^0, -78^0; -74^0; -69^0.

<Figure 1.19 here>

Figure 1.19 The RF spectrum (a1-d1) and corresponding oscillograms (a2-d2) for different setting of the POC2: a1, a2) θ_2=-80^0; b1, b2) θ_2=-78^0; c1, c2) θ_2=-74^0; d1, d2) θ_2=-69^0.

The theoretical study justifying the vector nature of self-mode-locking is found in section 1.14.

1.8 VECTOR HARMONIC MODE-LOCKING (EXPERIMENTS)

Difficulty of shortening the laser cavity imposes limited by hundreds of MHz repetition rate of mode-locked lasers. The more practical pathway to increase the repetition rate to GHz scale is

harmonic mode-locking (HML) based on resonance with the acoustic phonons (Liu 2019, Pang 2015, Grudinin 1997, Kbashi HJ. 2019, S. K. Sergeyev 2021), four-wave mixing (Quiroga-Teixeiro 1998), pattern-forming modulation instability (Sylvestre 2002) or/and through the insertion of a linear component featuring a periodic spectral transfer function (Peccianti 2012).

<Figure 1.20 here>

Figure 1.20 Acoustic modes in optical fiber core: a) radial mode R_{0m}; b) torsional-radial mode TR_{2m}.

Given the tunable mode-locking with repetition rates up to a few GHz and narrowing the RF line width down to 100 Hz, the resonance of a harmonic of the fundamental frequency with the frequency of a transverse acoustic wave is the most attractive HML technique (Liu 2019, Pang 2015, Grudinin 1997, Kbashi HJ. 2019, S. K. Sergeyev 2021). The pulses propagating in the cavity perturb the fiber's core refractive index and the fiber birefringence that leads to excitation of the radial R_{0m} and torsional-radial TR_{2m} acoustic modes (Figure 1.20a,b; (Shelby 1985, Pilipetskii 1993, Kim 2015). It was found that tuning the in-cavity linear and circular birefringence by using the in-cavity polarization controller enables control of the acoustic modes mediated interaction between the neighbored pulses from attraction to repulsion and the dynamics - from the vector soliton rain to HML driven by TR_{2m} modes (Kbashi H.J. 2019, Kbashi HJ. 2019, Sergeyev S 2021).

In previous section, for the Er-doped fiber laser without a saturable absorber, we demonstrated the mode-locking based on vector resonance multimode instability (VRMI) caused by tuning the birefringence (Sergeyev S.V. 2017). The TR_{2m} modes induces weak oscillations of the fiber birefringence vector orientation (Shelby 1985, Pilipetskii 1993, Kim 2015) and so there is a

challenging task of revealing the interplay between VRMI and TR_{2m} acoustic modes-based perturbation towards HML. In this section, we review our recent experimental results on novel vector HML mechanism caused by interplay of VRMI and TR_{2m} (Sergeyev S 2021). The resonance occurred for the 24th, 38th, and 45th harmonics and resulted in linewidth narrowing below the values reported the other authors (Grudinin 1997).

The setup is shown in Figure 1.21a. The cavity includes 15.8 m of SMF28 and 75 cm of Liekki Er80-8/125 Er-doped fiber with the anomalous dispersion of -20 fs^2/mm. The total length of the cavity is 17 meters. The pump laser diode (FOL14xx series with isolator) with the maximum power of 250 mW is used to pump the laser cavity via WDM coupler. A polarization controller POC1 and an optical isolator for 1560 nm (to improve the laser diode stability) is located between the diode output and the WDM. The output coupler (OUTPUT C) 80:20 redirects the light out of the cavity. After installation of an isolator with 51 dB attenuation, the laser was successfully mode locked. The lasing threshold was measured as 36 mW of the pump power based on linear extrapolation of the signal versus pump power curve (Figure 1.21b). To characterize the polarization laser dynamics, IPM5300 polarimeter is used. Given the absence of a polarizer and the presence of only one polarization controller inside the laser cavity, and low pump powers (less than 200 mW), mode-locking through nonlinear polarization rotation is excluded.

<Figure 1.21 here>

Figure 1.21. Operation of the laser at the fundamental frequency a) Erbium-doped fiber laser. EDF: erbium fiber; LD: l480 nm laser diode for the pump; POC1 and POC2: polarization controllers, OISO: optical isolator; WDM: wavelength division multiplexer (WDM), OUTPUT C: 80:20 output coupler. b) Average laser output power versus pump power; INSET: the RF linewidth

versus pump power (370 Hz at 220 mW pump power). The rectangle indicates the interval where unstable mode-locking patterns have been observed. c) The optical spectrum; inset: the same spectra plotted using a linear scale: 0.2 nm is a bandwidth at 3 dB level. d) The train of pulses at the fundamental frequency, INSET: time-resolved pulse.

The graphs for the output power versus pump power, the emission spectrum, and the pulse train are shown in Figure 1.21b-d. For the pump power above 48 mW, mode-locked pulses emerges with the fundamental repetition rate of 12.21 MHz (Figure 1.21d), RF linewidth 370 Hz (INSET of Figure 1.21b). The transient time for stabilization of this regime varies from a fraction of a second to few minutes. The pulse width of 20 ps (INSET of Figure 1.21d) can't be measured with an auto-correlator and so, to estimate the pulse parameters, we used an ultrafast photodetector XPDV232OR with a bandwidth of 50 GHz and DSO-X93204A oscilloscope with a bandwidth of 32GHz. The pulse width of 20 ps was obtained using the oscilloscope trace and the interpolation software supplied by Agilent that gave us the effective resolution of 781 fs/point (S. K. Sergeyev 2021). The low signal-to-noise ratio (SNR) of 6 dB (Figure 1.21d) reveals the partial mode-locking. The experimental results demonstrate the stable patterns at the fundamental frequency of 12.21 MHz and its high-order harmonics at frequencies of 293.16 MHz, 464.17 MHz, and 549.7 MHz (Table I).

Table 1 Frequencies observed in the experiments

Frequency, MHz.	RF peak width, Hz.	Temporal jitter, ppm[3]	Long term drift
12,21	[210, 370, 530] [1,2]	40	Yes
97.7	Unstable	Unstable	-
207.6	Unstable	Unstable	-
293.16	[9, 38, 155][1]	1.4	Yes

464.17	[22, 38, 150][1]	0.9	Yes
549.7	[1, 13, 97][1]	0.5	Yes
842.5	Unstable	Unstable	-
903.5	Unstable	Unstable	-

[1]Asymmetric interval of confidence 0. 95 [min, mean, max]

[2]At pump power of 220mW

[3] Parts per million with respect to the main value of frequency. The jitter has been quantified using ARIMA (0, 1, 0) (random walk with drift) model with the interval of confidence 0.95.

It has been demonstrated by many authors, that excitation of oscillations at such frequencies is caused by the resonance structure of the spectrum of acoustic phonons excited through the electrostriction effect (Grudinin 1997, Kbashi HJ. 2019, Liu 2019, Pang 2015, Sergeyev S 2021)

The dynamics of the HML at 293.16 MHz is shown in Figure 1.22a-d. A part of the RF spectra is in Figure 1.22a. The lines "A","B" and "C" are related to the 23rd, 24th, and 25th harmonics of the fundamental frequency. We adjusted birefringence by turning the knob of the POC2 and fixed the pump power at 160 mW to clarify evolution of the satellite lines caused by linear and circular birefringence. When the angle of the knob was set between 18 positions, the satellites of the lines “A” and “C” were moving closer to the line "B" as shown in Figure 1.22a. To demonstrate the linewidth compression, we recorded temporal traces and RF spectra for the last four steps 15-18 (Figures 1.22b and 1.22c). For position 15 in Figures 1.22b and 1.22c, the distance between the satellites is slightly less than 3 MHz and the satellites disappears. The RF spectral line corresponds to the fundamental comb frequency with SNR changed from 6 dB to 30 dB for pump power increase from 48 mW to 160 mW. In position 16, the distance between satellites decreases, optical noise spectrum demonstrates a periodic pattern, and the RF spectrum becomes broader. After the knob of POC2 has turned to position 17, the oscilloscope traces (Figure 1.22b, shows oscillations at 293.16 MHz with the period close to 20 ns (50 MHz) and The RF spectrum has multiple peaks.

<Figure 1.22 here>

Figure 1.22. Acousto-optical polarization-dependent locking of a high harmonics a) RF comb showing 24^{th} harmonic along with satellites of 23^{rd}, $24^{th,}$ and 25^{th} harmonics tuning with the help of in-cavity polarization controller POC2. b) Emergence of the 293.16 MHz pulse train for the positions 15, 16, 17, and 18 of the POC2. c) Evolution of the RF spectrum of the 293.16 MHz line for the positions 15, 16, 17, and 18 of the POC2. d) The output SOPs for the POC2 positions 15 and 18 (measurements resolution is 1 μs).

Finally, for the knob position 18, the modulation disappears, and the regular oscillations pattern at the frequency of 293.16 MHz emerges. The RF spectrum shows narrow resonance line with 60 dB SNR and the noise level of -120 dB as shown in Figure 1.22d. The locked SOP for POC2 positions 15 and 18 corresponds to the self-oscillation at the fundamental frequency for position 15 and HML for position 18. The tuning POC2 from position 15 to position 18 changes the linear and circular birefringence in the cavity due to induced fiber squeezing and twist (Collett 2003). As shown in Figure 1.22d, increasing DOP from 62 % to 86% indicates more stable operation for 18^{th} position as compared to the 15th position. By adjusting POC2. HML at different acoustic frequencies is observed as shown in Table 1. In section 1.15, we review our recent theoretical results on novel vector HML mechanism caused by interplay of VRMI and TR_{2m} (Sergeyev S 2021).

1.9 VECTOR MODEL OF ERBIUM DOPED FIBER LASER

1.9.1 Semiclassical equations

To describe vector features of mode-locked erbium doped fiber laser with a carbon nanotube (CNT) as a saturable absorber, we start with the vector semi-classical equations for a unidirectional laser (Fu 1987, S. V. Sergeyev 1996, S. Sergeyev 1999):

$$\frac{\partial E_x}{\partial t} + c\frac{\partial E_x}{\partial z} = -kE_x + ik\int \left(\boldsymbol{e_x P}(g)\right)dg\,,$$

$$\frac{\partial E_y}{\partial t} + c\frac{\partial E_y}{\partial z} = -kE_y + ik\int \left(\boldsymbol{e}_y \boldsymbol{P}(g)\right)dg\,,$$

$$\frac{\partial \boldsymbol{P}(g)}{\partial t} = \left(-\gamma_p + i\Delta_0\right)\boldsymbol{P}(g) - i\gamma_p D(g)\boldsymbol{m_e^*}\left(E_x(\boldsymbol{e_x m}_e) + E_y\left(\boldsymbol{e}_y \boldsymbol{m}_e\right)\right),$$

$$\frac{\partial D(g)}{\partial t} = \gamma_d\left(D_0 - D(g) + \frac{i}{4}\left(\boldsymbol{P}(g)^*\left[E_x \boldsymbol{e_x} + E_y \boldsymbol{e}_y\right] - \boldsymbol{P}(g)\left[E_x^* \boldsymbol{e_x} + E_y^* \boldsymbol{e}_y\right]\right)\right). \quad (1.4)$$

Here ***P(g)*** and *D(g)* are angular distributions for polarization of active medium and normalized gain, $g=(\theta,\varphi,\psi)$ are Euler angles showing the orientation of the local reference frame *(X',Y',Z')* connected to the orientation of the dipole moments of Er^{3+} ion with respect to the laboratory reference frame *(X,Y,Z)* described by the orientation of the cross-polarized components of the electric field $\mathbf{e_x}$ and $\mathbf{e_y}$. So, $\int \ldots dg = (1/8\pi)^2 \int_0^{2\pi}\int_0^{2\pi}\int_0^{\pi} \ldots \sin\theta\, d\theta d\phi d\psi$ (Varshalovich 1988), $\boldsymbol{E}=E_x\boldsymbol{e_x}+E_y\boldsymbol{e_y}$ is a lasing electric field, $\boldsymbol{m_e}$ is a unit vector for the dipole moment of the transition with emission (S. Sergeyev 1999, S. V. Sergeyev 1996), D_0 is the normalized parameter for the pumping light power, Δ_0 is detuning of the lasing wavelength from to the maximum of the gain spectrum, the vector $\mathbf{m_e}^*$ is a vector with complex conjugation of the vector $\mathbf{m_e}$; *k,* γ_p, and γ_d are the relaxation rates for photons in the cavity, medium polarization and gain. Given the relaxation rate of the medium polarization in erbium doped silica matrix $\gamma_p = 4.75 \times 10^{14}\ s^{-1} >> \gamma_d$, *k* ($\gamma_d$=100

s^{-1}, k=10^7 - 10^8 s^{-1}) (Williams 1996) , we can use the following simplification $\partial P(g)/\partial t = 0$ and so the Equation (1.4) takes the following form:

$$\frac{\partial E_x}{\partial t} + c\frac{\partial E_x}{\partial z} = -kE_x + \frac{(1+i\Delta)}{1+\Delta^2}\left(D_{xx}E_x + D_{xy}E_y\right),$$

$$\frac{\partial E_y}{\partial t} + c\frac{\partial E_y}{\partial z} = -kE_y + \frac{(1+i\Delta)}{1+\Delta^2}\left(D_{yx}E_x + D_{yy}E_y\right),$$

$$\frac{\partial D(g)}{\partial t} = \gamma_d\left(D_0 - D(g) - \frac{D(g)}{2}R\left(E_x, E_y, g\right)\right),$$

$$R\left(E_x, E_y, g\right) = \frac{1}{1+\Delta^2}\begin{bmatrix}|E_x|^2|\boldsymbol{e_x m}_e|^2 + \left|E_y\right|^2\left|\boldsymbol{e}_y\boldsymbol{m}_e\right|^2 + \\ E_xE_y^*(\boldsymbol{e_x m}_e)\left(\boldsymbol{e}_y\boldsymbol{m}_y^*\right) + E_yE_x^*\left(\boldsymbol{e}_y\boldsymbol{m}_e\right)(\boldsymbol{e}_x\boldsymbol{m}_e^*)\end{bmatrix}. \quad (1.5)$$

Here $\Delta = \Delta_0/\gamma_p$ and

$$D_{xx} = k\int D(g)|\boldsymbol{e_x m}_e|^2 dg\,, \quad D_{yy} = k\int D(g)\left|\boldsymbol{e}_y\boldsymbol{m}_e\right|^2 dg\,,$$

$$D_{xy} = k\int D(g)\left(\boldsymbol{e}_y\boldsymbol{m}_e\right)(\boldsymbol{e}_x\boldsymbol{m}_e^*)dg, \quad D_{yx} = k\int n(g)(\boldsymbol{e}_x\boldsymbol{m}_e)\left(\boldsymbol{e}_y\boldsymbol{m}_e^*\right)dg \quad (1.6)$$

By adding a saturable absorber (single-wall carbon nanotubes, CNTs), fiber birefringence, Kerr nonlinearity, chromatic dispersion (S. Sergeyev 2014, S. V. Sergeyev 2014), absorption from the ground state at the lasing wavelength for Erbium ions (Desurvire 1994) (Figure 1.23a), and SOP for pump wave, we can modify Equation 1.6 as follows (S. Sergeyev 2014, S. V. Sergeyev 2014) :

$$\frac{\partial E_x}{\partial z} = i\beta E_x - \eta\frac{\partial E_x}{\partial t} - i\beta_2\frac{\partial^2 E_x}{\partial t^2} + i\gamma\left(|E_x|^2E_x + \frac{2}{3}\left|E_y\right|^2E_x + \frac{1}{3}E_y^2E_x^*\right) + D_{xx}E_x + D_{xy}E_y,$$

$$\frac{\partial E_y}{\partial z} = -i\beta E_y + \eta\frac{\partial E_y}{\partial t} - i\beta_2\frac{\partial^2 E_y}{\partial t^2} + i\gamma\left(\left|E_y\right|^2E_y + \frac{2}{3}|E_x|^2E_y + \frac{1}{3}E_x^2E_y^*\right) + D_{yx}E_x + D_{yy}E_y,$$

$$D_{xx} = \frac{\alpha_1}{2}\frac{(1-i\Delta)}{1+\Delta^2}\left[\chi\int n(g)|\boldsymbol{e_x m}_e|^2 dg - 1\right] - \alpha_2\int N(g)|\boldsymbol{e_x\mu}_a|^2 dg - \alpha_4,$$

$$D_{xy} = \frac{\alpha_1\chi}{2}\frac{(1-i\Delta)}{1+\Delta^2}\int n(g)\left(\boldsymbol{e}_y\boldsymbol{m}_e\right)(\boldsymbol{e}_x\boldsymbol{m}_e^*)dg - \alpha_2\int N(g)\left(\boldsymbol{e}_y\boldsymbol{\mu}_a\right)(\boldsymbol{e}_x\boldsymbol{\mu}_a^*)dg\,,$$

$$D_{yx} = \frac{\alpha_1 \chi}{2} \frac{(1 - i\Delta)}{1 + \Delta^2} \int n(g)(\boldsymbol{e}_x \boldsymbol{m}_e)(\boldsymbol{e}_y \boldsymbol{m}_e^*) dg - \alpha_2 \int N(g)(\boldsymbol{e}_x \boldsymbol{\mu}_a)(\boldsymbol{e}_y \boldsymbol{\mu}_a^*) dg\,,$$

$$D_{yy} = \frac{\alpha_1}{2} \frac{(1 - i\Delta)}{1 + \Delta^2} \left[\chi \int n(g) \left| \boldsymbol{e}_y \boldsymbol{m}_e \right|^2 dg - 1 \right] - \alpha_2 \int N(g) \left| \boldsymbol{e}_y \boldsymbol{\mu}_a \right|^2 dg - \alpha_4,.$$

$$\frac{\partial n(g)}{\partial t} = \gamma_a \left(\frac{I_p}{I_{ps}} \left(1 - n(g)\right) \left| \boldsymbol{e}_p \boldsymbol{m}_a \right|^2 - n(g) - (\chi n(g) - 1) R_{Er}(E_x, E_y, g) \right),$$

$$N(g) = \frac{1}{1 + \alpha_3 R_{CNT}(E_x, E_y, g)(1 + \Delta^2)}$$

$$R_{Er}(E_x, E_y, g) = \frac{1}{1 + \Delta^2} \left[\frac{|E_x|^2}{I_{ss}} |\boldsymbol{e}_x \boldsymbol{m}_e|^2 + \frac{\left|E_y\right|^2}{I_{ss}} \left| \boldsymbol{e}_y \boldsymbol{m}_e \right|^2 + \frac{E_x E_y^*}{I_{ss}} (\boldsymbol{e}_x \boldsymbol{m}_e)(\boldsymbol{e}_y \boldsymbol{m}_e^*) \right.$$

$$\left. + \frac{E_y E_x^*}{I_{ss}} (\boldsymbol{e}_y \boldsymbol{m}_e)(\boldsymbol{e}_x \boldsymbol{m}_e^*) \right],$$

$$R_{CNT}(E_x, E_y, g) = \frac{1}{1+\Delta^2} \left[\frac{|E_x|^2}{I_{ss}} |\boldsymbol{e}_x \boldsymbol{\mu}_a|^2 + \frac{\left|E_y\right|^2}{I_{ss}} \left| \boldsymbol{e}_y \boldsymbol{\mu}_a \right|^2 + \frac{E_x E_y^*}{I_{ss}} (\boldsymbol{e}_x \boldsymbol{\mu}_a)(\boldsymbol{e}_y \boldsymbol{\mu}_a^*) + \right.$$

$$\left. \frac{E_y E_x^*}{I_{ss}} (\boldsymbol{e}_y \boldsymbol{\mu}_a)(\boldsymbol{e}_x \boldsymbol{\mu}_a^*) \right]. \qquad (1.7)$$

<Figure 1.23 here>

Figure 1.23 a) Diagram of energy levels and transitions in Er^{3+} ion: 1 – pimp absorption at 980 nm; 2- fluorescence at 1550 nm; 3 – absorption at 1550 nm; 4 – lasing at 1550 nm; 5, 5' – upconversion (radiationless energy transfer between two excited ions at $^4I_{13/2}$ level, the donor ion is deactivated whereas the acceptor is exited at $^4I_{9/2}$ level); 6, 7 - non-radiative phonon-assisted transitions; 8 – fluorescence at 980 nm. b) The orientation of absorption and emission dipole moments for erbium doped silica ($\mathbf{m_a}$,$\mathbf{m_e}$) and the absorption dipole moment for CNT $\boldsymbol{\mu}_\mathbf{a}$.

Here *n(g)* and *N(g)* are the angular distributions of the erbium ions at the first excited level and CNT in the ground state, α_2 is the CNT absorption at the lasing wavelength, α_3 is the ratio of

saturation powers for CNT and EDF, α_4 represents the normalized losses, β is the birefringence strength ($2\beta=2\pi/L_b$, L_b is the beat length), $\boldsymbol{m_a}$ and $\boldsymbol{\mu_a}$ are unit vectors along the dipole moment of the transition with absorption for erbium ions and CNT, V_g is the group velocity, $\eta=\beta\lambda/(2\pi c)$ is the inverse group velocity difference between the polarization modes, $\alpha_1 = \sigma_a \Gamma_L \rho$ is the EDF absorption at the lasing wavelength, $I_{ps} = \gamma_d A h \nu_p / \left(\sigma_a^{(p)} \Gamma_p\right)$, $I_{ss} = \gamma_d A h \nu_s / \left(\sigma_a^{(L)} \Gamma_L\right)$ are saturation powers for pump and lasing (h is Planck's constant, ν_p, ν_s are pump and lasing frequencies), $\chi = \left(\sigma_a^{(L)} + \sigma_e^{(L)}\right)/\sigma_a^{(L)}$, $\sigma_{a(e)}^{(L)}$, $\sigma_a^{(p)}$ are absorption and emission cross sections at the lasing wavelength and absorption cross section at the pump wavelength, Γ_L and Γ_p are the confinement factors of the EDF fiber at the lasing and pump wavelengths, ρ is the concentration of erbium ions, A is the fiber core cross section area.

1.9.2 Reducing the complexity of the semiclassical model

To simplify description of the polarized lasing field interaction with the gain medium in Equations (1.7), we use an approximation introduced by Zeghlache and Boulnois (Zeghlache 1995) and justified by Leners and Stéphan (Leners 1995), i.e. we suggest that dipole moments ($\mathbf{m_a}$, $\mathbf{m_e}$) and the dipole moment $\boldsymbol{\mu_a}$ are located in the plane defined by the orthogonal components of the lasing field $\boldsymbol{e_x}$ and $\boldsymbol{e_y}$ (Figure 1.23b). In addition, we use the property of Er ions $\boldsymbol{m_a}=\boldsymbol{m_e}$ and consider an elliptically polarized pump $\boldsymbol{e}_p = \left(\boldsymbol{e}_x + i\delta \boldsymbol{e}_y\right)/\sqrt{1+\delta^2}$ (here δ is the ellipticity of the pump wave) as follows (S. Sergeyev 2014, S. V. Sergeyev 2014)

$$\left(\boldsymbol{m}_e \boldsymbol{e}_x\right) = cos(\theta)\,,\ \left(\boldsymbol{m}_e \boldsymbol{e}_y\right) = sin(\theta)\,,\ \left(\boldsymbol{m}_a \boldsymbol{e}_p\right)^2 = \frac{cos(\theta)^2 + \delta^2\, sin(\theta)^2}{1+\delta^2},$$

$$\left(\boldsymbol{\mu}_a \boldsymbol{e}_x\right) = cos(\theta_1)\,,\ \left(\boldsymbol{\mu}_a \boldsymbol{e}_y\right) = sin(\theta_1) \qquad (1.8)$$

So, the angular distributions $n(g)$ now depends only on θ and can be presented by a Fourier series follows (S. Sergeyev 2014, S. V. Sergeyev 2014, Zeghlache 1995):

$$n(\theta) = \frac{n_0}{2} + \sum_{k=1}^{\infty} n_{1k}\cos(k\theta) + \sum_{k=1}^{\infty} n_{2k}\sin(k\theta). \tag{1.9}$$

Substituting Equations (1.9) to Equations (1.4), we find a complete set of equations for E_x, E_y, n_0, n_{12}, n_{22} (S. Sergeyev 2014, S. V. Sergeyev 2014):

$$\frac{\partial E_x}{\partial z} = i\beta E_x - \eta\frac{\partial E_x}{\partial t} - i\beta_2\frac{\partial^2 E_x}{\partial t^2} + i\gamma\left(|E_x|^2 E_x + \frac{2}{3}\left|E_y\right|^2 E_x + \frac{1}{3}E_y^2 E_x^*\right) + D_{xx}E_x + D_{xy}E_y,$$

$$\frac{\partial E_y}{\partial z} = -i\beta E_y + \eta\frac{\partial E_y}{\partial t} - i\beta_2\frac{\partial^2 E_y}{\partial t^2} + i\gamma\left(\left|E_y\right|^2 E_y + \frac{2}{3}|E_x|^2 E_y + \frac{1}{3}E_x^2 E_y^*\right) + D_{yx}E_x + D_{yy}E_y$$

$$D_{xx} = \left(\frac{\alpha_1(1-i\Delta)}{1+\Delta^2}I_{xx}(n_0, n_{12}, n_{22}) - J_{xx} - \alpha_4 L\right), D_{xy} = D_{yx}$$

$$= \left(\frac{\alpha_1(1-i\Delta)}{1+\Delta^2}I_{xy}(n_0, n_{12}, n_{22}) - J_{xy}\right),$$

$$D_{yy} = \left(\frac{\alpha_1(1-i\Delta)}{1+\Delta^2}I_{yy}(n_0, n_{12}, n_{22}) - J_{yy} - \alpha_4 L\right)$$

$$I_{xx}(n_0, n_{12}, n_{22}) = \left(\chi\frac{n_0}{2} - 1\right) + \chi\frac{n_{12}}{2}, I_{yy}(n_0, n_{12}, n_{22}) = \left(\chi\frac{n_0}{2} - 1\right) - \chi\frac{n_{12}}{2},$$

$$I_{xy}(n_0, n_{12}, n_{22}) = \chi\frac{n_{22}}{2},\ J_{xx} = \alpha_2\left(\frac{1}{2} - \alpha_3\frac{1}{8}\left[3|E_x|^2 + \left|E_y\right|^2\right]\right),$$

$$J_{yy} = \alpha_2\left(\frac{1}{2} - \alpha_3\frac{1}{8}\left[|E_x|^2 + 3\left|E_y\right|^2\right]\right),\ J_{xy} = -\frac{\alpha_3\alpha_2}{8}\left[E_x E_y{}^* + c.c.\right],$$

$$\frac{dn_0}{dt} = \gamma_d\left[I_p + 2R_{10} - \left(1 + \frac{I_p}{2} + \chi R_{10}\right)n_0 - \left(\chi R_{11} + \frac{I_p}{2}\frac{(1-\delta^2)}{(1+\delta^2)}\right)n_{12} - \chi n_{22}R_{12}\right],$$

$$\frac{dn_{12}}{dt} = \gamma_d\left[\frac{(1-\delta^2)}{(1+\delta^2)}\frac{I_p}{2} + R_{11} - \left(\frac{I_p}{2} + 1 + \chi R_{10}\right)n_{12} - \left(\frac{(1-\delta^2)}{(1+\delta^2)}\frac{I_p}{2} + \chi R_{11}\right)\frac{n_0}{2}\right],$$

$$\frac{dn_{22}}{dt} = \gamma_d\left[R_{12} - \left(\frac{I_p}{2} + 1 + \chi R_{10}\right)n_{22} - \chi R_{12}\frac{n_0}{2}\right],$$

$$R_{10} = \frac{1}{2(1+\Delta^2)}\left(|E_x|^2 + \left|E_y\right|^2\right), R_{11} = \frac{1}{2(1+\Delta^2)}\left(|E_x|^2 - \left|E_y\right|^2\right), R_{12} = \frac{1}{2(1+\Delta^2)}\left[E_x E_y{}^* + c.c.\right].$$

(1.10)

Here we use approximation $\frac{\alpha_3}{4}\left[3|E_x|^2+\left|E_y\right|^2\right] << 1$. We apply the distributed forms for saturable absorption and losses in Equations (1.10) instead of lumped presentation to simplify consideration. Next, we use approach of averaging over the pulse width to characterize the slow time scale dynamics. We introduce a new slow-time variable $t_s = z/\left(V_g t_R\right)$, where $t_r=L/V_g$ is the photon round-trip time, L is the cavity length) and assume an ansatz in the form (S. Sergeyev 2014, S. V. Sergeyev 2014):

$$E_x(t,t_s) = u(t_s)\, sech(\, t/T_p),\ E_x(t,t_s) = v(t_s)\, sech(\, t/T_p). \tag{1.11}$$

Here T_p is the pulse width. After substitution of Equations (1.11) into Equations (1.10) and averaging over the time $T_p<<t<<t_R$ we obtain the following (S. Sergeyev 2014, S. V. Sergeyev 2014):

$$\begin{gathered}
\frac{du}{dt_s} = i\beta L u + i\frac{\gamma L I_{ss}}{2}\left(|u|^2u+\frac{2}{3}|v|^2u+\frac{1}{3}v^2u^*\right)+D_{xx}u+D_{xy}v,\\
\frac{dv}{dt_s} = -i\beta L v + i\frac{\gamma L I_{ss}}{2}\left(|v|^2v+\frac{2}{3}|u|^2v+\frac{1}{3}u^2v^*\right)+D_{xy}u+D_{yy}v,\\
\frac{dn_0}{dt_s} = \varepsilon\left[I_p+2R_{10}-\left(1+\frac{I_p}{2}+\chi R_{10}\right)n_0-\left(\chi R_{11}+\frac{I_p}{2}\frac{(1-\delta^2)}{(1+\delta^2)}\right)n_{12}-\chi n_{22}R_{12}\right],\\
\frac{dn_{12}}{dt_s} = \varepsilon\left[\frac{(1-\delta^2)}{(1+\delta^2)}\frac{I_p}{2}+R_{11}-\left(\frac{I_p}{2}+1+\chi R_{10}\right)n_{12}-\left(\frac{(1-\delta^2)}{(1+\delta^2)}\frac{I_p}{2}+\chi R_{11}\right)\frac{n_0}{2}\right],\\
\frac{dn_{22}}{dt_s} = \varepsilon\left[R_{12}-\left(\frac{I_p}{2}+1+\chi R_{10}\right)n_{22}-\chi R_{12}\frac{n_0}{2}\right],\\
R_{10}=\frac{1}{(1+\Delta^2)}(|u|^2+|v|^2),\quad R_{11}=\frac{1}{(1+\Delta^2)}(|u|^2-|v|^2), R_{12}=\frac{1}{(1+\Delta^2)}(uv^*+vu^*),
\end{gathered} \tag{1.12}$$

Coefficients D_{ij} can be found as follows:

$$\begin{aligned}
D_{xx} &= \frac{\alpha_1 L(1-i\Delta)}{1+\Delta^2}(f_1+f_2)-\left(\frac{\alpha_2 L}{2}-\frac{2\alpha_2\alpha_3 L}{8\pi}k_1\right)-\alpha_4 L,\\
D_{yy} &= \frac{\alpha_1 L(1-i\Delta)}{1+\Delta^2}(f_1-f_2)-\left(\frac{\alpha_2 L}{2}-\frac{\alpha_2\alpha_3 L}{4\pi}k_2\right)-\alpha_4 L,
\end{aligned}$$

$$D_{xy} = D_{yx} = \frac{\alpha_1 L(1-i\Delta)}{1+\Delta^2} f_3 - \frac{2\alpha_2\alpha_3 L}{8\pi} k_3, \tag{1.13}$$

where:

$$f_1 = \left(\chi \frac{n_0}{2} - 1\right),\ f_2 = \chi \frac{n_{12}}{2},\ f_3 = \chi \frac{n_{22}}{2},$$
$$k_1 = 3|u|^2 + |v|^2,\ k_2 = |u|^2 + 3|v|^2,\ k_3 = uv^* + vu^*. \tag{1.14}$$

Here $\varepsilon = t_R \gamma_d$ and u, v are normalized to the saturation power I_{ss} and I_p is normalized to the saturation power I_{ps}. We have also neglected the inverse group velocity difference of the cross polarized components x and y that corresponds to $\eta \approx 0$. For a cavity length $L_c = 7.8\ m$, beat length $L_b = 5m$, and $\lambda = 1.56$ μm the time delay between cross polarized pulses over the length of the cavity can be found from the notations to Equations (1.9) as $T_d = 8\ fs$. Given the $T_d << T_p$=600 fs and the CNT relaxation time of 300 fs, the group velocity difference can be neglected in Equations (1.9). We have also used the following notations (S. Sergeyev 2014, S. V. Sergeyev 2014)

$$\int_{-T/T_p}^{T/T_p} \frac{cosh(x)^2 - 2}{cosh(x)^3} dx \to 0, \frac{\int_{-T/T_p}^{T/T_p} sech(x^3) dx}{\int_{-T/T_p}^{T/T_p} sech(x) dx} \approx \frac{1}{2}, \frac{\int_{-T/T_p}^{T/T_p} sech(x^2) dx}{\int_{-T/T_p}^{T/T_p} sech(x) dx} \approx \frac{2}{\pi}. \tag{1.15}$$

We have neglected the absorption dynamics in CNT that holds true for saturable absorber relaxation time τ_a is smaller than the pulse width T_p. In our experiments $\tau_a \sim 300\ fs$ and $T_p \sim 600$ fs and so approximation of fast saturable absorber is valid if we make change of variables $\alpha_2 \to \alpha_2(1-exp(-T_p/\tau_a))$ for the case of $\alpha_2 << 1$. Though Er^{3+} ion is usually described as a four-level system in Figure 1.23b, we reduce this model to two-level one by excluding excited state absorption from $^4I_{11/2}$ and population of this level justified for pump powers I_p<200 mW, *viz.* for the case considered in our publications (S. Sergeyev 2014, S. V. Sergeyev 2014). For high concentration Er-doped fiber, Sergeyev and co-workers demonstrated that migration assisted upconversion (MAUP) results in decreasing first excited level lifetime more than 10 times (S. Sergeyev 2003, S. P.

Sergeyev 2006, Sergeyev, S., Popov, S., and Friberg, A.T. 2005) and so decreasing the lifetime at the first excited level is a reliable approach for mimic MAUP (S. Sergeyev 2014, S. V. Sergeyev 2014). Slow MAUP dynamics in microseconds scale has no effect on pulse shape. Unlike previously used models based on either coupled nonlinear Schrödinger or Ginzburg-Landau equations, the Equations (1.12)–(1.14) account for slow polarization dynamics.

To study the evolving SOPs of the vector solitons, we account for birefringence tuning by in-cavity polarization controller. First, we rewrite Equations (1.12) for $\boldsymbol{\Psi} = (u, v)^T$ as

$$\boldsymbol{\Psi}(t_s + 1) = \boldsymbol{B}\, exp(\boldsymbol{G})\ \boldsymbol{\Psi}(t_s), \tag{1.16}$$

where

$$\mathbf{G} = \begin{bmatrix} \int_{t_s}^{t_s+1} D_{xx}(t_s)dt_s & \int_{t_s}^{t_s+1} D_{xy}(t_s)dt_s \\ \int_{t_s}^{t_s+1} D_{xy}(t_s)dt_s & \int_{t_s}^{t_s+1} D_{yy}(t_s)dt_s \end{bmatrix}, \quad \mathbf{B} = \begin{bmatrix} \exp\left(\frac{i\pi L}{L_b}\right) & 0 \\ 0 & \exp\left(-\frac{i\pi L}{L_b}\right) \end{bmatrix}. \tag{1.17}$$

The presence of the in-cavity polarization controller modifies Equations (1.16):

$$\boldsymbol{\Psi}(t_s+1) = \mathbf{T}\,\mathbf{B}\exp(\mathbf{G})\boldsymbol{\Psi}(t_s), \tag{1.18}$$

Where T is the transfer matrix of POC (Heismann 1994)

$$\boldsymbol{T} = \begin{bmatrix} A + iB & C + iD \\ -C + iD & A - iB \end{bmatrix}, A = -cos(\psi_1)\, cos(\psi_2)\,,$$

$$B = -sin(\psi_3)\, sin(\psi_1)\,, C = -cos(\psi_1)\, sin(\psi_2)\,, D = -sin(\psi_1)\, cos(\psi_3)\,,$$

$$A^2 + B^2 + C^2 + D^2 = 1,\ \psi_1 = \zeta - \upsilon - \xi/2, \psi_2 = \xi/2\,, \quad \psi_3 = \xi/2 + \upsilon, \tag{1.19}$$

Here υ/2, ζ/2, and (υ+ξ)/2 are the orientations of the first quarter-wave plate (QWP), half-wave plate and the second QWP at the vertical axis Y.

As follows from Equations (1.17) and (1.18):

$$\mathbf{T_1} = \mathbf{T}\,\mathbf{B}, \mathbf{T}_1 = \begin{bmatrix} A_1 + iB_1 & C_1 + iD_1 \\ -C_1 + iD_1 & A_1 - iB_1 \end{bmatrix},\ A_1^2 + B_1^2 + C_1{}^2 + D_1{}^2 = 1. \tag{1.20}$$

As follows from Equation (1.18), the condition of the SOP reproducibility in *n*-round trips takes the form:

$$(\boldsymbol{T_1}\, exp(\boldsymbol{G}))^n = a\boldsymbol{I},\ \ \boldsymbol{I} = \begin{bmatrix} 1 & 0 \\ 0 & 1 \end{bmatrix},\ |a| = 1, arg(a) = \pi k,\ k = 0,\ 1.. \tag{1.21}$$

If we neglect SOP rotation caused by an active medium, i.e. $exp(\boldsymbol{G})=\boldsymbol{I}$, reproducibility of SOP for two round trips for the condition $A_1=C_1=D_1=0$ and $B_1=1$ means $L_b=2L$ whereas for reproducibility for three round trips for condition $C_1=D_1=0$ results in $A_1=3^{1/2}/2$, $B_1=1/2$, i.e. $L_b=3L$.

To calculate pulse-to-pulse evolution of SOP numerically, we transform Equations (1.18) into the distributed form as follows:

$$\frac{d\Psi}{dt_s} = (G + ln(T_1))\Psi, \tag{1.22}$$

Given the condition $C_1=D_1=0$ for the case of SOP reproducibility in *n*-round trips, Equations (1.22) take the form

$$\frac{d\boldsymbol{\Psi}}{dt_s} = \boldsymbol{G\Psi} + \begin{pmatrix} i\pi L/L_{b1} & 0 \\ 0 & -i\pi L/L_{b1} \end{pmatrix}\boldsymbol{\Psi} + \boldsymbol{NL}, \tag{1.23}$$

Where L_{b1} is the beat length for combined fiber-POC birefringence, **NL** describes contribution of the Kerr nonlinearity as follows:

$$\boldsymbol{NL} = i\frac{\gamma L I_{ss}}{2}\begin{pmatrix} |u|^2u + \frac{2}{3}|v|^2u + \frac{1}{3}v^2u^* \\ |v|^2v + \frac{2}{3}|u|^2v + \frac{1}{3}u^2v^* \end{pmatrix}. \tag{1.24}$$

For an analytical study of SOP evolution, we substitute $\mathbf{\Psi} = \left(|u|\exp(i\phi_x), |v|\exp(i\phi_y)\right)^T$ in Equation (1.23) and find equation for the phase difference $\Delta\varphi = \varphi_x - \varphi_y$

$$\frac{d\Delta\varphi}{dt_s} = -\frac{2\pi L}{L_{b1}} + \frac{\gamma L I_{ss}}{12}(|v|^2 - |u|^2)(1 - 2\cos(2\Delta\varphi)) + Im(D_{yy}) - Im(D_{xx}) + \frac{(|v|^2-|u|^2)}{|u||v|} Im(D_{xy})\cos(\Delta\varphi) - \frac{(|v|^2+|u|^2)}{|u||v|} Re(D_{xy})\sin(\Delta\varphi). \quad (1.25)$$

1.10 SPIRAL POLARIZATION ATTRACTOR (THEORY)

Adjusting the in-cavity polarization controller enables changing fiber-POC birefringence from zero isotropic case to the case of high birefringent cavity. For the case of weak birefringence ($L_{b1}>>L$) and the pump power for laser below the threshold, cylindrical symmetry leads in SOP degeneration. However, for the pump power above the threshold value, instability of the steady state solution with the Stokes vector **S**= (S_0,0,0±1) results in emergence of a double scroll attractor located at the Poincaré sphere (S. Sergeyev 2014, S. V. Sergeyev 2014).

Results for the numerical simulations of Equations (1.13) for the case of the isotropic cavity ($L_{b1}>>L$) are shown in Figure 1.24. Anisotropy in the cavity is caused by the elliptically polarized pump and external fiber patchcord transforms the output lasing SOP. When the pump is circularly polarized (δ=1), the spiral attractor is symmetrical with the repeatable trajectories (Figure 1.24a). If the pump SOP is an elliptical (δ=0.8), the laser becomes more anisotropic and the output SOP is locked (Figure 1.24b). Increased pump power and weak deviation of the pump SOP from the circular (δ=0.99) transforms the symmetry and the trajectories fill more densely the surface of the Poincare sphere (Figure 1.24c).

<Figure 1.24 here>

Fig. 1.24 Theoretically obtained: a, c, Polarization precessing, and b, Polarization locked vector solitons in terms of a, b, c, Stokes parameters at the Poincaré sphere. Parameters: a-c, $\varepsilon=10^{-4}$, $\alpha_1 L=200/ln(10)$, $\alpha_2 L=0.136$, $\alpha_3=10^{-4}$, $\alpha_4 L=50/ln(10)$, $\chi=5/3$, $\Delta=0.1$, $\gamma L I_{ss}=2\text{x}10^{-6}$; a, $I_p=30$, $\delta=1$; b, $I_p=30$, $\delta=0.8$; c, $I_p=100$, $\delta=0.99$.

Given the polarimeter's photodetector has cut-off frequency of 1 MHz that means averaged over 25 roundtrips, polarization dynamics, the attractors in Fig. 24 can have the different shape. To justify such comment, we have processed the time domain waveforms shown in Figure 1.24 by using a low-pass filter in the form of a Hanning window (Transmission spectrum $T(f) = (1 + cos(\pi f/f_c))/2,\ f \le f_c = 1MHz$) As a result, the spiral attractor in Figure 1.24a is slightly modified towards the shape similar to the experimentally observed (Figures 1.24a and 1.24a). Unlike this case, the filtering does not affect a polarization locked case (Figure 1.24b and 1.25b). Also, the low pass filter transforms the fast-evolving trajectory in Figure 1.24c to the slow-evolving one which is taking the shape of the double semi-circle trajectory similar to the experimentally observed (Figure 1.25c). Presented in Figures 1.24a and 1.25a spiral attractor dynamics is related to the relaxation oscillations with the period in terms of round-trip time and notations to Equations (1.12) of $T_{osc} \sim \varepsilon^{1/2}$ (Khanin 2005). With 40 ns round trip time and $\varepsilon=10^{-4}$, we have $T_{osc} \sim 4$ μs. Neglecting the gain dynamics leads to $\varepsilon \to \infty$ in Equations (1.12) and so $T_{osc} \to \infty$. It means that auto-oscillations doesn't exist and so there is no spiral attractor. Thus, Equations (1.12) can't be further simplified and slow gain dynamics has to be included into consideration.

<Figure 1.25 here>

Figure 1.25 Low-pass filtering with a Hanning window: a) Spiral attractor after filtering; b)

locked SOP, c) transformation of the double-scroll attractor to the double semi-circle by data filtering; (Transmission spectrum $T(f) = (1 + cos(\pi f/f_c))/2,\ f \le f_c = 1MHz$). Parameters: a-f, h-i, $\varepsilon=10^{-4}$, $\alpha_1 L=200/ln(10)$, $\alpha_2 L=0.136$, $\alpha_3=10^{-4}$, $\alpha_4 L=50/ln(10)$, $\chi=5/3$, $\Delta=0.1$, $\gamma L I_{ss}=2\text{x}10^{-6}$; *a-c*, $I_p=30$, $\delta=1$; *d-f*, $I_p=100$, $\delta=0.99$; h, i, $I_p=30$, $\delta=0.8$.

In the theory of coupled oscillators', the weak coupling leads to a complex behavior, while the strong coupling leads to the quenching oscillations and emerging the globally stable steady state (the Bar-Eli effect (Aronson DG 1990)). For our vector model, the coupling strength depends on the pump SOP ellipticity and power. Also, coupling the orthogonally polarized lasing SOPs takes place through the gain sharing, detuning of the lasing wavelength with respect to the maximum of the gain spectrum and the Kerr nonlinearity.

To find the contribution of each of these factors to the origin of the spiral attractor, we present three different cases: 1) scalar model of the Er-doped active medium, and a vector model of CNT; 2) a scalar model of both Erbium active medium and CNT, 3) a vector model of the active Erbium medium, and a scalar model of CNT at Δ=0 (Δ is detuning of the lasing wavelength with respect to the maximum of the gain spectrum).

First, we linearized the equations by substituting $|u| = |u_0| + x_1, |v| = |v_0| + x_1, \Delta\varphi = \Delta\varphi_0 + x_3, f_1 = f_{10} + x_4, f_2 = f_{20} + x_5, f_3 = f_{30} + x_5$in Equations (1.12) and account for the different coefficients for the cases 1)-3) . Here $|u_0|, |v_0|,\ \Delta\varphi_0, f_{10},\ f_{20},\ f_{30}$ are steady state solutions for the cases 1)-3)

$$|u_0|^2 = |v_0|^2 = \frac{\pi\alpha_1}{2\chi\alpha_4}\left(\frac{I_p}{2}(\chi-1)-1\right) - \frac{\pi(1+\Delta^2)}{2\chi}\left(1+\frac{I_p}{2}\right),$$

$$\Delta\varphi_0 = \pm\frac{\pi}{2}, f_{10} = \frac{I_p(\chi-1)/2-1}{1+\frac{I_p}{2}+\frac{2\chi|u_0|^2}{(1+\Delta^2)\pi}}, f_{20} = f_{30} = 0. \quad (1.26)$$

Where $u = |u|\,exp(\varphi_u)$, $v = |v|\,exp(\varphi_v)$, and $\Delta\varphi = \varphi_u - \varphi_v$ is the phase difference between

two linearly polarized SOPs. Substituting $x_i = \tilde{x}_i\, exp(\lambda t_s)$ into the linearized equations, we find the following eigenvalues

$$\lambda_{1,2} = \pm 2\sqrt{a_1^2 + a_2^2}\ ,\ \lambda_{3,4} = \frac{-b_2+4a_1}{2} \pm \frac{1}{2}\sqrt{(b_2+4a_1)^2 - 8a_3b_1}. \quad \text{case 1)}$$

$$\lambda_1 = 2a_2,\ \lambda_2 = -2a_2, \lambda_{3,4} = \frac{-b_2+4a_1}{2} \pm \frac{1}{2}\sqrt{(b_2+4a_1)^2 - 8a_3b_1}. \quad \text{case 2)}$$

$$\lambda_{1,2} = \frac{-b_2+2a_1}{2} \pm \frac{1}{2}\sqrt{(b_2+2a_1)^2 - 4a_3b_1},\ \lambda_{3,4} = \frac{-b_2-4a_1}{2} \pm \frac{1}{2}\sqrt{(b_2-4a_1)^2 - 8a_3b_1},$$

$$\lambda_{5,6} = \frac{-b_2+4a_1}{2} \pm \frac{1}{2}\sqrt{(b_2+4a_1)^2 - 8a_3b_1}. \quad \text{case 3)}$$

(1.27)

Where

$$a_1 = \frac{\alpha_2 L a_3 |u_0|^2}{2\pi}, a_2 = \frac{2\gamma L I_{ss}|u_0|^2}{3},\ a_3 = \frac{\alpha_1 L}{1+\Delta^2},\ b_1 = \varepsilon\chi f_{10}\frac{2|u_0|^2}{(1+\Delta^2)\pi}, b_2 = \varepsilon\left(1 + \frac{I_p}{2} + \frac{2\chi|u_0|^2}{(1+\Delta^2)\pi}\right).$$

(1.28)

Next, we introduce a saddle index as follows (Ovsyannikov IM 1987)

$$\nu = |\rho/\gamma|, \quad If\ \lambda_1 = \gamma > 0, \quad \lambda_{2,3} = -\rho \pm i\omega, \quad (\omega \neq 0, \rho > 0), or\ \lambda_1 = -\gamma < 0, \quad \lambda_{2,3} = \rho \pm i\omega, \quad (\omega \neq 0, \rho > 0). \quad (1.29)$$

Equation (1.29) describe saddle-focus with limit cycles emerging in the homoclinic bifurcation. According to the Shilnikov theorem, the stability and number of the limit cycles is defined by saddle index ν (Ovsyannikov IM 1987). If ν >1 homoclinic bifurcations results in one stable limit cycle. Unlike this, for ν <1 an infinite number of unstable cycles emerge and form a chaotic attractor (Ovsyannikov IM 1987). The saddle index as a function of pump power I_p is shown in Figure 1.26. As follows from Figure 1.26, the double-scroll attractor cannot exist for the first and the second case and, also, for the third case where $\lambda_i = -\rho_i \pm i\omega_i, \quad (\omega_i \neq 0, \rho_i > 0)$. Thus,

we conclude that the detuning of the lasing wavelength with respect to the maximum of the gain spectrum and SOPs coupling through the gain sharing leads to the complex dynamics.

<Figure 1.26 here>

Fig. 26 Saddle index ν as a function of the normalized pump power I_p for the first case (solid line) and the second case (dashed line). Parameters (thin and thick lines): $\varepsilon=10^{-4}$, $\alpha_1 L=200/\ln(10)$, $\alpha_2 L=0.136$, $\alpha_4 L=50/\ln(10)$, $\chi=5/3$, $\Delta=0.1$, $\delta=1$, $\gamma L I_{ss}=2\times10^{-6}$; (thin lines): $\alpha_3=10^{-4}$; (thick lines): $\alpha_3=10^{-2}$.

1.11 INTREPLAY BETWEEN POLARIZATION HOLE BURNING AND IN-CAVITY BIREFINGENCE (THEORY)

To illustrate interplay between birefringence and polarization hole burning, we solve Equations (1.12) numerically by varying pump SOP ellipticity δ and beat length L_{b1}, and using parameters values quite close to the experimental ones (S. Sergeyev 2014), *viz.* $L=10m$, $\alpha_1 L=\ln(10)6.4$, $\alpha_2 L=0.136$, $\alpha_3=10^{-4}$, $\alpha_4 L=\ln(10)0.5$, $\chi=3/2$, $\Delta=0.1$, $I_p=30$, $\gamma L I_{ss}=2\times10^{-6}$, $\varepsilon=10^{-4}$. The results for $\delta=1$ (circularly polarized pump) are shown in Figure 1.27.

As follows from Figure 1.27a-f, weak birefringence can distort spiral attractor and results in SOP localization close to the circle $s_2^2+s_3^2=1$. In line with Equation 1.21, SOP is reproduced in n round trips with a drift caused by polarization hole burning.

<Figure 1.27 here>

Figure 1.27. Fast and slow evolution of vector solitons in terms of Stokes parameters in the Poincaré sphere. Parameters: $L=10m$, $\alpha_1 L=\ln(10)6.4$, $\alpha_2 L=0.136$, $\alpha_3=10^{-4}$, $\alpha_4 L=\ln(10)0.5$, $\chi=3/2$,

$\Delta=0.1$, $I_p=30$, $\gamma LI_{ss}=2x10^{-6}$, $\varepsilon=10^{-4}$, $\delta=1$; a) $L_b=500$ L, b) $L_b=250$ L, c) $L_b=100$ L, d) $L_b=3$ L, e) $L_b=2$ L, f) $L_b=$ L.

By changing ellipticity from to $\delta=1$ to $\delta=0.5$, we find that SOP is localized at the circle $s_2^2+ s_3^2=a$ $(a<1, s_1\neq0)$ with slightly suppressed SOP drift (Figure 1.28a,b). For the pump power decreased from $I_p=30$ to $I_p=20$, the drift is completely suppressed (Figure 1.28c). The origin of drift can be clarified by analyzing the signal power S_0 as a function of number of round trips (Figure 1.28d-f). As follows from Figure 1.28d, e, fast oscillations of S_0 are caused by changes in the pulse-to-pulse rotation matrix associated with gain $\boldsymbol{G}$ (Equation 1.23). Elliptically polarized pump with ellipticity of $\delta=0.5$ leads to the light-induced anisotropy and so suppressed oscillations and (Figure 1.28e). As follows from Figure 1.28e. Stokes parameter s_1 increase with increased light-induced anisotropy that, according to Equation 1.25 results in decreased contribution of the active medium to the SOP drift. By decreasing the pump power from $I_p=30$ to $I_p=20$ we reduce the lasing powers $|v|^2, |u|^2$ that results in suppression of S_0 (normalized output power) oscillations and so, according to Equation 1.25, in suppression of SOP drift as shown in Figure 1.28c, f.

The obtained theoretical results are in a good agreement with our experimental data obtained previously for fundamental, bound state (BS) and multipulsing (MP) soliton operations (sections 1.1-1.4 (Mou Ch. 2013, S. Sergeyev 2014, S. V. Sergeyev 2012, S. V. Sergeyev 2014, Tsatourian V 2013, Tsatourian V. 2013)). For example, application of ansatz (Equation 1.11) is justified by our experimental study where pulse width is fixed (Sections 1.1 – 1.4). Also, the ansatz can be used for different pulse shapes with fixed pulse widths also, viz. for Gaussian in the case of normal dispersion, multipulsing and bound soliton soliton regimes (Mou Ch. 2013, S. Sergeyev 2014, S. V. Sergeyev 2012, S. V. Sergeyev 2014, Tsatourian V 2013, Tsatourian V.

2013)).

<Figure 1.28 here>

Figure 1.28 Interplay between different types of birefringence caused by in-cavity polarisation controller and polarization hole burning, and light-induced anisotropy caused by elliptically polarized pump; a) – c) fast and slow evolution of vector solitons in in terms of Stokes parameters in the Poincaré sphere, d) – e) output power signal S_0 as a function of number of round trips. Parameters: a)-f) L_b=3 L; a), d) I_p=30, δ=1; b), e) I_p=20, δ=0.5; c), f) I_p=20, δ=1.

1.12 VECTOR SOLITON RAIN (THEORY)

To understand the experimental data on spiral attractor transformation caused by the soliton rain, we review our recent theoretical results (Sergeyev, S.V., Eliwa, M., Kbashi, H. 2022) . Equation 1.12 are complemented by presentation of the vector soliton rain in the form of an injected signal with periodically evolving SOPs:

$$E_x = a \cdot \cos(\Omega t + \phi_0)\,, E_y = a \cdot \sin(\Omega t + \phi_0) \cdot exp(\Delta\varphi). \quad (1.30)$$

Here a is the amplitude of the soliton rain, Ω is the frequency of oscillations, ϕ_0 is the initial phase, $\Delta\varphi$ is the phase difference between the orthogonal SOPs. The main pulse depletes orientation distribution of inversion mainly at orientation coinciding the linearly polarized SOP (polarization hole burning, PHN) in and so SR pulses can have a SOPs different from the main pulse's SOP (Kbashi H.J. 2019). So, periodically evolving main pulse's SOP causes oscillation of the SR SOP as shown in Equation 1.30. With taking into account Equation 1.30, Equations 1.12 take the form:

$$\frac{du}{dt} = i\beta u + i\frac{\gamma}{2}\left(|u|^2 u + \frac{2}{3}|v|^2 u + \frac{1}{3}v^2 u^*\right) + D_{xx}u + D_{xy}v + E_x,$$

$$\frac{dv}{dt} = -i\beta v + i\frac{\gamma}{2}\left(|v|^2 v + \frac{2}{3}|u|^2 v + \frac{1}{3}u^2 v^*\right) + D_{xy}u + D_{yy}v + E_y,$$

$$\frac{dn_0}{dt} = \varepsilon\left[I_p + 2R_{10} - \left(1 + \frac{I_p}{2} + \chi R_{10}\right)n_0 - \chi R_{11}n_{12} - \chi n_{22}R_{12}\right],$$

$$\frac{dn_{12}}{dt} = \varepsilon\left[\frac{(1-\delta^2)}{(1+\delta^2)}\frac{I_p}{2} + R_{11} - \left(1 + \frac{I_p}{2} + \chi R_{10}\right)n_{12} - \left(\frac{(1-\delta^2)}{(1+\delta^2)}\frac{I_p}{2} + \chi R_{11}\right)\frac{n_0}{2}\right],$$

$$\frac{dn_{22}}{dt_s} = \varepsilon\left[R_{12} - \left(1 + \frac{I_p}{2} + \chi R_{10}\right)n_{22} - \chi R_{12}\frac{n_0}{2}\right],$$

$$R_{10} = \frac{1}{(1+\Delta^2)}(|u|^2 + |v|^2), \quad R_{11} = \frac{1}{(1+\Delta^2)}(|u|^2 - |v|^2), R_{12} = \frac{1}{(1+\Delta^2)}(uv^* + vu^*),$$

(1.31)

Coefficients D_{ij} can be found as follows:

$$D_{xx} = \frac{\alpha_1(1-i\Delta)}{1+\Delta^2}(f_1 + f_2) - \alpha_2 + ln\left(1 - \frac{\alpha_0}{1+\alpha_s(|u|^2+v^2)}\right), \; D_{yy} = \frac{\alpha_1(1-i\Delta)}{1+\Delta^2}(f_1 - f_2) - \alpha_2 +$$

$$ln\left(1 - \frac{\alpha_0}{1+\alpha_s(|u|^2+v^2)}\right), D_{xy} = D_{yx} = \frac{\alpha_1(1-i\Delta)}{1+\Delta^2}f_3. \qquad (1.32)$$

To obtain results shown in Figure 1.29, we used the following parameters: a), d), g) I_p *=25, a=0.001* ; b), e), h) I_p *=22, a=0.02*; c), f), i) I_p *=30, a=10.* The other parameters: a)-i) $\beta_L = \beta_C = 0$, $\alpha_1 = 5.38, \alpha_2 = 1, \alpha_s = 10^{-3}$, $\alpha_0 = 0.136, \delta = 0.99$ (elliptically polarized pump SOP), *D=0.13* ε=10^{-4}, χ_p=1, χ_s=2.3, Ω=0.005π, ϕ_0 =0, Ψ=π/2. To model the effect of the output SOP transformation caused by the patchcord

connected to the polarimeter, we use the 3D rotation (around axes related to the Stokes parameters S_0, S_1, S_2, S_3) matrix (Varshalovich 1988):

$$\begin{pmatrix} \tilde{S}_1 \\ \tilde{S}_2 \\ \tilde{S}_3 \\ \tilde{S}_0 \end{pmatrix} = \begin{bmatrix} a_{11} & a_{12} & a_{13} & 0 \\ a_{21} & a_{22} & a_{23} & 0 \\ a_{31} & a_{32} & a_{33} & 0 \\ 0 & 0 & 0 & 1 \end{bmatrix} \begin{pmatrix} S_1 \\ S_2 \\ S_3 \\ S_0 \end{pmatrix},$$

$$a_{11} = \cos(\psi)\cos(\gamma),\ a_{12} = \cos(\gamma)\sin(\alpha)\sin(\psi) - \cos(\alpha)\sin(\gamma),$$

$$a_{13} = \cos(\alpha)\cos(\gamma)\sin(\psi) + \sin(\alpha)\sin(\gamma),$$

$$a_{21} = \cos(\psi)\sin(\gamma),\ a_{22} = \cos(\alpha)\cos(\gamma) + \sin(\alpha)\sin(\psi)\sin(\gamma),$$

$$a_{23} = -\cos(\gamma)\sin(\alpha) + \sin(\psi)\sin(\gamma),\ a_{31} = -\sin(\gamma),\ a_{32} = \cos(\psi)\sin(\alpha),$$

$$a_{33} = \cos(\alpha)\cos(\psi). \qquad (1.33)$$

<Figure 1.29 here>

Figure 1.29 Slow polarization dynamics: a)- c) trajectories on the Poincaré sphere.); d) - f) The output power vs number of the round trips for two linearly cross-polarized SOPs I_x (dashed line) and I_y (dotted line) and total power $I=I_x+I_y$ (black);); g-f) the phase difference vs number of the round trips. Parameters: $\alpha = -\pi/4, \beta = \pi/4,\ \gamma = 2\pi/5$, (a-i); I_p =25 (a, d, g), I_p =22 (b, e, h); Ip=30 (c, f, i). The time span of 10^4 corresponds to 1 ms.

As follows from Figure 1.29a-h, the injected signal with evolving SOP modifies the spiral attractor and polarization dynamics of the SOPs x and y. Theoretical results are quite close to the experimental data (

Figure 1.15a-h) for the soliton rain's condensed phase in Figure 1.14a, b. Increased amplitude of the injected signal from *a=0.02 to a=10* transform the spiral attractor is transformed to the circle (Fig. 1.29c), and x and y SOPs' oscillations take the form of antiphase close to harmonic oscillations with the fast phase difference switching (Figure 1.29 f, i). The dynamics is quite close to the experimental results shown in Figure 1.15 c, f, i and the corresponding the soliton rain bunch shown in Figure 1.14 c.

Kbashi and co-workers demonstrated that the mechanism driving the SR origin and merging to the condensate phase is competition between polarization hole burning (PHB) caused by SR pulses and holes refilling by the pump wave and active medium (Kbashi H.J. 2019). Here we reveal a new effect of the soliton rain on the active medium in the context of modifying the polarization properties. In the SR condensed phase (Figure 1.14a,b,d,e), the SR completely depletes population inversion and cw component can't appear. The active medium is slightly modified by SHB by inducing a small circular birefringence and so the spiral attractor on the Poincaré sphere emerges (Figure 1.14a,b,d,e,g,h) and Figure 1.29b,e,h). The soliton bunch appears when PHB can't deplete the population inversion completely, and CW components generated (Figure 1.14f). The soliton bunch has a large amplitude and the periodically evolving SOP caused by the its drift and so transforms the spiral attractor to the circle on the Poincaré sphere (Figures 1.15c,f, i) and 1.29c, f, i). The obtained results can pave the wave to development a new technique for the laser dynamics' control by using the injected optical signal with evolving states of polarization that of interest for different application including spectroscopy, metrology and biomedical diagnostics.

1.13 VECTOR BRIGHT-DARK ROGUE WAVES (THEORY)

To justify mechanism of the RWs emergence at the fast and slow time scales, we modify Equations 1.12 as follows:

$$\frac{dS_0}{dt} = \left(\frac{2\alpha_1 f_1}{1+\Delta^2} - 2\alpha_2 - ln\left(1 - \frac{\alpha_0}{1+\alpha_s S_0}\right)\right)S_0 + \frac{2\alpha_1 f_2}{1+\Delta^2}S_1 + \frac{2\alpha_1 f_3}{1+\Delta^2}S_2,$$

$$\frac{dS_1}{dt} = \gamma S_2 S_3 + \frac{2\alpha_1 f_2}{1+\Delta^2}S_0 + \left(\frac{2\alpha_1 f_1}{1+\Delta^2} - 2\alpha_2 - ln\left(1 - \frac{\alpha_0}{1+\alpha_s S_0}\right)\right)S_1 - \beta_c S_2 - \left(\frac{2\alpha_1 f_3 \Delta}{1+\Delta^2}\right)S_3,$$

$$\frac{dS_2}{dt} = -\gamma S_1 S_3 + \frac{2\alpha_1 f_3}{1+\Delta^2}S_0 + \beta_c S_1 + \left(\frac{2\alpha_1 f_1}{1+\Delta^2} - 2\alpha_2 - ln\left(1 - \frac{\alpha_0}{1+\alpha_s S_0}\right)\right)S_2 + \left(\frac{2\alpha_1 f_2 \Delta}{1+\Delta^2}\right)S_3,$$

$$\frac{dS_3}{dt} = \left(\frac{2\alpha_1 \Delta f_3}{1+\Delta^2}\right)S_1 - \left(\frac{2\alpha_1 \Delta f_2}{1+\Delta^2}\right)S_2 + \left(\frac{2\alpha_1 f_1}{1+\Delta^2} - 2\alpha_2 - ln\left(1 - \frac{\alpha_0}{1+\alpha_s S_0}\right)\right)S_3,$$

$$\frac{df_1}{dt} = \varepsilon\left[\frac{(\chi_s - 1)I_p}{2} - 1 - \left(1 + \frac{I_p \chi_p}{2} + d_1 S_0\right)f_1 - \left(d_1 S_1 + \frac{I_p \chi_p}{2}\frac{(1-\delta^2)}{(1+\delta^2)}\right)f_2 - d_1 S_2 f_3\right],$$

$$\frac{df_2}{dt} = \varepsilon\left[\frac{(1-\delta^2)}{(1+\delta^2)}\frac{I_p(\chi_s - 1)}{4} - \left(\frac{I_p \chi_p}{2} + 1 + d_1 S_0\right)f_2 - \left(\frac{(1-\delta^2)}{(1+\delta^2)}\frac{I_p \chi_p}{2} + d_1 S_1\right)\frac{f_1}{2}\right],$$

$$\frac{df_3}{dt} = -\varepsilon\left[\frac{d_1 S_2 f_1}{2} + \left(\frac{I_p \chi_p}{2} + 1 + d_1 S_0\right)f_3\right]. \quad (1.34)$$

Here time and length are normalized to the round trip and cavity length, respectively; S_i *(i=0,1,2,3)* are the Stokes parameters defined in Equation 1.1 (S_0 is the output power, pump and lasing powers are normalized to the corresponding saturation powers); $\beta_{L\,(C)} = 2\pi/L_{bL(bC)}$ is the linear (circular) birefringence, $L_{bL(bC)}$ is the linear (circular) birefringence beat length; α_1 is the total absorption of erbium ions at the lasing wavelength, α_2 is the total insertion losses in the cavity; δ is the ellipticity of the pump wave, $\varepsilon = \tau_R/\tau_{Er}$ is the ratio of the round trip time τ_R to the lifetime of erbium ions at the first excited level τ_{Er}; $\chi_{p,s} = (\sigma_a^{(s,p)} + \sigma_e^{(s,p)})/\sigma_a^{(s,p)}$, ($\sigma_a^{(s,p)}$ and $\sigma_e^{(s,p)}$ are absorption and emission cross-sections at the lasing (s) and pump (p) wavelengths); Δ is the detuning of the lasing wavelength with respect to the maximum of the gain spectrum (normalized to the gain spectral width); $d_1 = \chi_s/\pi(1+\Delta^2)$.

To explain mechanism of RW emergence, we solve Equations 1.34 numerically by using the parameters shown in Figure 1.30.

<Figure 1.30 here>

Figure 1.30 Laser dynamics averaged over the roundtrip time and after low pass filtering. Dynamics before (a-c) and after (d-f) low-pass filtering with a Hanning window with transmission spectrum ($T(f)=(1+\cos(\pi f/f_c))/2, f\le f_c=1MHz$). a) Dynamics of the output power; b) dynamics of the phase difference $\Delta\phi$; c) probability distribution histograms (the output power I is normalized as shown in Fig.2); d) dynamics of the output powers $I=I_x+I_y$ (black) and the phase difference $\Delta\phi$ (gray); e) trajectories on the Poincaré sphere; f) Probability distribution histogram for the total output power (output power is normalized as shown in Figs. 16 and 17). Parameters: $I_p=76$; $\alpha_1=21.53$, $\alpha_0=0.136$, $\alpha_s=1.8\cdot10^{-5}$, $\alpha_2=2.533$, $\chi=2.3$, $\Delta=0.1$, $\gamma=2x10^{-6}$, $\varepsilon=10^{-4}$; a-f) $\delta=0.84$ (elliptically polarized pump), $\beta=1.1\pi\cdot10^{-2}$.

As follows from Figure 1.30, adjusting the pump power, birefringence and the ellipticity of the pump wave leads to the emergence of the bright-dark rogue waves. After the data averaging over 30 round-trips (1 MHz low-pass filter) the data are transformed (Figure 1.30d-f). The obtained results in Fig. 1.30 are in a good correspondence to the experimental data shown in Figures 16 and 17. The anomalous spikes-dips in the output power (Figure 1.30a,b,d) coincides with the phase difference jumps in π (Figue 1.30b, d), i.e. transitions between orthogonally polarized SOPs (Figure 1.30e). Probability distribution diagram for the total power $I=I_x+I_y$ (Figure 1.30 c, f) is showing the presence the dark-bright RWs. The emergence of the RWs at the slow time scale is explained in terms of transition of the synchronization scenario from the phase locking to the chaotic phase drift (section 1.16).

Thus, we demonstrate a new type of the bright-dark rogue waves resulting from the interaction between the orthogonal SOPs in an Er-doped mode-locked fiber laser. By adjusting in-cavity and the pump wave polarization controllers, we enable control of the coupling between SOPs towards SOPs desynchronization and so emergence of the bright-dark rogue. The revealed mechanism shows a great potential for mapping conditions for RWs existence and so for developing

techniques for suppression RWS in different distributed systems.

1.14. VECTOR RESONANCE MULTIMODE INTSABILIT (THEORY)

The experimental results on mode-locking based on Vector Resonance Multimode Instability (VRMI) can be well understood based on the vector model of an Er-doped fiber laser derived by Sergeyev et al. (Sergeyev S. 2018):

$$\begin{gathered}
\frac{\partial S_0}{\partial z}+\frac{\partial S_0}{\partial t}=\left(\frac{2\alpha_1 f_1}{1+\Delta^2}-2\alpha_2\right)S_0+\frac{2\alpha_1 f_2}{1+\Delta^2}S_1+\frac{2\alpha_1 f_3}{1+\Delta^2}S_2,\\
\frac{\partial S_1}{\partial z}+\frac{\partial S_1}{\partial t}=\gamma S_2 S_3+\left(\frac{2\alpha_1 f_1}{1+\Delta^2}-2\alpha_2\right)S_1+\frac{2\alpha_1 f_2}{1+\Delta^2}S_0-\frac{2\alpha_1 f_3\Delta}{1+\Delta^2}S_3,\\
\frac{\partial S_2}{\partial z}+\frac{\partial S_2}{\partial t}=-\gamma S_1 S_3+\frac{2\alpha_1 f_3}{1+\Delta^2}S_0+\left(\frac{2\alpha_1 f_1}{1+\Delta^2}-2\alpha_2\right)S_2+\left(\frac{2\alpha_1 f_2\Delta}{1+\Delta^2}-2\beta\right)S_3,\\
\frac{\partial S_3}{\partial z}+\frac{\partial S_3}{\partial t}=\frac{2\alpha_1\Delta f_3}{1+\Delta^2}S_1-\frac{2\alpha_1\Delta f_2}{1+\Delta^2}S_2+2\beta S_2+\left(\frac{2\alpha_1 f_1}{1+\Delta^2}-2\alpha_2\right)S_3,\\
\frac{df_1}{dt}=\varepsilon\left[\frac{(\chi_s-1)I_p}{2}-1-\left(1+\frac{I_p\chi_p}{2}+d_1S_0\right)f_1-\left(d_1S_1+\frac{I_p}{2}\xi\right)f_2-d_1S_2f_3\right],\\
\frac{df_2}{dt}=\varepsilon\left[\xi\frac{I_p(\chi_s-1)}{4}-\left(\frac{I_p\chi_p}{2}+1+d_1S_0\right)f_2-\left(\frac{I_p\chi_p}{2}\xi+d_1S_1\right)\frac{f_1}{2}\right],\\
\frac{df_3}{dt}=-\varepsilon\left[\frac{d_1S_2f_1}{2}+\left(\frac{I_p\chi_p}{2}+1+d_1S_0\right)f_3\right].
\end{gathered} \tag{1.35}$$

Here $\xi=(1-\delta^2)/(1+\delta^2)$ is parameter of the pump anisotropy.

Given the experimental condition that used pump power of 18 mW is much less than values (approx. 800 mW) required for mode locking based on nonlinear polarization rotation (NPR) [], the presnted model excludes NPR-based mode-locking (Lecaplain 2014) . The pulse width in our experiments (Fig. 19) was estimated to be of 40 ns and so we can use approximation where the second order dispersion can be neglected in the model of VMRI-based mode-locking. Also, the pulse width is much longer than the transverse relaxation time of 160 fs. Therfore, the medium polarization dynamics can be ignored (Fontana 1995, E. B. Pessina 1997, E. P. Pessina 1999, Voigt 2004, Lugiato 2015).

To find conditions for the VRMI-based mode locking, we linearize the Equation 1.35 nearby

the steady state solution $\boldsymbol{F}_0=(S_{00}\ \pm S_{00}\ \ 0\ 0\ f_{10}\ f_{20}\ 0)^T$ and substitute the following ansatz into Equation 1.35:

$$\boldsymbol{F}(t,z) \equiv [S_0 S_1 S_2 S_3 f_1 f_2 f_3]^T = \boldsymbol{F}_0 + [x_0 x_1 x_2 x_3 x_4 x_5 x_6 x_7]^T \, exp(\lambda t + qz)\,,$$

(1.36)

where $\boldsymbol{F}_0=(S_{00}\ \pm S_{00}\ \ 0\ 0\ f_{10}\ f_{20}\ 0)^T$. As a result, we find the following equation for eigenvalues:

$$det\begin{bmatrix} a_1 - iq - \lambda & 0 & 0 & 0 & a_2 & a_2 & 0 \\ -a_1 & a_1 - iq - \lambda & 0 & 0 & a_2 & a_2 & 0 \\ 0 & 0 & a_1 - iq - \lambda & a_3 + a_4 & 0 & 0 & a_2 \\ 0 & 0 & -a_3 & a_1 - iq - \lambda & 0 & 0 & \Delta \cdot a_2 \\ b_2 & b_4 & 0 & 0 & b_1 - \lambda & b_3 & 0 \\ b_4 & b_2/2 & 0 & 0 & b_3/2 & b_1 - \lambda & 0 \\ 0 & 0 & b_2/2 & 0 & 0 & 0 & b_1 - \lambda \end{bmatrix} = 0$$

(1.37)

where

$$a_1 = \frac{2\alpha_1}{1+\Delta^2} f_{10} - \alpha_2, a_2 = \frac{2\alpha_1}{1+\Delta^2} S_{00}, a_3 = \frac{2\alpha_1 \Delta}{1+\Delta^2} f_{20} - 2\beta, a_4 = -\gamma S_{00},$$

$$b_1 = -\varepsilon\left(1 + \frac{I_p \chi_p}{2} + d_1 S_{00}\right), b_2 = -\varepsilon d_1 f_{10}, b_3 = -\varepsilon\left(d_1 S_0 + \frac{I_p \chi_p \xi}{2}\right), b_4 = -\varepsilon d_1 f_{20},$$

$$S_{00} = \frac{-Q_2 - \sqrt{{Q_2}^2 - 4Q_1 Q_3}}{2Q_1}, Q_1 = -\frac{\alpha_2 d_1^2}{2},$$

$$Q_2 = -\alpha_2\left(2d_1\left(1 + I_p\chi_p\right) - \tfrac{d_1 I_p \xi}{2}\right) + \left(\tfrac{\chi_s - 1}{2} I_p - 1\right).$$

(1.38)

As a result, Equation 1.37 has three branches of eigenvalues:

$$\lambda - 2a_1 + 2iq = 0, \quad (I)$$

$$\lambda^3 + [-2b_1 + iq]\lambda^2 + \left(b_1^2 - \frac{b_3^2}{2} - \frac{3a_2 b_2}{2} - 2a_2 b_4 - 2iq b_1\right)\lambda + \frac{3a_2 b_1 b_2}{2} + 2a_2 b_1 b_4 -$$

$$2a_2b_1b_4 - a_2b_2b_3 - \frac{3a_2b_3b_4}{2} - \frac{ib_3^3q}{2} + ib_1^2q = 0, \quad (II)$$

$$\lambda^3 + (-2a_1 - b_1 + 2iq)\lambda^2 + \left(a_1^2 + 2b_1a_1 + a_3^2 + a_{\ 4}a_3 - q^2 - \frac{a_2b_2}{2} - 2ib_1q - 2ia_1q\right) +$$

$$b_1q^2 - a_3^2b_1 - a_1^2b_1 + \frac{a_1a_2b_2}{2} - a_3a_4b_1 - \frac{a_2a_3b_2\Delta}{2} - \frac{a_2a_4b_2\Delta}{2} - \frac{ia_2b_2q}{2} + 2ia_1b_1q$$

$$= 0, \quad (III)$$

As a result:

(1.39)

$$(I) \quad \lambda_0 = iq + A_0(I_p, \xi),$$

$$(II) \quad \lambda_1 = A_1(q, I_p, \xi) + i\Omega_1(q, I_p, \xi), \quad \lambda_2 = A_2(q, I_p, \xi) + i\Omega_2(q, I_p, \xi),$$

$$\lambda_3 = A_3(q, I_p, \xi) + i\Omega_3(q, I_p, \xi),$$

$$(III) \quad \lambda_4 = A_4(q, I_p, \beta, \xi) + i\Omega_4(q, I_p, \beta, \zeta),$$

$$\lambda_5 = A_5(q, I_p, \beta, \xi) + i\left(q + \Delta\Omega(q, I_p, \beta, \xi)\right), \quad \lambda_6 = A_6(q, I_p, \beta, \xi) + i\left(q - \Delta\Omega(q, I_p, \beta, \xi)\right),$$

$$A_0(I_p, \xi) > 0,\ A_1(q, I_p, \xi) < 0,\ \ A_2(q, I_p, \xi) < 0,\ \ A_3(q, I_p, \xi) < 0,$$

$$A_4(q, I_p, \xi) < 0,\ A_5(q, I_p, \xi) > 0,\ A_6(q, I_p, \xi) > 0.$$

(1.40)

Here $q=0,\pm1, \pm2,..\pm N$ is the wave number of the longitudinal mode and eigenvalues are normalized to the fundamental frequency $\omega=2\pi/\tau_R$. The results are shown in Figure 1.31. The first and the second (multimode instability) thresholds are found in Figure 1.31a. For RNGH instability, the threshold pump powers for excitation of different number of longitudinal modes are different (Fontana 1995, E. B. Pessina 1997, E. P. Pessina 1999, Voigt 2004, Lugiato 2015), whereas for the case of VRMI the powers are the same (Figure 1.31a). Also, the second threshold of the VRMI coincides with the first lasing threshold for circuitry polarized pump and slightly exceeds the first one with increased pump anisotropy parameter ξ. Threshold for MMI (branch I) coincides with the threshold for excitation of birefringence-dependent RF satellite lines (branch III). As follows from Figure 1.31b, the branch II corresponds to additional birefringence-independent spectral lines with the frequency splitting of 0.01f (f is the fundamental frequency) with respect to

the longitudinal mode frequency q. The real part of the corresponding eigenvalues, i.e. A_1, A_2 and A_3, are less than zero, but the parametric phase locking with the frequencies of the branch I can activate the satellites. For branch III (Figure 1.31c), increased birefringence strength can result in the resonance conditions, i.e. matching longitudinal mode q satellites' frequencies the frequency of the longitudinal mode q+N (where N is integer) from the branch I.

<Figure 1.31 here>

Figure 1.31 The results of linear stability analysis of Equations 1.35. a) Vector multimode instability in terms of positive real parts of eigenvalues, i.e. A_0 (dots), A_5 (solid line) (A_6 is close to the A_5 and so is not shown here) and the output signal S_0 (dashed line) vs pump power I_p for ξ=0 (upper lines), ξ=0.1 (lower line); b) The frequencies of the scalar branch: Ω_1 (empty circles) Ω_2-1(empty triangles), Ω_3 (empty squares) and vector branch Ω_4 (empty diamonds) along with the real parts of the scalar branch: A_1 (filled circles), A_2 (filled triangles), A_3 (filled squares), and the vector branch: A_4 (filled diamonds) vs pump power I_p for ξ=0.1. c) Frequencies for the branch I, i.e. $\Omega_0=\pm q$, q=0,1,2,3 (solid lines), and the vector branch (III), i.e. $\Omega_{5,6}=q\pm\Delta\Omega$ (squares, triangles, circles), vs the birefringence strength $2\beta-2\Delta\alpha_1/(1+\Delta^2)$ for ξ=0.1. The equality $\Omega_0=\Omega_{5,6}$ for $2\beta-2\Delta\alpha_1/(1+\Delta^2)$=1,2,… means the resonance mode locking shown in Figure 1.31c. Parameters: *L=615 m, $2\alpha_1$=ln(10)6.4, $2\alpha_2$=ln(10)0.5, χ_s=3/2, χ_p=1/0.7, Δ=0.1, I_p=10 (c), $\gamma=2x10^{-6}$*, $\varepsilon=10^{-3}$, β=1 (a,b), q=1 (b), ξ=0.1 (b,c).

As follows from Figures 1.31 and 1.19, the theoretical results are in a good correspondence with the experimental data. First, the threshold of the multimode instability (the second threshold) slightly exceeds the first lasing threshold (Figure 1.31 (a)). Second, when the birefringence-dependence satellites frequencies deviates from the longitudinal mode frequencies (Figure 1.19a1-c1), the dynamics takes the form of complex oscillations in view of equal threshold conditions for all longitudinal modes and the absence of the synchronization (Figure 1.31a)). Finally, matching the frequencies for longitudinal modes' harmonics and the birefringence-dependent satellites leads their synchronization similar to the injection locking-based mode locking (S. Y. Cundiff 2003).

Also, stable mode locking is accompanied with the stable SOP locking Figs. 18 (b, c). As follows from Figure 1.31, linear stability analysis results in the eigenfrequencies ratio with respect to the fundamental frequency as $1{:}10^{-1}{:}10^{-2}{:}10^{-3}{:}10^{-4}$. In addition, the presence of harmonics (more than 1000, as follows from the experiment) requires accounting for many time scales and so the direct numerical simulation is very complex problem.

The demonstrated vector resonance multimode instability-based mode-locking can be potentially observed in the other distributed systems. The resonance of the satellite lines caused by the birefringence tuning with the other branch of eigen-frequencies leads to the synchronization phenomena which can be of interest in photonics and beyond.

1.15 VECTOR HARMONIC MODE-LOCKING (THEORY)

To understand the mechanism of harmonic mode-locking tunability and linewidth narrowing, we review our recently developed vector model of EDFLs (Sergeyev S 2021). The model accounts for the linear and circular birefringence and fast- and slow axis modulation caused by TR_{2m} acoustic modes. Without accounting for the gain dynamics, the SOP evolution in terms of the Stokes vector *S* and number of roundtrips caused by the interplay of the factors mentioned above can be described as follows:

$$d\,S/dt = R \cdot W \times S, \tag{1.41}$$

Here time is normalized to the roundtrip time, $W = (\beta_L, 0, \beta_c)^T$ is the birefringence vector, $\beta_{L\,(C)} = 2\pi/L_{bL(bC)}$ is the linear (circular) birefringence strength, $L_{bL(bC)}$ is the beat length for linear (circular) birefringence. The matrix R is the 3x3 matrix that defines the rotation of the birefringence vector around axis OS_3 caused by TR_{2m} excitation (Collett 2003):

$$R = \begin{bmatrix} \cos\left(\zeta(t)\right) & -\sin\left(\zeta(t)\right) & 0 \\ \sin\left(\zeta(t)\right) & \cos\left(\zeta(t)\right) & 0 \\ 0 & 0 & 1 \end{bmatrix}, \tag{1.42}$$

where $\zeta(t) = A_0 \cos(2\pi\Omega t)$. Here $\zeta(t)$ is the angle of the birefringence vector rotation, A_0 is the amplitude of rotation, and Ω is the frequency of oscillations at the TR_{2m} acoustic mode. In Equations 1.41 and 1.42, the contribution of TR_{2m} was accounting for only in the birefringence modulation context. The modulation of the refractive index was neglected. With accounting for Equations 1.41 and 1.42, along with the ASE noise in the cavity, Eqs. (30) and (31) take the following form (Sergeyev S 2021):

$$\frac{dS_0}{dt} = \left(\frac{2\alpha_1 f_1}{1+\Delta^2} - 2\alpha_2\right) S_0 + \frac{2\alpha_1 f_2}{1+\Delta^2} S_1 + \frac{2\alpha_1 f_3}{1+\Delta^2} S_2,$$

$$\frac{dS_1}{dt} = \gamma S_2 S_3 + \frac{2\alpha_1 f_2}{1+\Delta^2} S_0 + \left(\frac{2\alpha_1 f_1}{1+\Delta^2} - 2\alpha_2\right) S_1 - \beta_c S_2 - \left(\frac{2\alpha_1 f_3 \Delta}{1+\Delta^2} - \beta_L sin\left(\zeta(t)\right)\right) S_3 + \sigma_1,$$

$$\frac{dS_2}{dt} = -\gamma S_1 S_3 + \frac{2\alpha_1 f_3}{1+\Delta^2} S_0 + \beta_c S_1 + \left(\frac{2\alpha_1 f_1}{1+\Delta^2} - 2\alpha_2\right) S_2 + \left(\frac{2\alpha_1 f_2 \Delta}{1+\Delta^2} - \beta_L cos\left(\zeta(t)\right)\right) S_3 + \sigma_2,$$

$$\frac{dS_3}{dt} = \left(\frac{2\alpha_1 \Delta f_3}{1+\Delta^2} - \beta_L sin\left(\zeta(t)\right)\right) S_1 - \left(\frac{2\alpha_1 \Delta f_2}{1+\Delta^2} - \beta_L cos\left(\zeta(t)\right)\right) S_2 + \left(\frac{2\alpha_1 f_1}{1+\Delta^2} - 2\alpha_2\right) S_3 + \sigma_3,$$

$$\frac{df_1}{dt} = \varepsilon\left[\frac{(\chi_s - 1) I_p}{2} - 1 - \left(1 + \frac{I_p \chi_p}{2} + d_1 S_0\right) f_1 - \left(d_1 S_1 + \frac{I_p \chi_p}{2} \frac{(1-\delta^2)}{(1+\delta^2)}\right) f_2 - d_1 S_2 f_3\right],$$

$$\frac{df_2}{dt} = \varepsilon\left[\frac{(1-\delta^2)}{(1+\delta^2)} \frac{I_p(\chi_s - 1)}{4} - \left(\frac{I_p \chi_p}{2} + 1 + d_1 S_0\right) f_2 - \left(\frac{(1-\delta^2)}{(1+\delta^2)} \frac{I_p \chi_p}{2} + d_1 S_1\right) \frac{f_1}{2}\right],$$

$$\frac{df_3}{dt} = -\varepsilon\left[\frac{d_1 S_2 f_1}{2} + \left(\frac{I_p \chi_p}{2} + 1 + d_1 S_0\right) f_3\right]. \tag{1.42}$$

σ_i are Stokes parameters of the injected δ–correlated stochastic signal:

$$\langle \sigma_i(t) \rangle_t = 0,\ \langle \sigma_i(t)\sigma_j(t-\tau) \rangle_t = \Sigma^2 \delta_{i,j}\delta(\tau), \quad \delta_{i,j} = \begin{cases} 1, i = j, \\ 0\ i \neq j. \end{cases}\ \delta(\tau) = \begin{cases} \infty, \tau = 0, \\ 0\ \tau \neq 0. \end{cases} \tag{1.43}$$

Here $\delta_{i,j}$ is the Kronecker symbol, δ(τ) is the Dirac function, $\sigma^2 = 1/\tau_c$, τ_c is the correlation time.

To obtain results shown in Figure 1.32, we used the following parameters: a)-i) $\Omega = 7, A_0 = 0.1$; a)-c) $\beta_L = 2\pi/\sqrt{5}, \beta_C = 0$; d)-f) $\beta_L = 2\pi/\sqrt{5}, \beta_C = \pi\sqrt{2}/\sqrt{5}$; g)-i) $\beta_L = 2\pi/\sqrt{5}, \beta_C = \pi\sqrt{4}/\sqrt{5}$. The other parameters: a)-i) α_1*=21.5,* α_2*=2.53,* I_p*=30,d=0.5* (elliptically polarized pump SOP), Δ*=0.1*, ε=10^{-4}, χ_p=1/0.75, χ_s=2.3, S=10^{-3}.

It was shown in section 12 that tuning the linear birefringence results in the vector resonance multimode instability (Sergeyev S.V. 2017). By adjusting the in-cavity and the pump wave polarization controllers, the birefringence strength can be increased and two satellite lines around the q-harmonic frequency emerge. Finally, longitudinal modes synchronization happens when the beat length equals the cavity length and so the frequencies of the satellites for q-harmonic are in resonance with the q+1-and q-1-harmonic.

The complexity of the vector model exceeds the complexity of any known scalar or vector models of fiber lasers considered elsewhere. Given the complexity of the problem, we use a few approximations to reveal the effect of the TR_{2m} on the modulation of the output power at frequency Ω. First, in the theoretical analysis, we accounted for the only interplay of the linear and circular birefringence with the TR_{2m} acoustic mode-based modulation for harmonic $q = 0$ in terms of the ability of excitation of the output power oscillations at a frequency of TR_{2m} mode.

The results of the theoretical analysis are shown in Figure 1.32a-i. As follows from Figure 1.32 a, b,d,e, the output power I and I_x, I_y are oscillating at frequency $\omega = \sqrt{\beta_L^2 + \beta_c^2}$ (Collett 2003),

whereas oscillations at the frequency Ω have almost been suppressed. Only for the case when the frequency $\Omega = 14\pi$ is a multiple of frequency $\omega = 2\pi$, the oscillations at the frequency ω disappear, and the output power is modulated at frequency Ω. This is like the experimental data shown in Figure 1.21, where HML is stabilized only when $\omega = 2\pi$, i.e. when the satellites' frequencies are matching the frequency spacing between harmonics. The HML mechanism looks like the vector mode-locking at the fundamental frequency (Sergeyev S 2021). By adjusting the in-cavity polarization controller POC2, we were able to increase the circular birefringence strength that leads to the generation of two satellite lines around the q=0 harmonic frequency. When the birefringence-based modulation frequency ω approaches the fundamental frequency, the modulation of the harmonic at the frequency ω disappears, and TR_{2m} is activation results in modulation of q=0 cavity mode with the frequency of TR_{2m}. The amplitude of the output power (Figure 1.32g) along with the Stokes parameters shown was small, and so SOP was locked (Figure 1.32i).

<Figure 1.32 here>

Figure 1.32. Results of the numerical modeling. a), d), g) The output power vs time for two linearly cross-polarized SOPs I_x (dashed line) and I_y (dots) and total power $I=I_x+I_y$(solid line); b), e), h) Spectrum of the oscillations; c), f), i) trajectories on the Poincare sphere. Parameters: time is normalized to the roundtrip time, frequency Ω – to the fundamental frequency; birefringence strengths β_L, β_C - to the fiber length; a)-i) $\Omega = 7, A_0 = 0.1$; ellipticity of the pump wave δ=0.5; a)-c) $\beta_L = 2\pi/\sqrt{5}, \beta_C = 0$; d)-f) $\beta_L =$

$2\pi/\sqrt{5}, \beta_C = 2\pi\sqrt{2}/\sqrt{5}$; g)-i) $\beta_L = 2\pi/\sqrt{5}, \beta_C = 2\pi\sqrt{4}/\sqrt{5}$. The other parameters are found in text.

The trajectories shown in Figure 1.32c and 1.32f are different from the experimentally observed (Figure 1.21d). However, the DOP=62 % in Figure 1.21d is indication that the SOP evolves at the time scale faster than the polarimeter resolution of 1 μs and, after averaging over 10 roundtrips, can merge to the dot at the Poincare sphere (Kbashi HJ. 2019). By using a low-pass filter (Hanning window with the transmission spectrum $T(f) = (1 + cos(\pi f/f_c))/2,\ f \le f_c = 1MHz$) we processed time domain waveforms shown in Figure 1.32c and found that circle was transformed to the dot with DOP=61.7 % that is close to the experimental data. The suppression of the oscillations at the frequency ω indicates that the linewidth is narrowing due to oscillations only at the frequency Ω (Figure 1.32h).

We highlight that the analysis of HML based on the excitation of TR_{2m} provides just a qualitative approach to the linewidth suppression. The presence of oscillations of the output power at the frequency of TR_{2m} mode and cancelation of the oscillations at the frequency related to the linear and circular birefringence results in narrowing the RF line and increased SNR of 30 dB as shown in Figure 1.22c.

1.16 SELF-PULSING IN FIBER LASERS (THEORY)

Output power self-pulsing (or self-Q-switching, SQS) in fiber lasers at frequencies of 10–100 kHz is a phenomenon resulting in emergence of auto-oscillations without external modulation (Toral-Acosta 2014, Mallek 2013, Lee 2010, S. O. Sergeyev 2010, Barmenkov 2004, Kir'yanov 2004, Le Boudec 1993, F. L. Sanchez 1995, F. S. Sanchez 1996). To explain variety of self-pulsing operations, the following mechanisms have been suggested: (i) effect of saturable absorber by unpumped section of active fiber

(Toral-Acosta 2014) or clustered erbium ions (Le Boudec 1993, F. L. Sanchez 1995, F. S. Sanchez 1996); (ii) stimulated Brillouin scattering (Mallek 2013), (iii) self-phase modulation (Lee 2010); (iv) coherence and anti-coherence resonance (CR an ACR) scenario where multimode and polarization instabilities play the role of an external noise source (S. O. Sergeyev 2010); (iv) the pump-to-signal intensity noise transfer (PSINT) (Barmenkov 2004), (v) power-dependent thermo-induced lensing in Er-doped fiber (Kir'yanov 2004). The X-ray-absorption fine structure spectroscopy (XAFS) has revealed a short-range coordination order (SRCO) of erbium ions rather than pair clustering (Peters 1998). Though in high concentration LIEKKI TM fibers SRCO is suppressed (Tammela 2003, S. a. Sergeyev 2007), however, SQS still presents (S. O. Sergeyev 2010). It has been also found, that the PSINT can contribute to low-frequency self-pulsing only slightly above the first lasing threshold (Barmenkov 2004). Also, coherence and CR and ACR are feasible scenarios but the models of CR and ACR-based self-pulsing have not been developed yet (S. O. Sergeyev 2010). Given that the saturable effect of unpumped active fiber, Brillouin scattering, and self-phase modulation have a high threshold, these mechanisms can be feasible only for high power Yb-doped lasers (Toral-Acosta 2014, Mallek 2013, Lee 2010). Power-dependent thermo-induced lensing can induce low-threshold self-pulsing (Kir'yanov 2004), but can't explain an origin of the experimentally observed complex self-pulsing regimes (Le Boudec 1993, F. L. Sanchez 1995).

In this section, we review a new concept of a tunable vector self-pulsing in Er-doped fiber laser developed by Sergeyev (S. Sergeyev 2016). The approach is based on Equations 1.42 . To reveal self-pulsing without a saturable absorber at frequencies less than the fundamental frequency of mode locking, linear stability along saddle index analysis (Tigan 2008) have been applied to find conditions for emerging complex vector attractors on the Poincare sphere as a function of the laser parameters such as the cavity birefringence, and power and ellipticity of the pump wave. Stability analysis was validated by numerical simulations which demonstrated that double scroll polarization attractor (DSPA) can exist as a

result of the polarization symmetry breaking in isotropic cavity without a saturable absorber whereas increased ellipticity of the pump wave and in-cavity birefringence leads to deformation of DSPA to chaotic attractor and further to limit cycle and stable focus. Thus, the obtained theoretical results provides an insight into the experimental data on the complex of self-pulsing regimes including chaos and rogue waves.

To describe evolution of the laser SOP on the Poincare sphere in terms of the Stokes parameters and the population of the first excited level in Er^{3+} doped active medium we use a simplified form of Equations 1.42:

$$\frac{dS_0}{dt} = \left(\frac{2\alpha_1 f_1}{1+\Delta^2} - 2\alpha_2\right) S_0 + \frac{2\alpha_1 f_2}{1+\Delta^2} S_1 + \frac{2\alpha_1 f_3}{1+\Delta^2} S_2,$$

$$\frac{dS_1}{dt} = \gamma S_2 S_3 + \frac{2\alpha_1 f_2}{1+\Delta^2} S_0 + \left(\frac{2\alpha_1 f_1}{1+\Delta^2} - 2\alpha_2\right) S_1 - \beta_c S_2 - \frac{2\alpha_1 f_3 \Delta}{1+\Delta^2} S_3,$$

$$\frac{dS_2}{dt} = -\gamma S_1 S_3 + \frac{2\alpha_1 f_3}{1+\Delta^2} S_0 + \beta_c S_1 + \left(\frac{2\alpha_1 f_1}{1+\Delta^2} - 2\alpha_2\right) S_2 + \frac{2\alpha_1 f_2 \Delta}{1+\Delta^2} S_3,$$

$$\frac{dS_3}{dt} = \frac{2\alpha_1 \Delta f_3}{1+\Delta^2} S_1 - \frac{2\alpha_1 \Delta f_2}{1+\Delta^2} S_2 + \left(\frac{2\alpha_1 f_1}{1+\Delta^2} - 2\alpha_2\right) S_3,$$

$$\frac{df_1}{dt} = \varepsilon\left[\frac{(\chi_s - 1) I_p}{2} - 1 - \left(1 + \frac{I_p \chi_p}{2} + d_1 S_0\right) f_1 - \left(d_1 S_1 + \frac{I_p \chi_p}{2}\frac{(1-\delta^2)}{(1+\delta^2)}\right) f_2 - d_1 S_2 f_3\right],$$

$$\frac{df_2}{dt} = \varepsilon\left[\frac{(1-\delta^2)}{(1+\delta^2)}\frac{I_p(\chi_s - 1)}{4} - \left(\frac{I_p \chi_p}{2} + 1 + d_1 S_0\right) f_2 - \left(\frac{(1-\delta^2)}{(1+\delta^2)}\frac{I_p \chi_p}{2} + d_1 S_1\right)\frac{f_1}{2}\right],$$

$$\frac{df_3}{dt} = -\varepsilon\left[\frac{d_1 S_2 f_1}{2} + \left(\frac{I_{p\chi_p}}{2} + 1 + d_1 S_0\right) f_3\right].$$

(1.44)

Next, equations 1.44 were linearized in the vicinity of the steady state solution ($S_0 \neq 0$, $S_1 = S_2 = 0$, $S_3 = \pm S_0$) and find numerically eigenvalues for the parameters quite close to the experimental ones (S. V. Sergeyev

2014) : *viz. L=17m, α_1=ln(10)6.4, α_4=ln(10)0.5, χ=3/2, Δ=0.1, I_p=10, γ=2x10^{-6}*, ε=10^{-4} . As a result, we find eigenvalues λ and saddle index ν as follows:

$$\lambda_0 = 0, \qquad \lambda_{1,2} = -\gamma_1 \pm i\omega_1, \qquad \lambda_{3,4} = -\gamma_2 \pm i\omega_2, \ \lambda_{5,6} = \rho \pm i\omega_3, \qquad \nu = \left|\frac{\gamma_1}{\rho}\right|$$

$$\left(\omega_{1,2,3} \neq 0, \ \rho, \gamma_1, \gamma_2 > 0, \ \gamma_1 > \gamma_2\right). \tag{1.45}$$

In view of eigenvalues for steady states ($S_0 \neq 0$, $S_1=S_2=0$, $S_3=S_0$) and ($S_0 \neq 0$, $S_1=S_2=0$, $S_3=-S_0$) are equal, conditions of the chaos existence in the neighborhood of the heteroclinic orbit can be written in the form of generalized Shilnikov theorem as follows: $\gamma^2>0$, $\rho^2>0$ and $\nu<1$ (Tigan 2008).

<Figure 1.33 here>

Figure 1.33 Saddle index ($\nu=|\mathrm{Re}\{\lambda_1\}/\mathrm{Re}\{\lambda_5\}|<1$) as a function of the pump power I_p , birefringence strength β and the anisotropy of pump $(1-\delta^2)/(1+\delta^2)$ in the vicinity of the steady state solution ($S_0 \neq 0$, $S_1=S_2=0$, $S_3=\pm S_0$). Parameters: *L=17m, α_1=ln(10)6.4, α_2=ln(10)0.5, χ=3/2, Δ=0.1, γ=2x10^{-6}*, ε=10^{-4}. The threshold pump power for cw operation $I_{p,th}=5.123$, the boundaries of self-pulsing for $\beta=0$, $\delta=1$: $I_{pmin}=5.134$, $I_{pmax}=140$.

The saddle index ν as a function of the anisotropy of the pump $(1-\delta^2)/(1+\delta^2)$ and birefringence strength β is shown in Figure 1.33. The internal area bounded by the surface shown in Fig. 33 and the surface $\nu=1$ defines the area of chaotic oscillations (Tigan 2008).

As follows from Figure 1.33 chaotic oscillations exist for the wide range of the pump power and very narrow range of ellipticity, and the cavity birefringence strength. Tunability of the dynamics with tuning

the ellipticity of the pump wave is shown in Figures 1.34 and 1.35. As follows from Figure 1.34, double scroll spiral attractor can exist without a saturable absorber (Figure 1.34, δ=1) and takes the forms of to the chaotic attractor, limit cycle and stable focus with increased ellipticity of the pump wave. However, with increased the birefringence strength, spiral attractor changes shape to the chaotic attractor and the limit cycle (Figure 1.35). As follows from Figure 1.36 (filled squares), increased birefringence results in modulation of the Stokes parameters with the frequency (2β-$\alpha_1 f_2\,\Delta/(1+\Delta^2)$) (Sergeyev S.V. 2017).

<Figure 1.34 here>

Figure 1.34 The calculated from Eqs. (1) dynamic waveforms and corresponding trajectories on the Poincare sphere as a function of ellipticity of the pump wave δ(I_p=20, β=0). Inset (IN1) shows auto-oscillations of the output power that corresponds to the double scroll polarization attractor. Parameters: *L=17m, α_1=ln(10)6.4, α_2=ln(10)0.5, χ=3/2, Δ=0.1, γ=2x10^{-6}*, ε=10^{-4}.

As follows from Figure 1.36, spiral attractor is transforming into the limit cycle for βL>0.017 and δ=1. However, for δ=0.9 chaotic oscillations of the output power is emerging again as a result of re-activation of oscillations close to the steady state of $S_0\neq0$, $S_1=S_2=0$, $S_3=\pm S_0$ (filled triangles in Fig. 36) and the presence of birefringence-driven oscillations around steady state $S_0\neq0$ $S_1=\pm S_0$, $S_2=S_3=0$ (filled squares in Figure 1.36). The complexity of demonstrated self-pulsing regimes can be interpreted based on the coupled oscillators theory (Pikovsky 2002, Arenas 2008, Thévenin 2011, Aronson DG 1990) where the phase difference $\Delta\varphi$ for two orthogonal linearly polarized modes plays the role of relative phase. The following equation for the phase difference $\Delta\varphi$ can be derived by using Equations 1.44:

$$\frac{d\Delta\varphi}{dt} = \Delta\Omega + K_{NL}\,sin^2(\Delta\varphi) + K_s\,sin(\Delta\varphi) + K_{as}\,cos(\Delta\varphi)\,,$$

$$\Delta\Omega = \frac{2\alpha_1 f_2 \Delta}{1+\Delta^2} - 2\beta, K_{NL} = \frac{\gamma L I_{ss}}{6}\left(I_y - I_x\right), K_s = -\frac{2\left(I_y + I_x\right)}{\sqrt{I_x I_y}}\frac{\alpha_1 f_3}{(1+\Delta^2)},$$

$$K_{as} = \frac{2\left(I_y - I_x\right)}{\sqrt{I_x I_y}}\frac{\alpha_1 f_3 \Delta}{(1+\Delta^2)}.$$

(1.46)

The Equation 1.46 is the further generalization of Adler equation (Pikovsky 2002, Arenas 2008, Thévenin 2011, Aronson DG 1990) based on accounting for asymmetry in the coupling of polarization modes (K_{as} coefficient) and polarization modes' coupling based on the Kerr effects (K_{NL}). In addition to this, I_x and I_y are also time-dependent variables.

As follows from the form of Equation 1.46 and 1.44, detuning $\Delta\Omega$ and coupling coefficients K_s, K_{as}, K_{NL} depend on the laser parameters and so mapping of different synchronization regimes (phase locking, phase entrainment with periodically oscillating phase and phase drifting with chaotically oscillating phase) can be done only numerically by using Equations 1.44 (S. Sergeyev 2016).

<Figure 1.35 here>

Figure 1.35 The calculated from Eqs. (1) dynamic waveforms and corresponding trajectories on the Poincare sphere as a function of the birefringence strength β (I_p=20). Parameters: *L=17m, α_1=ln(10)6.4, α_2=ln(10)0.5, χ=3/2, Δ=0.1, γ=2x10^{-6}*, $\varepsilon=10^{-4}$.

<Figure 1.36 here>

Figure 1.36 Frequency of self-pulsing (in red) and real part of the corresponding eigenvalue (in blue) in the vicinity of steady solution $S_0 \neq 0$, $S_1=S_2=0$, $S_3=\pm S_0$ (filled circles and empty and filled triangles) and $S_0 \neq 0$ $S_1=\pm S_0$, $S_2=S_3=0$ (filled squares and empty squares). Parameters: I_p=20, δ=1 (squares and empty triangles), δ=0.9 (filled triangles). Real part for eigenvalue in the vicinity of steady state $S_0 \neq 0$ $S_1=\pm S_0$,

$S_2=S_3=0$ (empty squares) is multiplied on 10^{-3}. All frequencies are normalized to the fundamental frequency which is inversely proportional to the round-trip time.

For example, the absence of self-pulsing for high pump power can be explained by the increased coupling strength between polarization modes to allow phase locking and so steady-state solution. The results of the phase difference evolution as a function of ellipticity of the pump wave and the birefringence strength are shown in Figure 1.37a,b. For $\beta=0$, it is possible to conclude that detuning is growing faster as compared to the coupling and so phase dynamics changes from the phase entrainment to the phase drift (curves 1 and 2 in Figure 1.37a) and chaotic self-pulsing while tuning ellipticity from $\delta=0.95$ to $\delta=0.9$. Further decreasing the ellipticity results in the faster growth of coupling that leads to the phase entrainment (curve 3 in Figure 1.37a) and periodic power oscillations with the increased frequency and, finally, in phase locked solution (curve 4 in Figure 1.37a) and steady-state regime for $\delta=0.8$. For circularly polarized pump ($\delta=1$) and increasing birefringence strength, phase difference dynamics is changing from the chaotic drift ($\beta=0.017$, curve 1 in Figure 1.37b) to the phase entrainment ($\beta=0.034$, curve 2 in Figure 1.37b) with the fast periodic oscillations of the phase difference and output power correspondently (Figure 1.34). Aforementioned resonance activation of the chaotic oscillations (Figure 1.34 and 1.35) for ($\delta=0.9$ and $\beta=0.034$) results in the chaotic phase drift (curve 3 in Figure 1.37b).

<Figure 1.37 here>

Figure 1.37a,b. The phase difference evolution. (a) $\beta=0$ and $\delta=0.95$ (curve 1), $\delta=0.9$ (2), $\delta=0.85$ (3), and $\delta=0.8$ (4); (b) $\delta=1$, $\beta=0.017$ (1); $\delta=1$, $\beta=0.034$ (2); $\delta=0.9$, $\beta=0.034$ (3). Parameters: $I_p=20$, $L=17m$, $\alpha_1=ln(10)6.4$, $\alpha_4=ln(10)0.5$, $\chi=3/2$, $\Delta=0.1$, $\gamma=2x10^{-6}$, $\varepsilon=10^{-4}$.

In conclusion, we demonstrate theoretically different vector self-pulsing scenarios in erbium-doped fiber laser. Unlike previous self-pulsing models modulation (Toral-Acosta 2014, Mallek 2013, Lee 2010, S. O. Sergeyev 2010, Barmenkov 2004, Kir'yanov 2004, Le Boudec 1993, F. L. Sanchez 1995, F. S. Sanchez 1996)., we reveal the emergence of the complex vector self-pulsing regimes in terms of the theory of synchronization of coupled oscillators as a transition from the phase locking to new types of phase entrainment and intermittent phase drift regimes as a function of coupling strength and detuning between oscillators' frequencies equation (Pikovsky 2002, Arenas 2008, Thévenin 2011, Aronson DG 1990).

References

Agrawal, G. P. 2013. *Nonlinear fiber optics (Academic press.* San Diego: Academic press.

Akhmediev, N., Kibler, B., Baronio, F., Belić, M., Zhong, W.P., Zhang, Y., Chang, W., Soto-Crespo, J.M., Vouzas, P., Grelu, P. and Lecaplain, C. 2016. "Roadmap on optical rogue waves and extreme events." *Journal of Optics* 18(6): 063001.

Arenas, A., Díaz-Guilera, A., Kurths, J., Moreno, Y. and Zhou, C. 2008. "Synchronization in complex networks." *Physics reports* 469(3): 93-153.

Aronson DG, Ermentrout GB, Kopell N. 1990. "Amplitude response of coupled oscillators." *Physica D 1990* 41: 403–449.

Barmenkov, Y.O. and Kir'yanov, A.V. 2004. "Pump noise as the source of self-modulation and self-pulsing in Erbium fiber laser. Optics express." *Optics express,* 12(14): 3171-3177.

Baronio, F., Degasperis, A., Conforti, M. and Wabnitz, S. 2012. "Solutions of the vector nonlinear Schrödinger equations: evidence for deterministic rogue waves." *Physical Review Letters* 109(4): 044102.

Benjamin, T.B. and Feir, J.E., 1967. 1967. "The disintegration of wave trains on deep water Part 1. Theory." *Journal of Fluid Mechanics* 27(3): 417-430.

Boscolo, S., Sergeyev, S.V., Mou, C., Tsatourian, V., Turitsyn, S., Finot, C., Mikhailov, V., Rabin, B. and Westbrook, P.S.,. 2014. "Nonlinear pulse shaping and polarization dynamics in mode-locked fiber lasers." *International Journal of Modern Physics B.* 28(12): 1442011.

Byrne, J.A., Gabitov, I.R., Kovačič, G. 2003. "Polarization switching of light interacting with a degenerate two-level optical medium." *Physica D* 2003: 69-92.

Chen, S., Grelu, P. and Soto-Crespo, J.M. 2014. "Dark-and bright-rogue-wave solutions for media with long-wave–short-wave resonance." *Physical Review E* 89(1): 011201.

Chouli, S. and Grelu, P. 2010. "Soliton rains in a fiber laser: An experimental study." *Physical Review A* 063829: 063829.

Collett, E. 2003. *Polarized light in fiber optics.* SPIE Press.

Cundiff, S.T., Collings, B.C., Akhmediev, N.N., Soto-Crespo, J.M., Bergman, K.,, and Knox, W.H. 1999. "Observation of Polarization-Locked Vector Solitons in an Optical Fiber." *Physical Review Letters* 82: 3988-3991.

Cundiff, S.T., Ye, J. 2003. "Colloquium: Femtosecond optical frequency combs. Reviews of Modern Physics." *Reviews of Modern Physics* 75(1): 325.

Desurvire, E. 1994. *Erbium-Doped Fiber Amplifiers, Principles and Applications.* New York: John Wiley & Sons.

Dudley, J.M., Dias, F., Erkintalo, M. and Genty, G. 2014. "Instabilities, breathers and rogue waves in optics." *Nature Photonics* 8(10): 755-764.

Faraday, M. 1831. "On a peculiar class of acoustical figures; and on certain forms assumed by

groups of particles upon vibrating elastic surfaces." *Philosophical transactions of the Royal Society of London* 121: 299-340.

Fontana, F., Begotti, M., Pessina, E.M. and Lugiato, L.A. 1995. "Maxwell-Bloch modelocking instabilities in erbium-doped fiber lasers." *Optics communications* 114(1-2): 89-94.

Fu, H., & Haken, H. 1987. 1987. "Semiclassical dye-laser equations and the unidirectional single-frequency operation." *Physical Review A* 36: 4802-4816.

Geng, Y., Zhou, H., Han, X., Cui, W., Zhang, Q., Liu, B., Deng, G., Zhou, Q. and Qiu, K. 2022. "Coherent optical communications using coherence-cloned Kerr soliton microcombs." *Nature communications* 13(1): 1-8.

Graham, R. and Haken, H. 1968. "Quantum theory of light propagation in a fluctuating laser-active medium." *Zeitschrift für Physik A Hadrons and nuclei* 213(5): 420-450.

Grelu, P., and Akhmediev, N. 2012. "Dissipative solitons for mode-locked lasers." *Nature photonics* 6: 84-92.

Grudinin, A.B. and Gray, S. 1997. "Passive harmonic mode locking in soliton fiber lasers." *JOSA B* 14(1): 144-154.

Gui, L. L., Xiao, X. S., and Yang, C. X. 2013. "Observation of various bound solitons in a carbon-nanotube-based erbium fiber laser." *JOSA B* 30: 158-164.

Haus, J.W., Shaulov, G, Kuzin, E.A., and Sanchez-Mondragon, J. 1999. "Vector soliton fiber lasers." *Optics Letters* 24: 376-378.

Heismann, F. 1994. "Analysis of a reset-free polarization controller for fast automatic polarization stabilization in fiber-optic transmission systems." *Journal of Lightwave Technology* 12(4): 690-699.

Hillerkuss, D., Schmogrow, R., Schellinger, T., Jordan, M., Winter, M., Huber, G.T. et al. 2011.

"26 Tbit s-1 21 line-rate super-channel transmission utilizing all-optical fast Fourier transform processing." *Nature Photonics* 5: 364-371.

Jiang, Y., Narushima, T., Okamoto, H. 2010. "Nonlinear optical effects in trapping nanoparticles with femtosecond pulses." *Nature Physics* 6: 1005-1009.

Kanda, N., Higuchi, T., Shimizu, H., Konishi, K., Yoshioka, K., and Kuwata-Gonokami, M. 2011. "The vectorial control of magnetization by light." *Nature Comunications* 2: 1-5.

Kbashi H., Sergeyev, S.V., Mou, C., Garcia, A.M., Araimi, M.A., Rozhin, A., Kolpakov, S. and Kalashnikov, V. 2018. "Bright-Dark Rogue Waves." *Annalen der Physik* 530(5): 1700362.

Kbashi H.J., Sergeyev, S.V., Al Araimi, M., Tarasov, N. and Rozhin, A., 2019. 2019. "Vector soliton rain." *Laser Physics Letters* 16(3): 035103.

Kbashi HJ., Sergeyev, S.V., Al-Araimi, M., Rozhin, A., Korobko, D. and Fotiadi, A. 2019. "High-frequency vector harmonic mode locking driven by acoustic resonances. Optics letters." *Optics Letters* 44(21): 5112-5115.

Kbashi, H.J., Zajnulina, M., Martinez, A.G. and Sergeyev, S.V. 2020. "Mulitiscale spatiotemporal structures in mode-locked fiber lasers." *Laser Physics Letters* 035103.

Khanin, YA. 2005. *Fundamentals of Laser Dynamics.* Cambridge: Cambridge International Science Publishing.

Kharif, C., Pelinovsky, E. and Slunyaev, A. 2008. *Rogue waves in the ocean.* Springer Science & Business Media.

Kim, I. and Lee, K.J. 2015. "Axial strain dependence of torsional acousto-optic gratings induced in a form-birefringence optical fiber. Journal of the Korean Physical Society." *Journal of the Korean Physical Society* 67(3): 465-471.

Kimel, A.V. and Li, M. 2019. "Writing magnetic memory with ultrashort light pulses." *Nature Reviews Materials* 4(3): 189-200.

Kir'yanov, A.V., Il'Ichev, N.N. and Barmenkov, Y.O. 2004. "Excited-state absorption as a source of nonlinear thermo-induced lensing and self-Q-switching in an all-fiber Erbium laser." *Laser Physics Letters* 1(4): 194.

Le Boudec, P., Jaouen, C., Francois, P.L., Bayon, J.F., Sanchez, F., Besnard, P. and Stephan, G. 1993. "Antiphase dynamics and chaos in self-pulsing erbium-doped fiber lasers." *Optics letters* 18(22): 1890-1892.

Lecaplain, C., Grelu, P. and Wabnitz, S. 2014. "LDynamics of the transition from polarization disorder to antiphase polarization domains in vector fiber lasers." *Physical Review A* 89(6): 063812.

Lee, H. and Agrawal, G.P. 2010. "Impact of self-phase modulation on instabilities in fiber lasers. IEEE journal of quantum electronics." *IEEE Journal of Quantum Electronics,* 46(12): 1732-1738.

Leners, R., Stéphan, G. 1995. "Rate equation analysis of a multimode bipolarization Nd3+ doped fibre laser." *Quantum and Semiclassical Optics: Journal of the European Optical Society Part B* 7(5): 757.

Li, F., Wai, P.K.A. and Kutz, J.N. 2010. "Geometrical description of the onset of multi-pulsing in mode-locked laser cavities." *JOSA B* 27(10): 2068-2077.

Li, X. L., Zhang, S. M., Meng, Y. C., Hao, Y. P., Li, H. F. et al. 2012. "Observation of soliton bound states in a graphene mode locked erbium-doped fiber laser." *Laser Physics* 22: 774-777.

Liu, X. and Pang, M. 2019. "Revealing the buildup dynamics of harmonic mode-locking states in

ultrafast lasers." *Laser & Photonics Reviews* 13(9): 1800333.

Lugiato, L., Prati, F. and Brambilla, M. 2015. *Nonlinear optical systems.* Cambridge University Press.

MacPhail-Bartley, I., Wasserman, W.W., Milner, A.A. and Milner, V. 2020. "Laser control of molecular rotation: Expanding the utility of an optical centrifuge." *Review of Scientific Instruments* 91(4): 045122.

Mallek, D., Kellou, A., Leblond, H. and Sanchez, F. 2013. "Instabilities in high power fiber lasers induced by stimulated Brillouin scattering." *Optics Communications* 308: 130-135.

Mandon, J., Guelachvili, G., and Picqué, N. 2009. "Fourier transform spectroscopy with a laser frequency comb." *Nature Photonics* 25: 99-102.

Misawa, K. 2016. "Applications of polarization-shaped femtosecond laser pulses." *Advances in Physics: X* 1(4): 544-569.

Mou Ch., Sergeyev, S.V., Rozhin, A.G. and Turitsyn, S.K. 2013. "Bound state vector solitons with locked and precessing states of polarization." *Optics express* 21(22): 26868-26875.

Mou, Ch., Sergeyev, S.V., Rozhin, A., and Turitsyn, S.K. 2011. "All-fiber polarization locked vector soliton laser using carbon nanotubes." *Optics letters* 36: 3831-3833.

Niang, A., Amrani, F., Salhi, M., Grelu, P. and Sanchez, F. 2014. "Rains of solitons in a figure-of-eight passively mode-locked fiber laser." *Applied Physics B* 116(3): 771-775.

Onorato M., Waseda, T., Toffoli, A., Cavaleri, L., Gramstad, O., Janssen, P.A.E.M., Kinoshita, T., Monbaliu, J., Mori, N., Osborne, A.R. and Serio, M. 2009. "Statistical properties of directional ocean waves: the role of the modulational instability in the formation of extreme events." *Physical Review Letters* 102(11): 114502.

Onorato, M., Residori, S., Bortolozzo, U., Montina, A. and Arecchi, F.T. 2013. "Rogue waves

and their generating mechanisms in different physical contexts. Physics Reports." *Physics Reports* 528(2: 47-89.

Ortac, B., Zavyalov, A., Nielsen, C. K., Egorov, O., Iliew R. et al. 2010. "Observation of soliton molecules with independently evolving phase in a mode-locked fiber laser." *Optics Letters* 35: 1578-1580.

Ovsyannikov IM, Shilnikov LP. 1987. "On systems with a saddle-focus homoclinic curve. Math." *Mathematics of the USSR-Sbornik* 58: 557–574.

Pang, M., X. Jiang, W. He, G. K. L. Wong, G. Onishchukov, N. Y. Joly, G. Ahmed, C. R. Menyuk, and P. St J. Russell. 2015. "Stable subpicosecond soliton fiber laser passively mode-locked by gigahertz acoustic resonance in photonic crystal fiber core." *Optica* 2: 339-342.

Peccianti, M., Pasquazi, A., Park, Y., Little, B.E., Chu, S.T., Moss, D.J. and Morandotti, R. 2012. "Demonstration of a stable ultrafast laser based on a nonlinear microcavity." *Nature communications* 3(1): 1-6.

Perego, A.M., Tarasov, N., Churkin, D.V., Turitsyn, S.K. and Staliunas, K. 2016. "Pattern generation by dissipative parametric instability." *Physical Review letters* 116(2): 028701.

Pessina, E.M., Bonfrate, G., Fontana, F. and Lugiato, L.A. 1997. "Experimental observation of the Risken-Nummedal-Graham-Haken multimode laser instability." *Physical Review A* 56(5): 4086.

Pessina, E.M., Prati, F., Redondo, J., Roldán, E. and De Valcarcel, G.J. 1999. "Multimode instability in ring fiber lasers." *Physical Review A* 60(3): 2517.

Peters, P.M., Houde-Walter, S.N. 1998. "Local structure of Er3+ in multicomponent glasses." *Journal of non-crystalline solids* 239(1-3): 162-169.

Picqué, N. and Hänsch, T.W. 2019. "2019. Frequency comb spectroscopy." *Nature Photonics* 13(3): 146-157.

Pikovsky, A., Rosenblum, M. and Kurths, J. 2002. *Synchronization: a universal concept in nonlinear science.* Cambridge : Cambridge University Press.

Pilipetskii, A.N., Luchnikov, A.V. and Prokhorov, A.M. 1993. "Soliton pulse long-range interaction in optical fibres: the role of light polarization and fibre geometry. Soviet lightwave communications." *Soviet lightwave communications* 3(1): 29-39.

Pupeza, I., Zhang, C., Högner, M. and Ye, J. 2021. "Extreme-ultraviolet frequency combs for precision metrology and attosecond science." *Nature Photonics* 15(3): 175-186.

Quiroga-Teixeiro, M., Clausen, C.B., Sørensen, M.P., Christiansen, P.L. and Andrekson, P.A. 1998. "Passive mode locking by dissipative four-wave mixing." *JOSA B* 15(4): 1315-1321.

Risken, H. and Nummedal, K. 1968. "Instability of off resonance modes in lasers." *Physics Letters A* 26(7): .275-276.

Rohrmann, P., Hause, A., Mitschke, F. 2012. "Solitons Beyond Binary: Possibility of Fibre-Optic Transmission of Two Bits per Clock Period." *Scientific Reports* 2: 866.

Sanchez, F., LeFlohic, M., Stephan, G.M., LeBoudec, P. and Francois, P.L. 1995. "Quasi-periodic route to chaos in erbium-doped fiber laser." *IEEE journal of quantum electronics* 31(3): 481-488.

Sanchez, F.., Stephan, G. 1996. "General analysis of instabilities in erbium-doped fiber lasers. Physical Review E." *Physical Review E* 53(3): 2110.

Seong, N. H., Kim, D. Y. 2002. "Experimental observation of stable bound solitons in a figure-eight fiber laser." *Optics Letters* 27: 1321-1323.

Sergeyev S, Kolpakov, S. and Loika, Y. 2021. "Vector harmonic mode-locking by acoustic resonance." *Photonics Research* 9(8): 1432-1438.

Sergeyev S., Kbashi, H., Mou, C., Martínez, A., Kolpakov, S. and Kalashnikov, V. 2018. "Vector rogue waves driven by polarisation instabilities." In *Nonlinear Guided Wave Optics: A testbed for extreme waves*, by S. Wabnitz, 9-1. IOP Publishing Ltd.

Sergeyev S.V., Kbashi, H., Tarasov, N., Loiko, Y. and Kolpakov, S.A. 2017. "Vector-resonance-multimode instability." *Physical review letters* 118(3): 033904.

Sergeyev, S. 2003. "Model of high-concentration erbium-doped fibre amplifier: effects of migration and upconversion processes." *Electronics Letters* 39(6): 511-512.

Sergeyev, S. and Khoptyar, D. 2007. "Theoretical and experimental study of migration-assisted upconversion in high-concentration erbium doped silica fibers." *Laser Optics: Solid State Lasers and Nonlinear Frequency Conversion.* 151-158.

Sergeyev, S. 1999. "Spontaneous Light Polarization Symmetry Breaking for an anisotropic ring cavity dye laser." *Physical Review A* 59: 3909- 3917.

Sergeyev, S. V. 1996. "Orientational-relaxation dependent bichromatic operations of a ring cavity dye laser with polarized pumping." *Optics Communications* 131(4-6): 399-407.

Sergeyev, S., Kolpakov, S. and Loika, Y. 2021. "Vector harmonic mode-locking by acoustic resonance." *Photonics Research* 9(8): 1432-1438.

Sergeyev, S., Popov, S., and Friberg, A.T. 2005. "Influence of the short-range coordination order of erbium ions on excitation migration and upconversion in multicomponent glasses." *Optics Letters* 30(11): 1258-1260.

Sergeyev, S., Popov, S., Khoptyar, D., Friberg, A.T. and Flavin, D. 2006. "Statistical model of migration-assisted upconversion in a high-concentration erbium-doped fiber amplifier."

JOSA B 23(8): 1540-1543.

Sergeyev, S.V. 2014. "Fast and slowly evolving vector solitons in mode-locked fibre lasers." *Philosophical Transactions of the Royal Society A: Mathematical, Physical and Engineering Sciences* 372(2027): 20140006.

Sergeyev, S.V., Eliwa, M., Kbashi, H. 2022. "Polarization attractors driven by vector soliton rain."

Sergeyev, Sergey V., Mou, C., Rozhin, A. and Turitsyn, S.K. 2012. "Vector solitons with locked and precessing states of polarization." *Optics Express* 20(24): 27434-27440.

Sergeyev, Sergey V., Mou, Ch., Turitsyna, E.G., Rozhin, A., Turitsyn, S.K. and Blow, K. 2014. "Spiral attractor created by vector solitons." *Light: Science & Applications* 3(1): e131-e131.

Sergeyev, SV. 2016. "Vector self-pulsing in erbium-doped fiber lasers." *Optics letters* 41(20): 4700-4703.

Sergeyev, SV., O'Mahoney, K., Popov, S. and Friberg, A. 2010. "Coherence and anticoherence resonance in high-concentration erbium-doped fiber laser." *Optics letters* 35(22): 3736-3738.

Shelby, R.M., Levenson, M.D. and Bayer, P.W. 1985. "Guided acoustic-wave Brillouin scattering. Physical Review B." *Physical Review B* 31(8): 5244.

Solli, D.R., Ropers, C., Koonath, P. and Jalali, B. 2007. "Optical rogue waves. Nature." *Nature* 450(7172): 1054-1057.

Soto-Crespo, J. M., Grelu, Ph., Akhmediev, N., & Devine, N. 2007. "Soliton complexes in dissipative systems: Vibrating, shaking, and mixed soliton pairs." *Physical Review E* 75: 016613.

Spanner, M., Davitt, K.M., and Ivanova, M.Yu. 2001. "Stability of angular confinement and rotational acceleration of a diatomic molecule in an optical centrifuge." *Journal of Chemical Physics* 115: 8403-8410.

Sulimany, K., Lib, O., Masri, G., Klein, A., Fridman, M., Grelu, P., Gat, O. and Steinberg, H. 2018. "Bidirectional soliton rain dynamics induced by casimir-like interactions in a graphene mode-locked fiber laser." *Physical Review Letters* 121(13): 13390.

Sylvestre, T., Coen, S., Emplit, P. and Haelterman, M. 2002. "Self-induced modulational instability laser revisited: normal dispersion and dark-pulse train generation." *Optics Letters* 27(7): 482-484.

Szwaj, C., Bielawski, S., Derozier, D. and Erneux, T. 1998. "Faraday instability in a multimode laser." *Physical Review Letters* 80: 3968.

Tammela, S., Hotoleanu, M., Kiiveri, P., Valkonen, H., Sarkilahti, S. and Janka, K. 2003. "Very short Er-doped silica glass fiber for L-band amplifiers." *Optical Fiber Communication Conference.* Optical Society of America. WK3.

Tang, D.Y., Zhang, H., Zhao, L.M., and Wu, X. 2008. "Observation of High-Order Polarization-Locked Vector Solitons in a Fiber Laser." *Physical Review Letters* 101: 153904.

Thévenin, J., Romanelli, M., Vallet, M., Brunel, M. and Erneux, T. 2011. "Resonance assisted synchronization of coupled oscillators: frequency locking without phase locking." *Physical review letters,* 107(10): 104101.

Tigan, G. and Opriş, D. 2008. "Analysis of a 3D chaotic system." *Chaos, Solitons & Fractals,* 36(5): 1315-1319.

Tlidi, M., Staliunas, K., Panajotov, K., Vladimirov, A.G. and Clerc, M.G. 2014. "Localized structures in dissipative media: from optics to plant ecology." *Philosophical Transactions*

of the Royal Society A: Mathematical, Physical and Engineering Sciences 372: 20140101.

Tong, L., Miljković, V.D., and Käll, M. 2010. "Alignment, Rotation, and Spinning of Single Plasmonic Nanoparticles and Nanowires Using Polarization Dependent Optical Forces." *Nano Letters* 10: 268-273.

Toral-Acosta, D., Martinez-Rios, A., Selvas-Aguilar, R., Kir'yanov, A.V., Anzueto-Sanchez, G. and Duran-Ramirez, V.M. 2014. "Self-pulsing in a large mode area, end-pumped, double-clad ytterbium-doped fiber laser. Laser Physics." *Laser Physics* 24(10): 105107.

Tsatourian V, Sergeyev, S.V., Mou, C., Rozhin, A., Mikhailov, V., Rabin, B., Westbrook, P.S. and Turitsyn, S.K. 2013. "Polarisation dynamics of vector soliton molecules in mode locked fibre laser." *Scientific reports* 3(1): 1-8.

Tsatourian V., Sergeyev, S.V., Mou, C., Rozhin, A., Mikhailov, V., Rabin, B., Westbrook, P.S. and Turitsyn, S.K. 2013. "Fast polarimetry of multipulse vector soliton operation." *39th European Conference and Exhibition on Optical Communication (ECOC 2013).* 1-3.

Turitsyna, E.G., Smirnov, S.V., Sugavanam, S., Tarasov, N., Shu, X., Babin, S.A., Podivilov, E.V., Churkin, D.V., Falkovich, G. and Turitsyn, S.K. 2013. "The laminar–turbulent transition in a fibre laser." *Nature Photonics* 7: 783-786.

Udem, Th., Holzwarth, R., Hänsch, T.W. 2002. "Optical frequency metrology." *Nature* 416: 233-237.

Van Wiggeren, G.D., Roy, R. 2002. "Communication with Dynamically Fluctuating States of Light Polarization." *Physical Review Letters* 88: 097903.

Varshalovich, D. A., Moskalev, A. N., & Khersonskii, V. K. 1988. *Quantum Theory of Angular Momentum.* Singapore: World Scientific.

Voigt, T., Lenz, M.O., Mitschke, F., Roldán, E. and De Valcarcel, G.J. 2004. "Experimental investigation of Risken–Nummedal–Graham–Haken laser instability in fiber ring lasers." *Applied Physics B* 79(2): 175-183.

Wang, X., Sun, M., Liang, Q., Yang, S., Li, S. and Ning, Q. 2020. "Observation of diverse structural bound-state patterns in a passively mode-locked fiber laser." *Applied Physics Express* 13(2): 022009.

Weill, R., Bekker, A., Smulakovsky, V., Fischer, B. and Gat, O. 2016. "Noise-mediated Casimir-like pulse interaction mechanism in lasers." *Optica* 3(2): 189-192.

Willemsen, M.B., van Exter, M.P., Woerdman, J.P. 2001. "Polarization loxodrome of a vertical-cavity semiconductor laser." *Optics Communications* 199: 167-173.

Williams, Q. L., and Roy, R. 1996. "Fast polarization dynamics of an erbium-doped fiber ring laser." *Optics Letters* 21: 1478-1480.

Wu, X., Tang, D. Y., Luan, X. N., and Zhang, Q. 2011. "Bound states of solitons in a fiber laser mode locked with carbon nanotube saturable absorber." *Optics communications* 284: 3615-3618.

Yan, Z.Y. 2010. "Financial rogue waves." *Communications in Theoretical Physics* 54(5): 947.

Zakharov, V.E. and Ostrovsky, L.A. 2009. "Modulation instability: the beginning." *Physica D: Nonlinear Phenomena* 238(5): 540-548.

Zavyalov, A., Iliew, R., Egorov, O., & Lederer, F. 2009. "Dissipative soliton molecules with independently evolving or flipping phases in mode-locked fiber lasers." *Physical Review A* 80: 043829.

Zeghlache, H., Boulnois, A. 1995. "Polarization instability in lasers. I. Model and steady states of neodymium-doped fiber lasers." *Physical Review A* 52: 4229-4242.

Zhang, H., Tang, D.Y., Zhao, L.M., and Wu, X. 2009. "Observation of polarization domain wall solitons in weakly birefringent cavity fiber lasers." *Physical Review E* 80: 052302.

Zhao, L.M., Tang, D.Y., Zhang, H., and Wu, X. 2008. "Polarization rotation locking of vector solitons in a fiber ring laser." *Optics Express* 16: 10053-10058.

Zhao, X., Li, T., Liu, Y., Li, Q. and Zheng, Z. 2018. "Polarization-multiplexed, dual-comb all-fiber mode-locked laser." *Photonics Research,* 6(9),: 853-857.

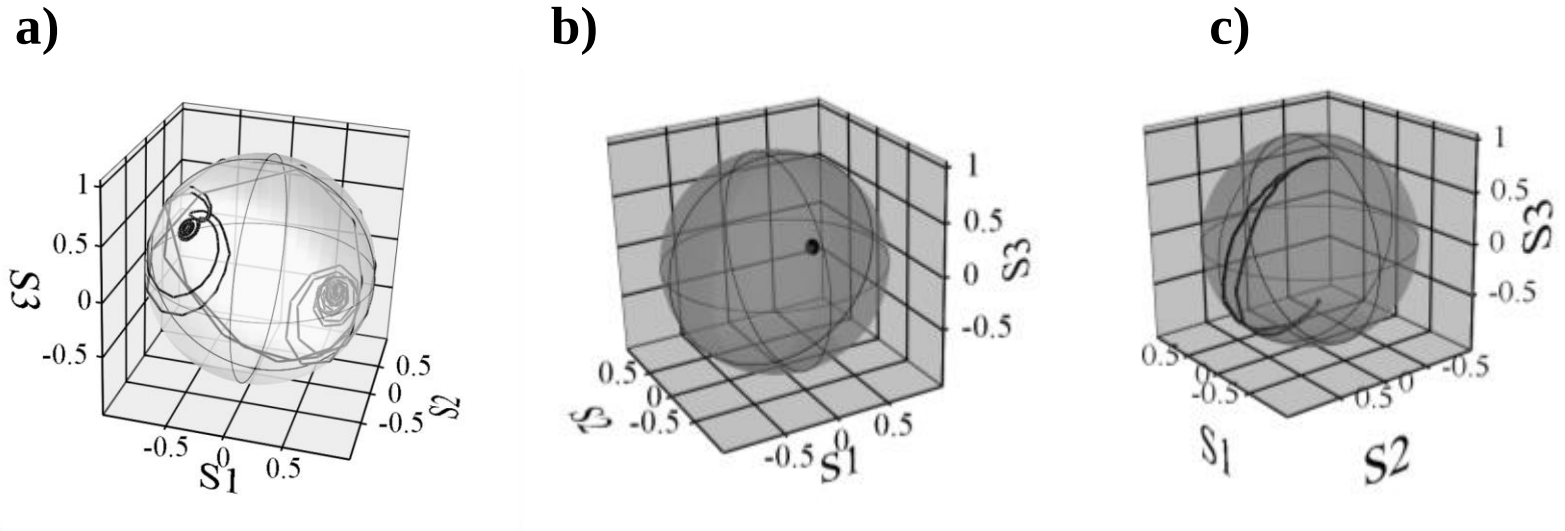

Fig. 2

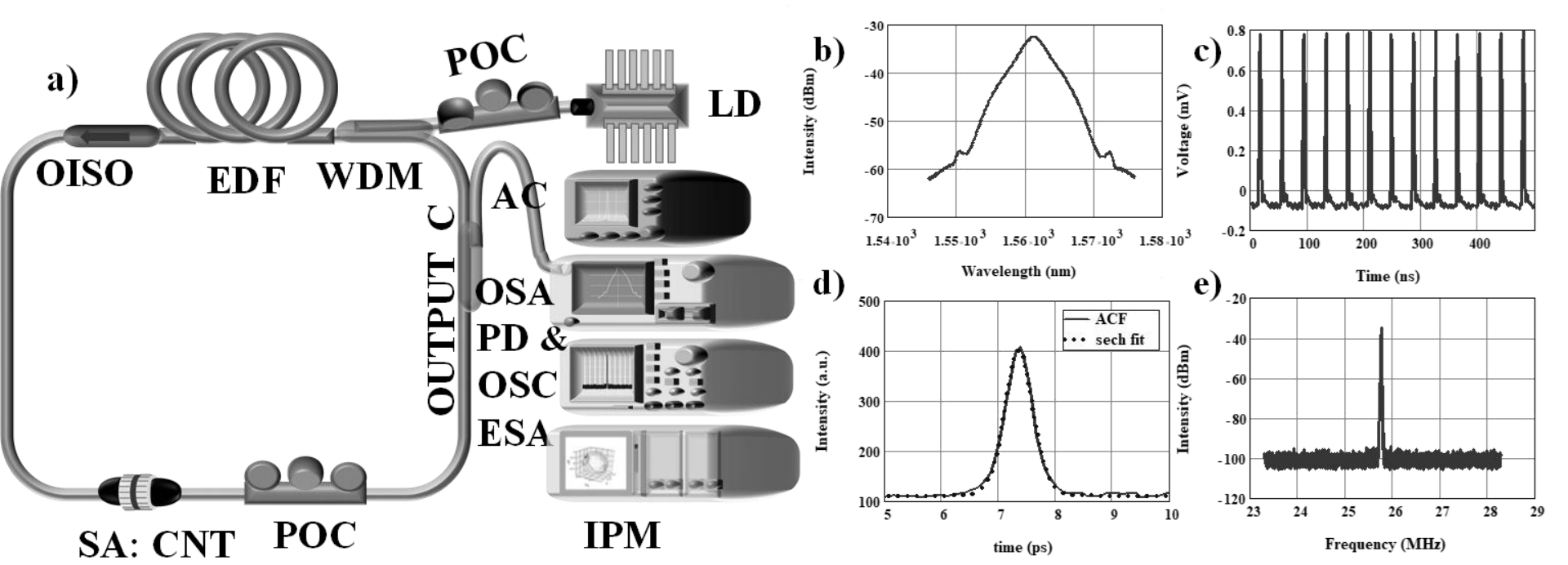
a)
POC
LD
OISO
EDF
WDM
AC
OUTPUT C
OSA
PD &
OSC
ESA
SA: CNT
POC
IPM
b)
Intensity (dBm)
-30
-40
-50
-60
-70
1.54·10^3
1.55·10^3
1.56·10^3
1.57·10^3
1.58·10^3
Wavelength (nm)
c)
Voltage (mV)
0.8
0.6
0.4
0.2
0
-0.2
0
100
200
300
400
Time (ns)
d)
Intensity (a.u.)
500
400
300
200
100
ACF
sech fit
5
6
7
8
9
10
time (ps)
e)
Intensity (dBm)
-20
-40
-60
-80
-100
-120
23
24
25
26
27
28
29
Frequency (MHz)

Fig. 1

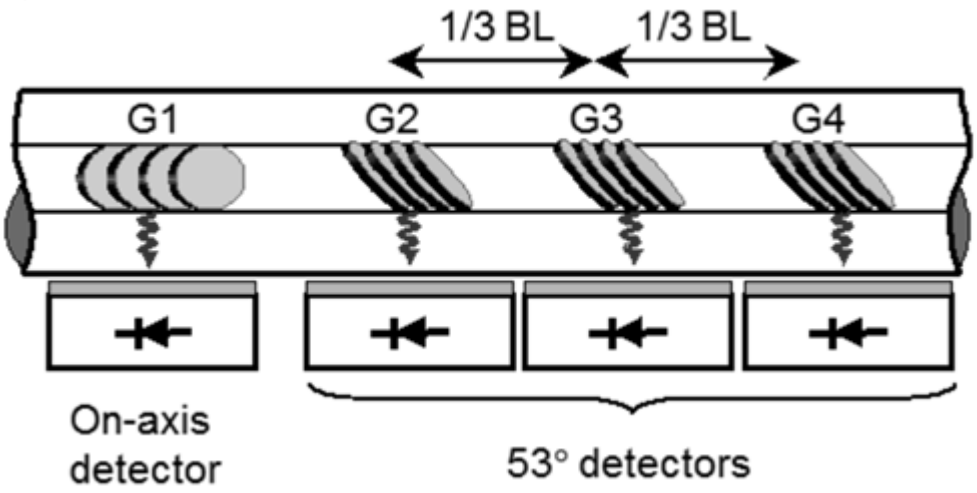

Fig. 3

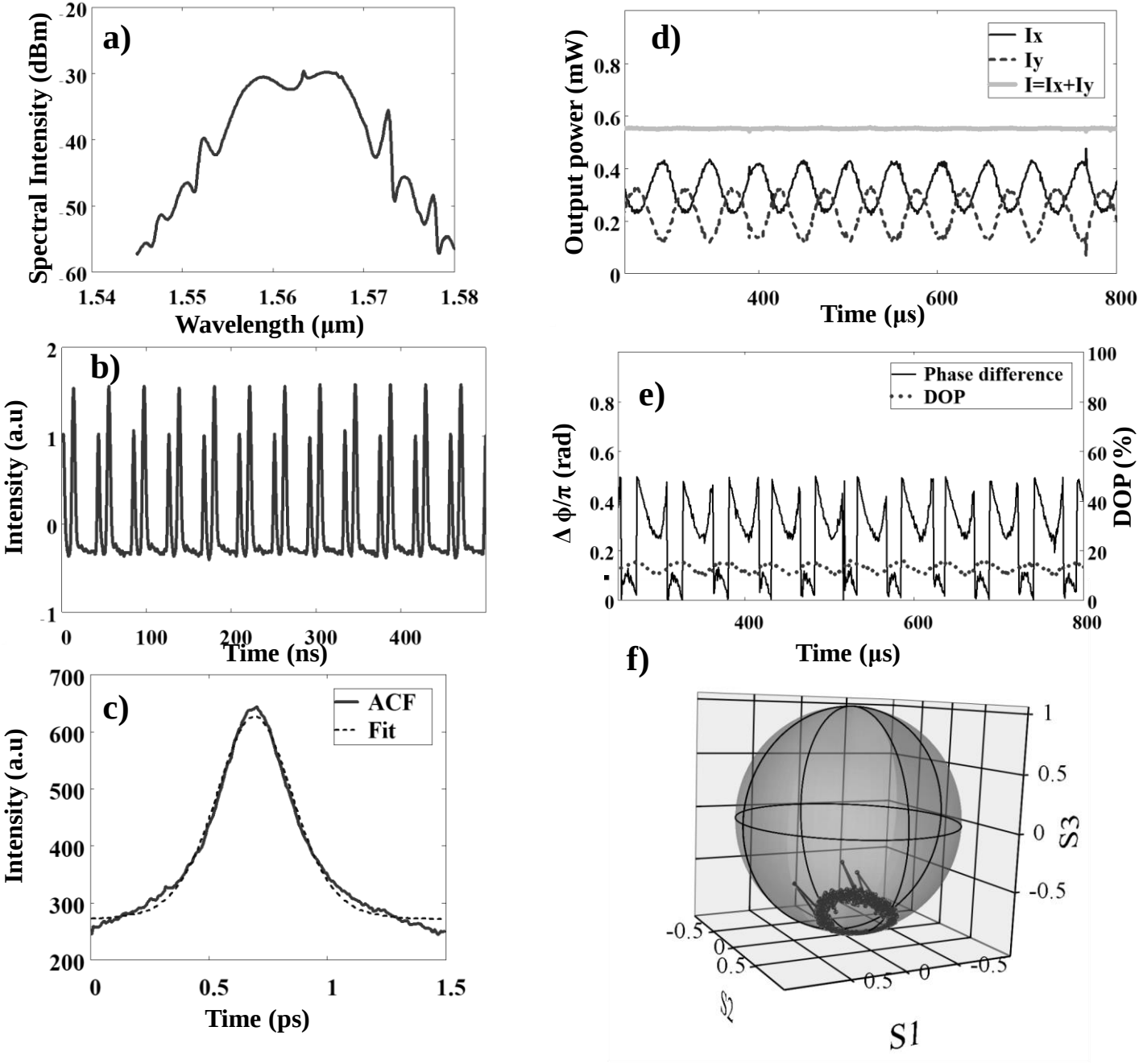
a)
Spectral Intensity (dBm)
Wavelength (μm)
b)
Intensity (a.u)
Time (ns)
c)
ACF
Fit
Intensity (a.u)
Time (ps)
d)
Ix
Iy
I=Ix+Iy
Output power (mW)
Time (μs)
e)
Phase difference
DOP
Δ ϕ/π (rad)
DOP (%)
Time (μs)
f)
S1
S2
S3

Fig. 4

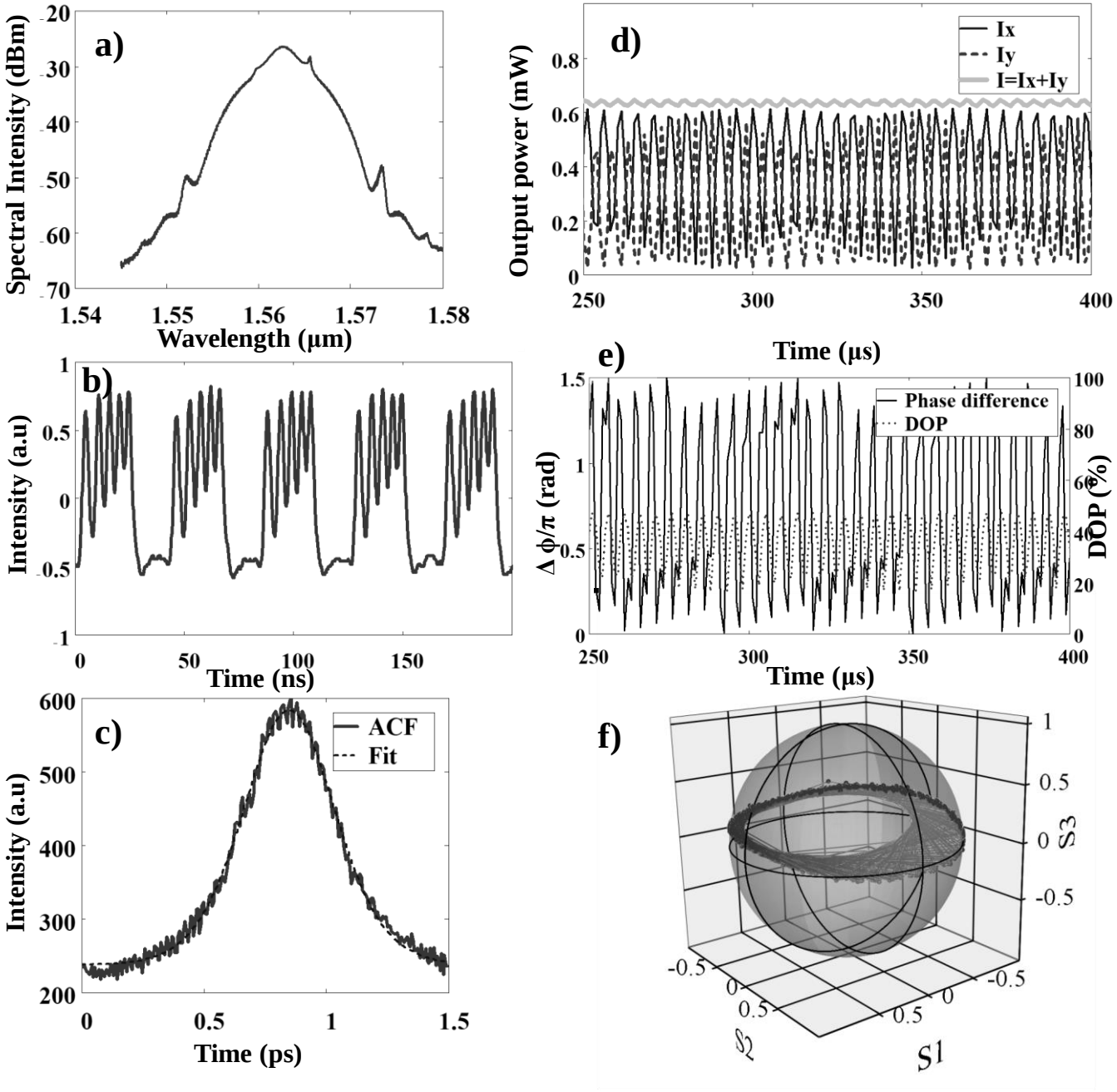
a)
Spectral Intensity (dBm)
Wavelength (μm)
b)
Intensity (a.u)
Time (ns)
c)
ACF
Fit
Intensity (a.u)
Time (ps)
d)
Ix
Iy
I=Ix+Iy
Output power (mW)
Time (μs)
e)
Phase difference
DOP
Δ ϕ/π (rad)
DOP (%)
Time (μs)
f)
S1
S2
S3

Fig. 5

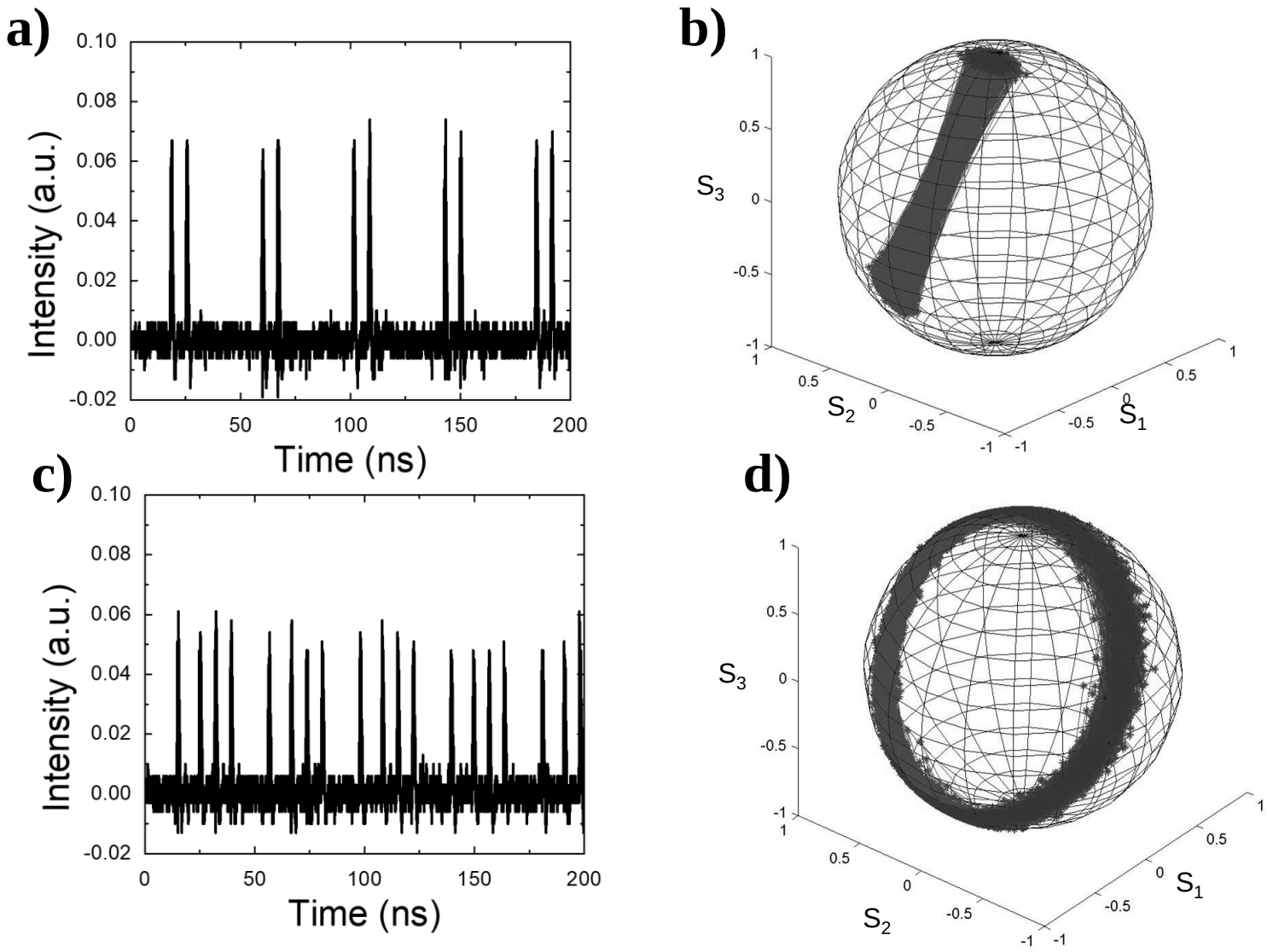
a)
Intensity (a.u.)
Time (ns)
b)
S3
S2
S1
c)
Intensity (a.u.)
Time (ns)
d)
S3
S2
S1

Fig. 6

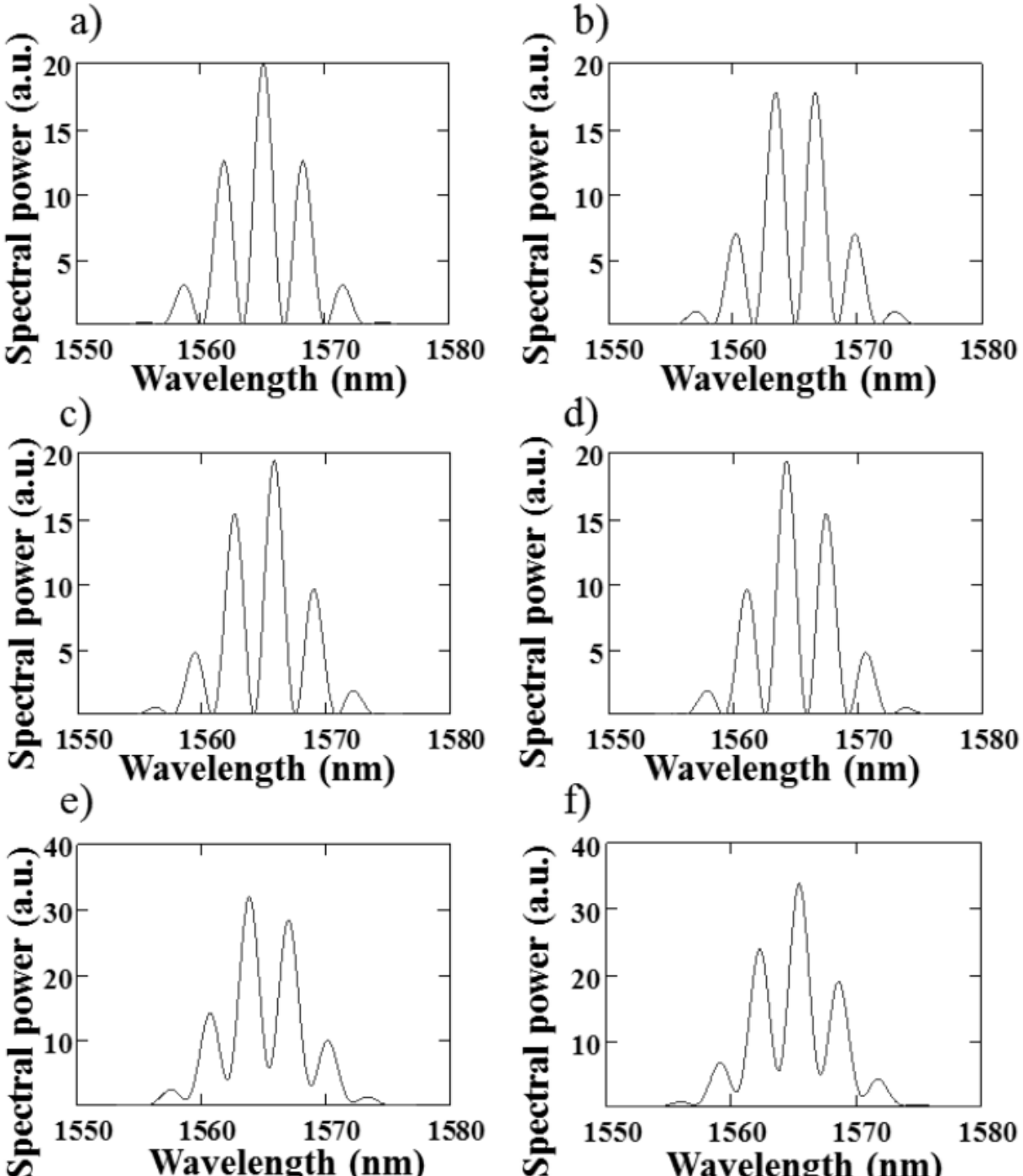
a)
b)
c)
d)
e)
f)
Spectral power (a.u.)
Wavelength (nm)
1550
1560
1570
1580
5
10
15
20
30
40

Fig.7

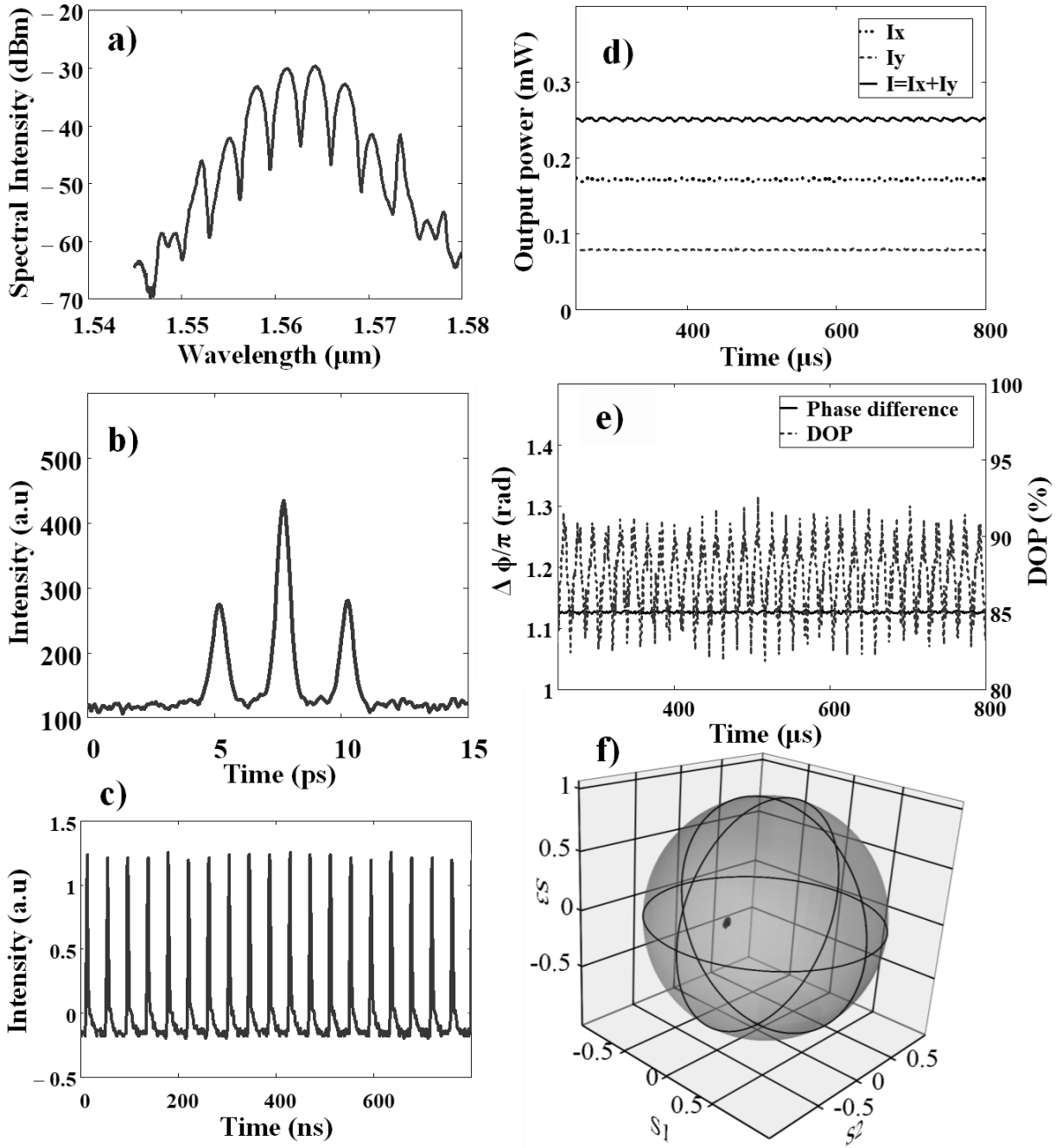
a)
Spectral Intensity (dBm)
Wavelength (μm)
b)
Intensity (a.u)
Time (ps)
c)
Intensity (a.u)
Time (ns)
d)
Ix
Iy
I=Ix+Iy
Output power (mW)
Time (μs)
e)
Phase difference
DOP
Δ ϕ/π (rad)
DOP (%)
Time (μs)
f)
S1
S2
S3

Fig. 8

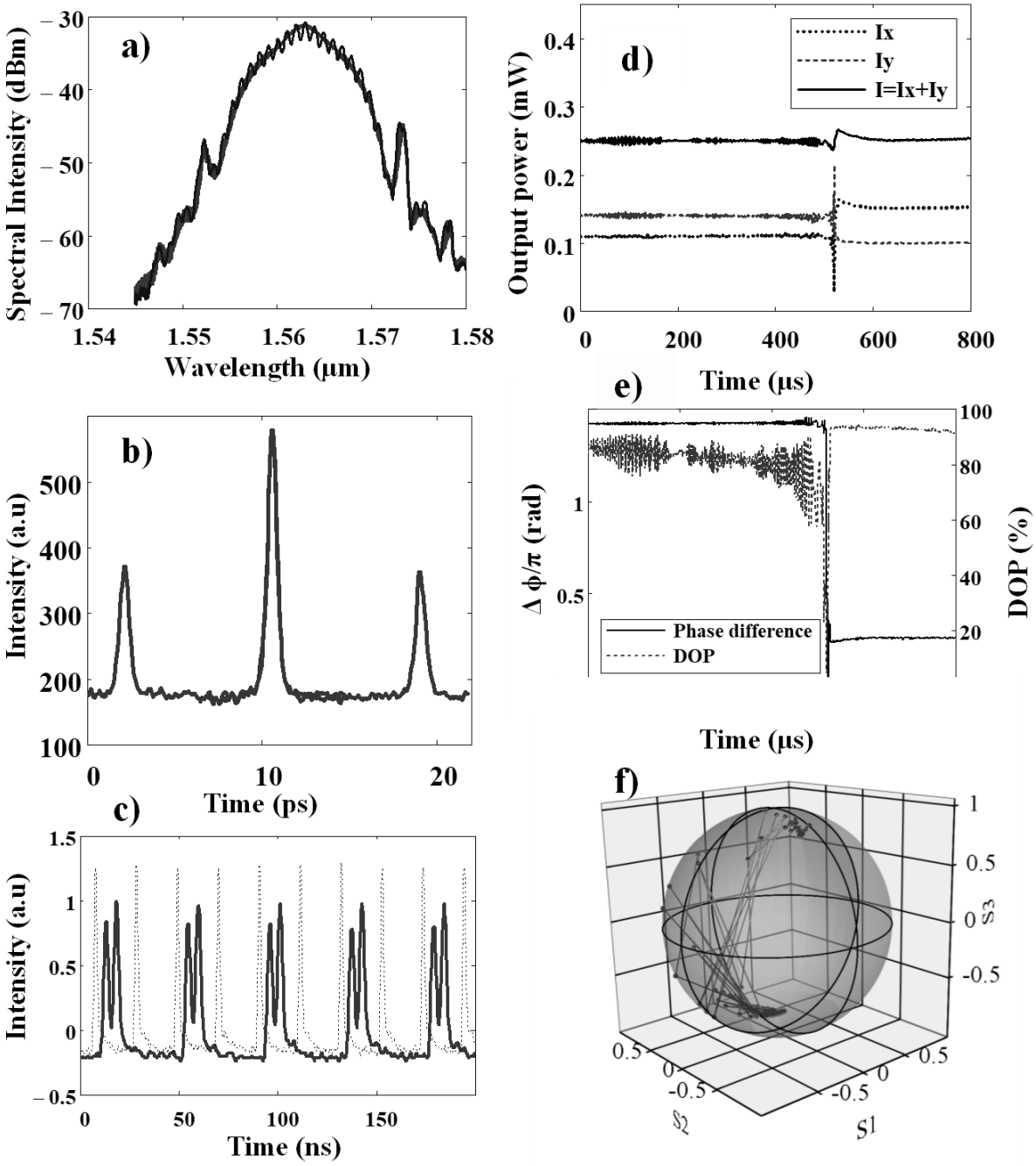
a)
Spectral Intensity (dBm)
Wavelength (μm)
b)
Intensity (a.u)
Time (ps)
c)
Intensity (a.u)
Time (ns)
d)
Ix
Iy
I=Ix+Iy
Output power (mW)
Time (μs)
e)
Δ ϕ/π (rad)
DOP (%)
Phase difference
DOP
Time (μs)
f)
S1
S2
S3

Fig. 9

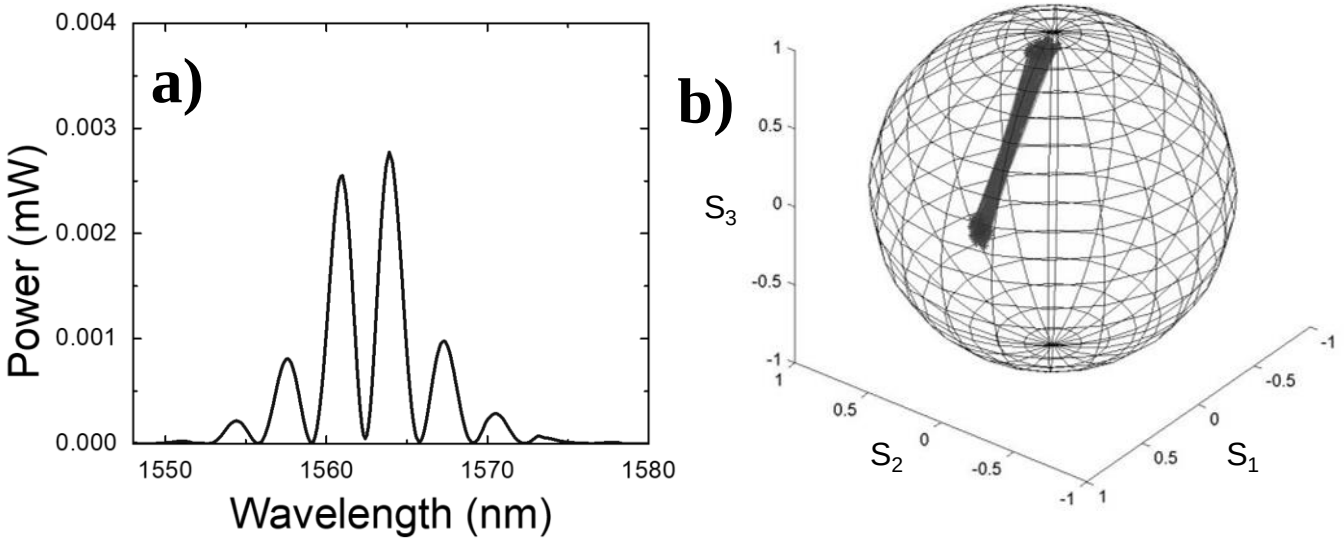
a)
b)
Power (mW)
Wavelength (nm)
0.004
0.003
0.002
0.001
0.000
1550
1560
1570
1580
S_3
S_2
S_1
1
0.5
0
-0.5
-1

Fig. 10

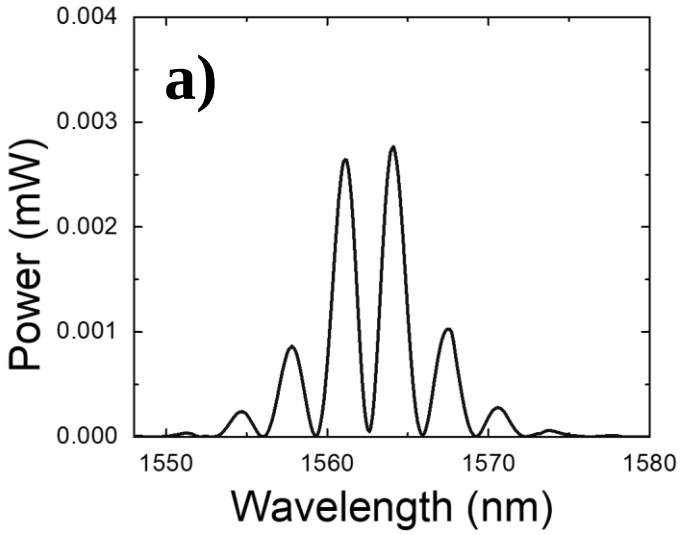
a)
0.004
0.003
0.002
0.001
0.000
Power (mW)
1550
1560
1570
1580
Wavelength (nm)

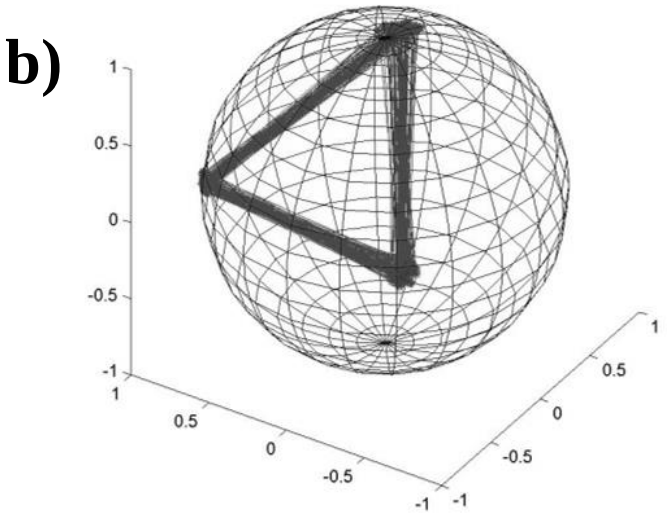
b)
1
0.5
0
-0.5
-1

Fig. 11

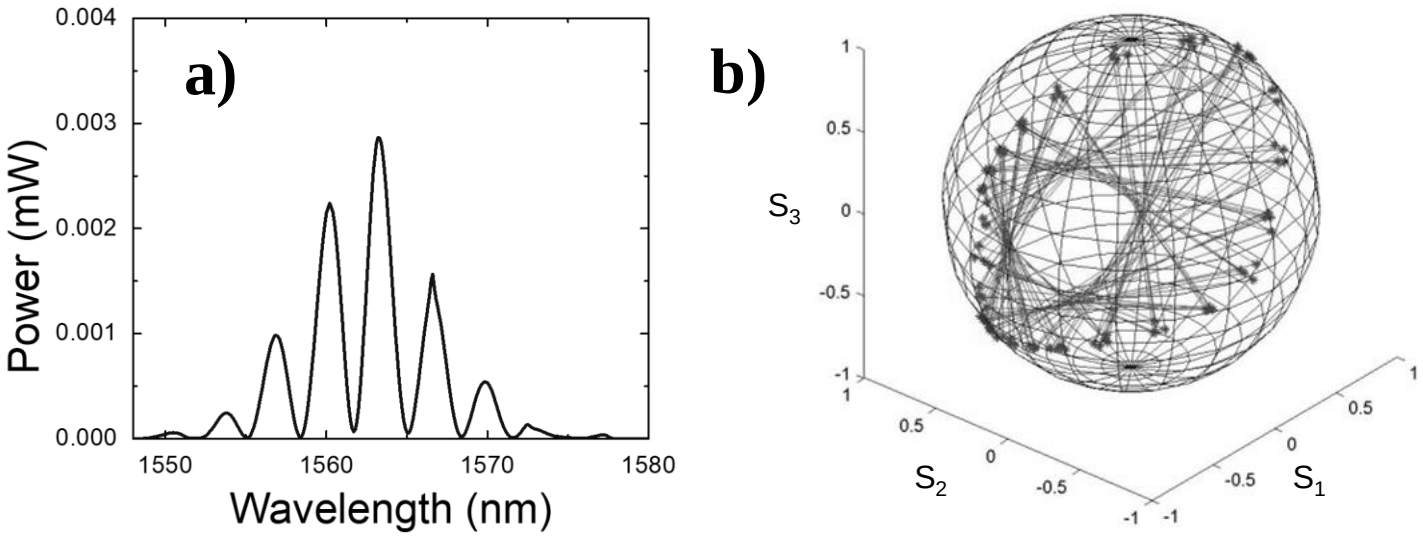
a)
b)
Power (mW)
Wavelength (nm)
0.004
0.003
0.002
0.001
0.000
1550
1560
1570
1580
S3
S2
S1
1
0.5
0
-0.5
-1

Fig. 12

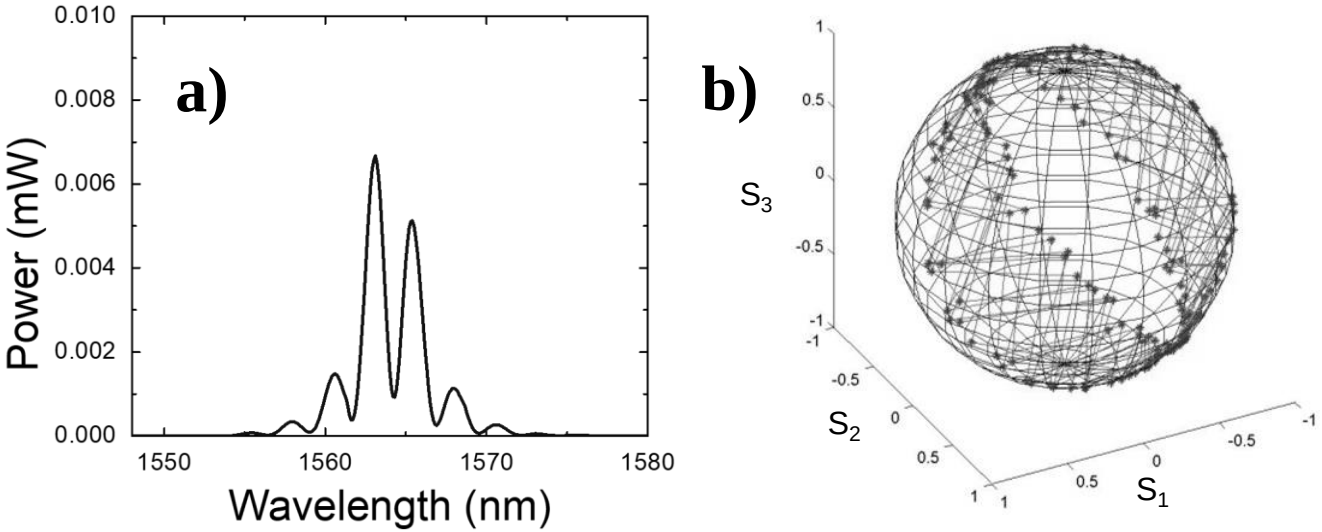
a)
b)
Power (mW)
0.010
0.008
0.006
0.004
0.002
0.000
1550
1560
1570
1580
Wavelength (nm)
S3
S2
S1
1
0.5
0
-0.5
-1

Fig. 13

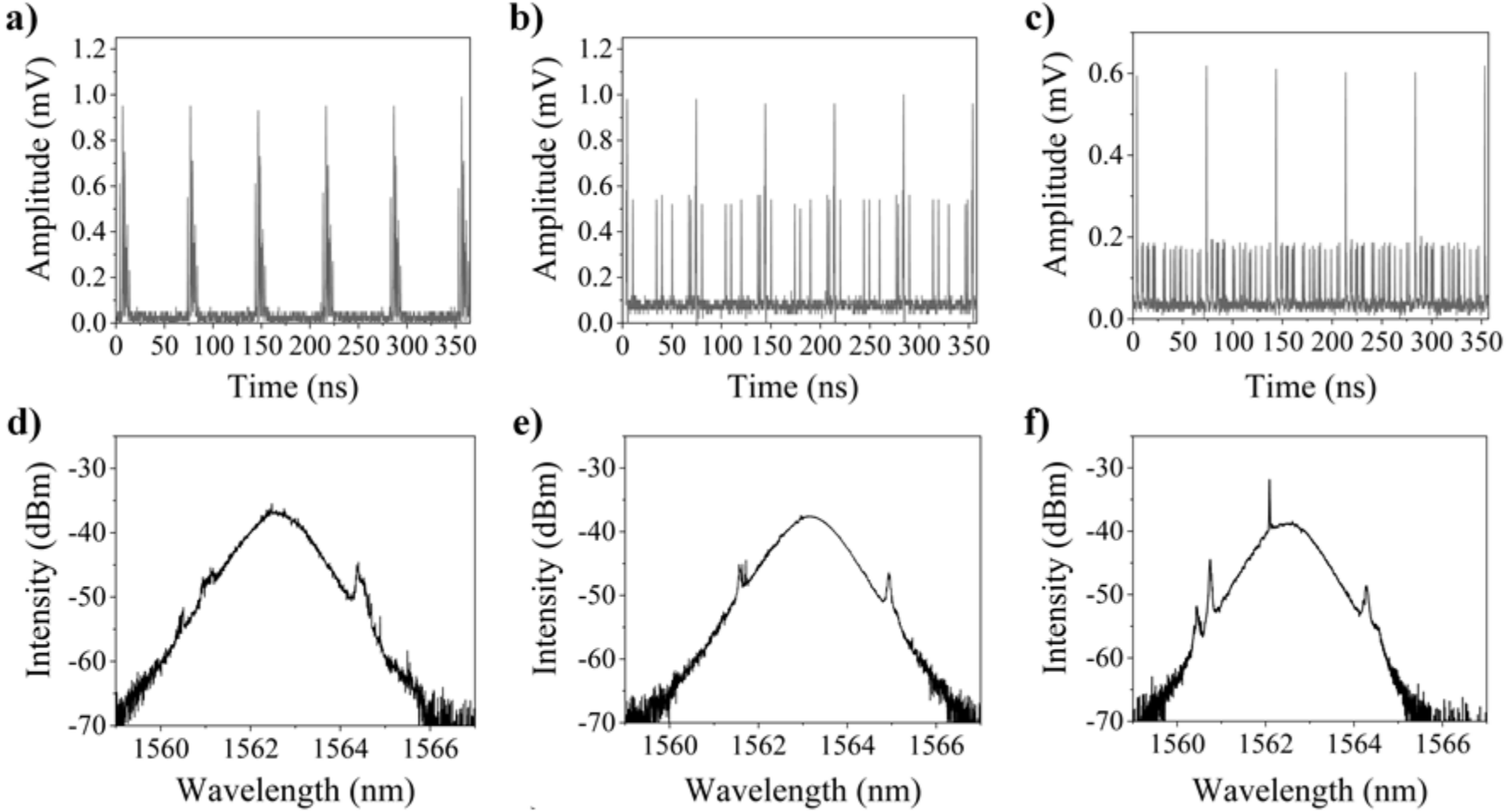

Fig. 14

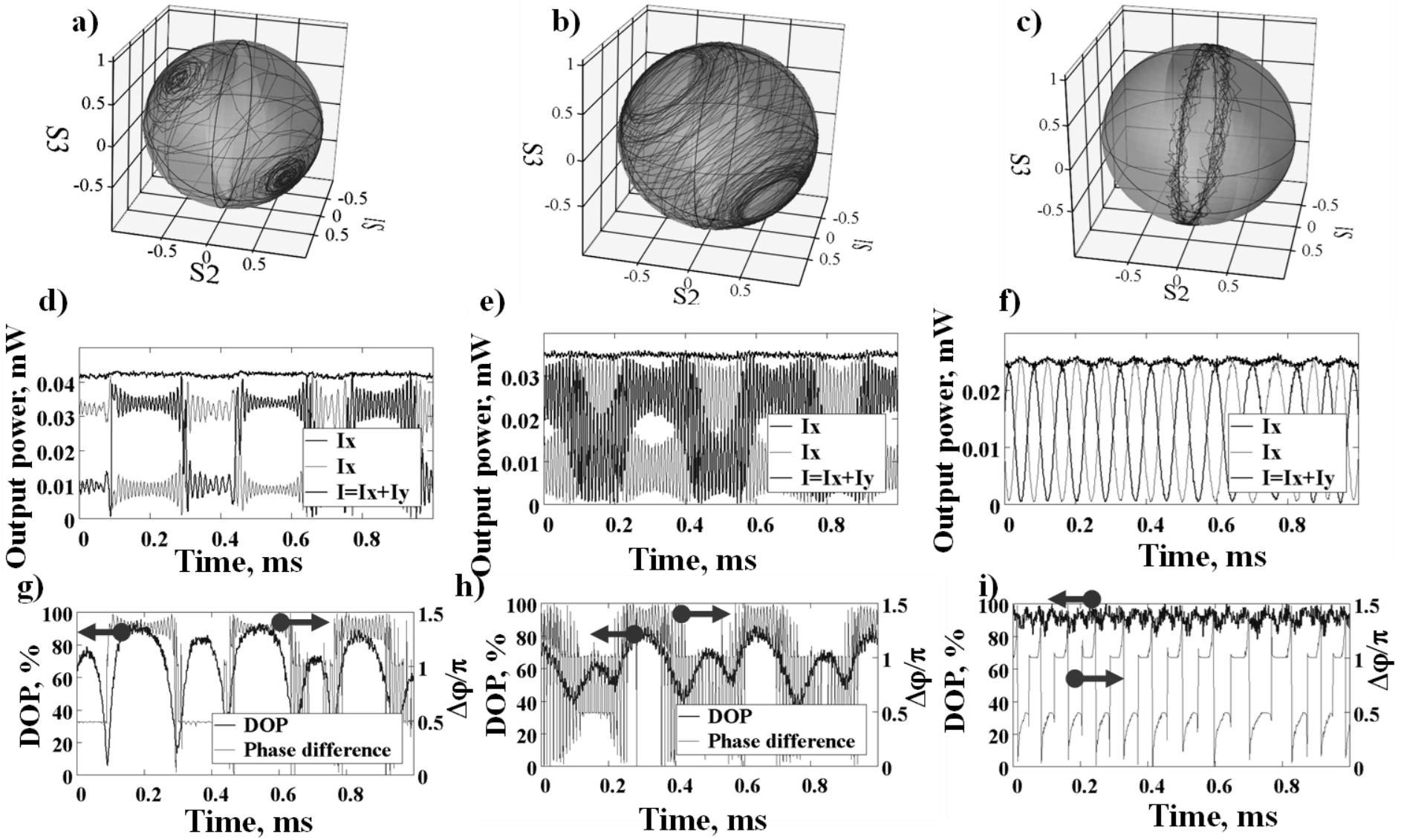
a)
b)
c)
S3
S2
S1
d)
e)
f)
Output power, mW
Time, ms
Ix
Ix
I=Ix+Iy
g)
h)
i)
DOP, %
Δφ/π
DOP
Phase difference

Fig. 15

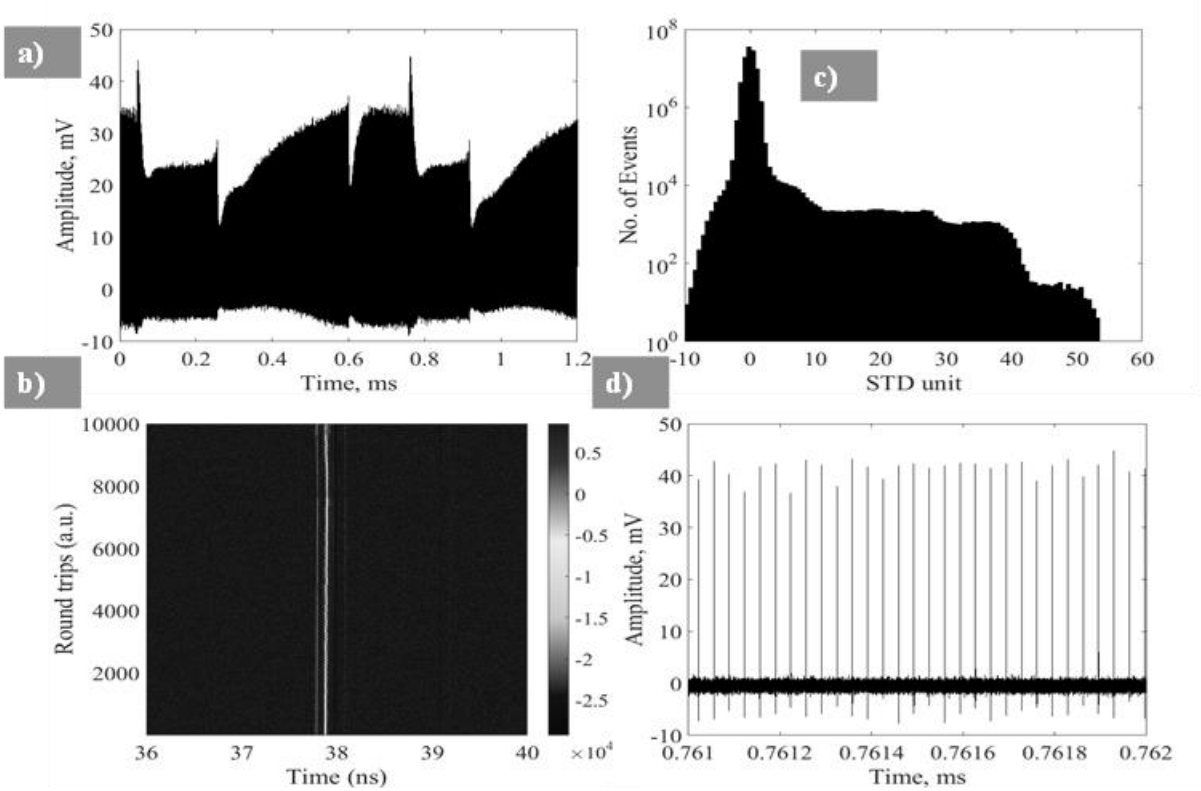
a)
Amplitude, mV
Time, ms
b)
Round trips (a.u.)
Time (ns)
×10^4
c)
No. of Events
STD unit
d)
Amplitude, mV
Time, ms

Fig. 16

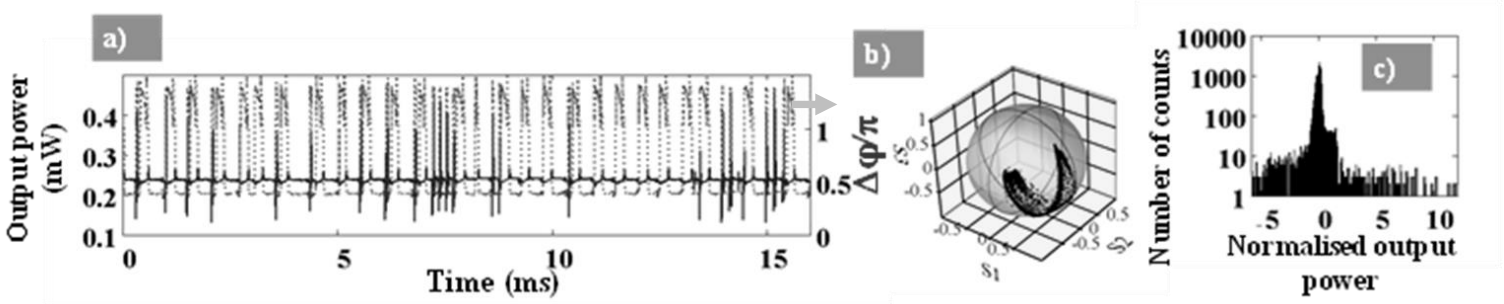
a)
Output power (mW)
0.4
0.3
0.2
0.1
0
5
10
15
Time (ms)
1
0.5
0
Δφ/π
b)
S3
S1
S2
c)
Number of counts
10000
1000
100
10
1
-5
0
5
10
Normalised output power

Fig. 17

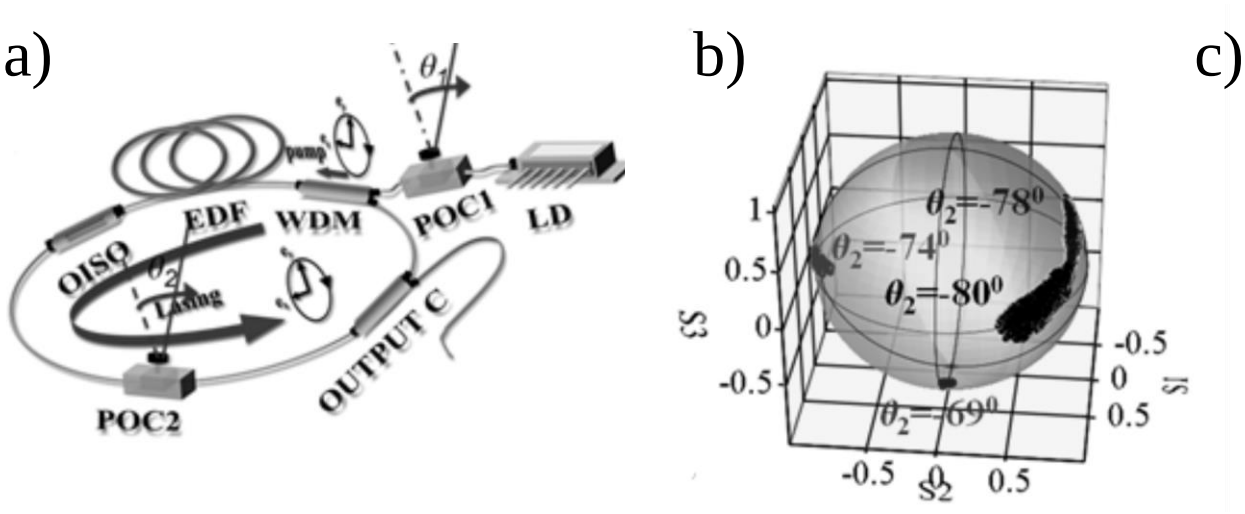
a)
b)
c)
pump
EDF
WDM
POC1
LD
OISO
Lasing
OUTPUT C
POC2
θ_1
θ_2
θ_2=-78^0
θ_2=-74^0
θ_2=-80^0
θ_2=-69^0
S3
S2
S1
Output power S_0 (mW)
Phase difference $\Delta\varphi/\pi$ (a.u)
DOP (%)
Time (ms)
Time (ms)

Fig. 18

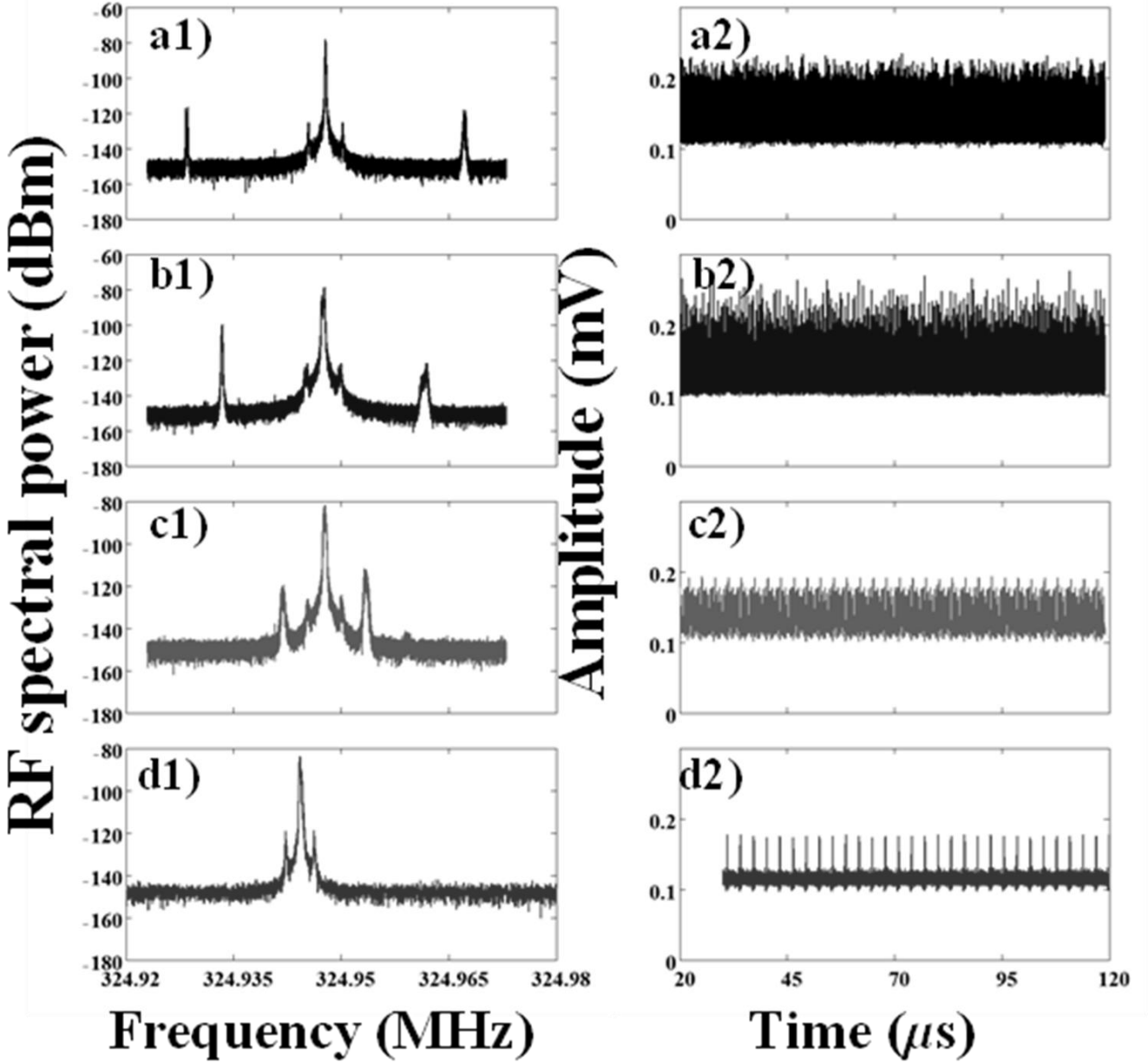
a1)
b1)
c1)
d1)
a2)
b2)
c2)
d2)
RF spectral power (dBm)
Amplitude (mV)
Frequency (MHz)
Time (μs)
-60
-80
-100
-120
-140
-160
-180
0.2
0.1
0
324.92
324.935
324.95
324.965
324.98
20
45
70
95
120

Fig. 19

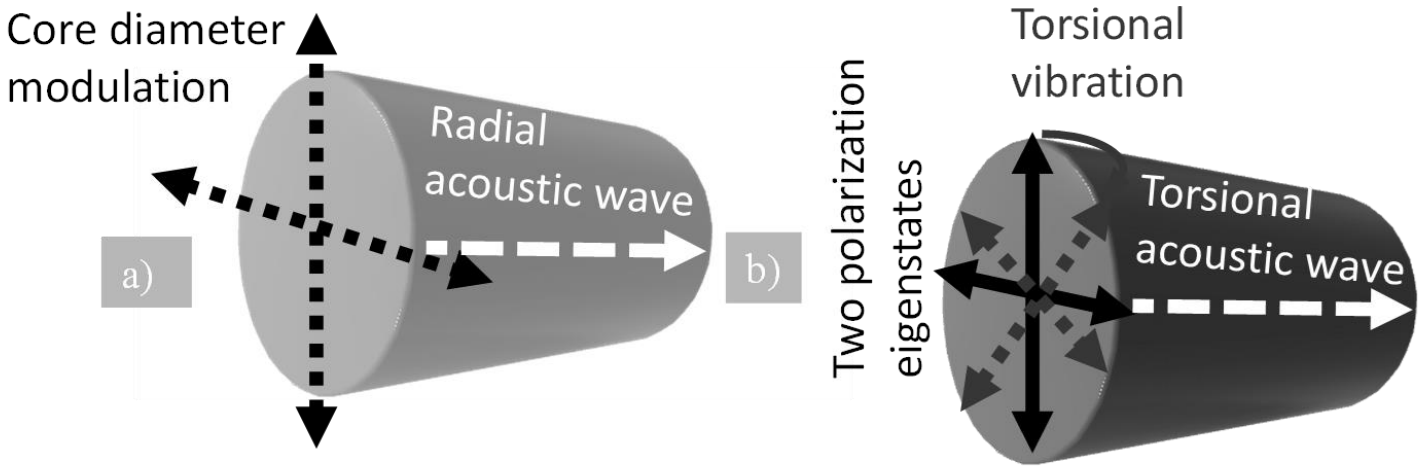
Core diameter
modulation
Radial
acoustic wave
a)
b)
Torsional
vibration
Two polarization
eigenstates
Torsional
acoustic wave

Fig. 20

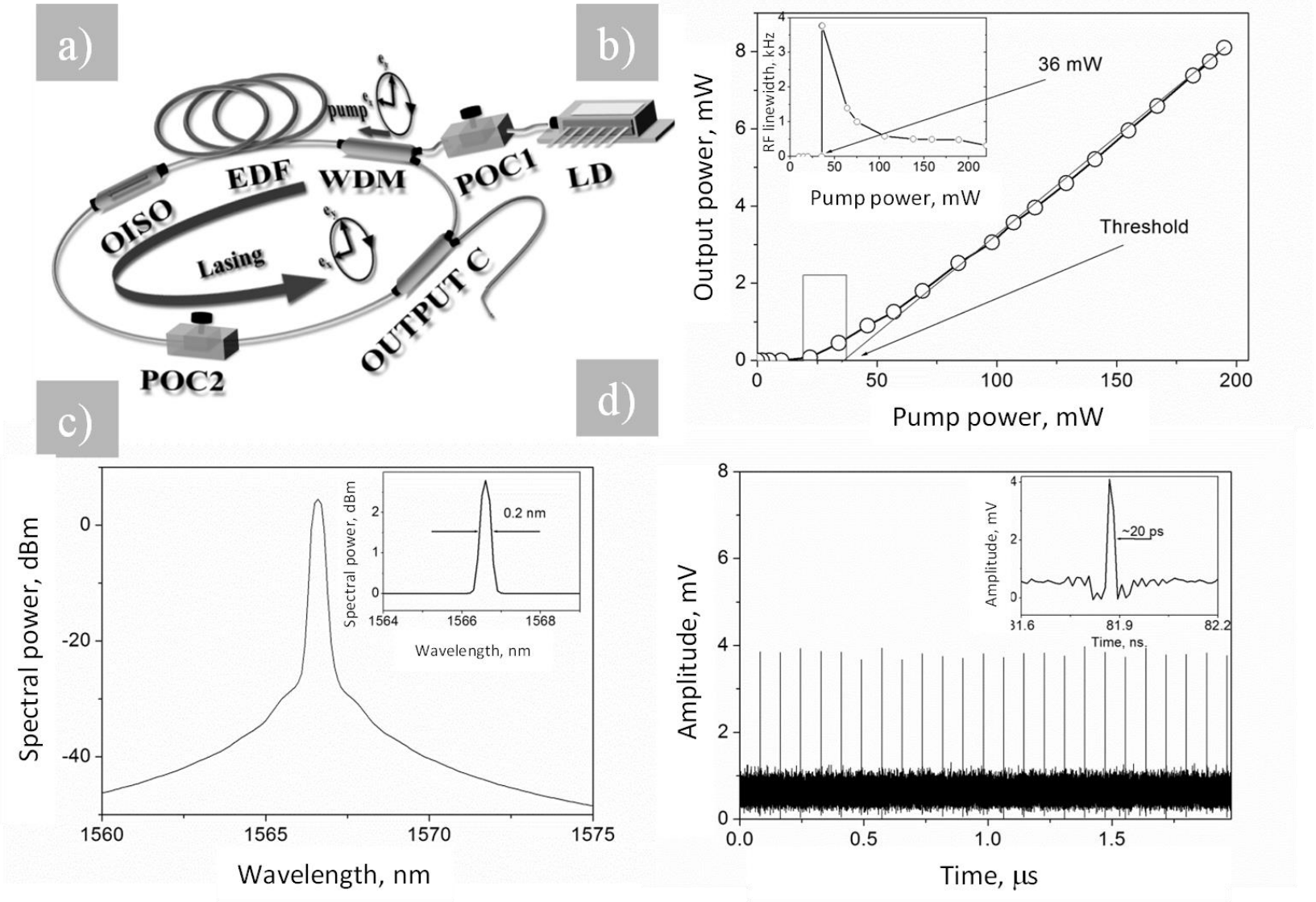
a)
b)
c)
d)
pump
EDF
WDM
POC1
LD
OISO
Lasing
OUTPUT C
POC2
Output power, mW
Pump power, mW
36 mW
Threshold
RF linewidth, kHz
Pump power, mW
Spectral power, dBm
Wavelength, nm
0.2 nm
Amplitude, mV
Time, μs
~20 ps
Time, ns

Fig. 21

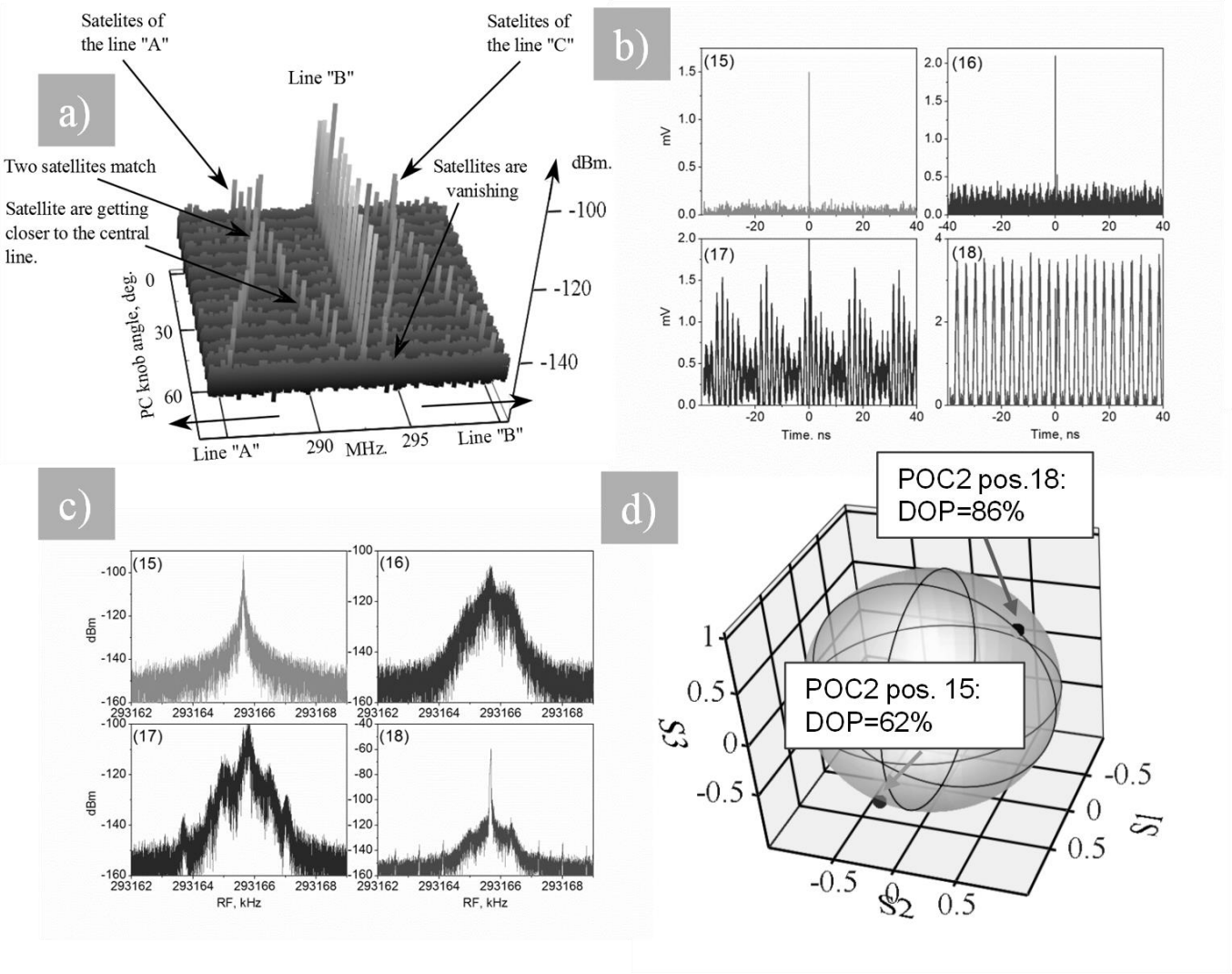
a)
Satelites of the line "A"
Satelites of the line "C"
Line "B"
Two satellites match
Satellite are getting closer to the central line.
Satellites are vanishing
dBm.
-100
-120
-140
PC knob angle, deg.
0
30
60
Line "A"
290
MHz.
295
Line "B"
b)
(15)
(16)
(17)
(18)
mV
Time. ns
c)
(15)
(16)
(17)
(18)
dBm
RF, kHz
d)
POC2 pos.18:
DOP=86%
POC2 pos. 15:
DOP=62%
S3
S1
S2

Fig.22

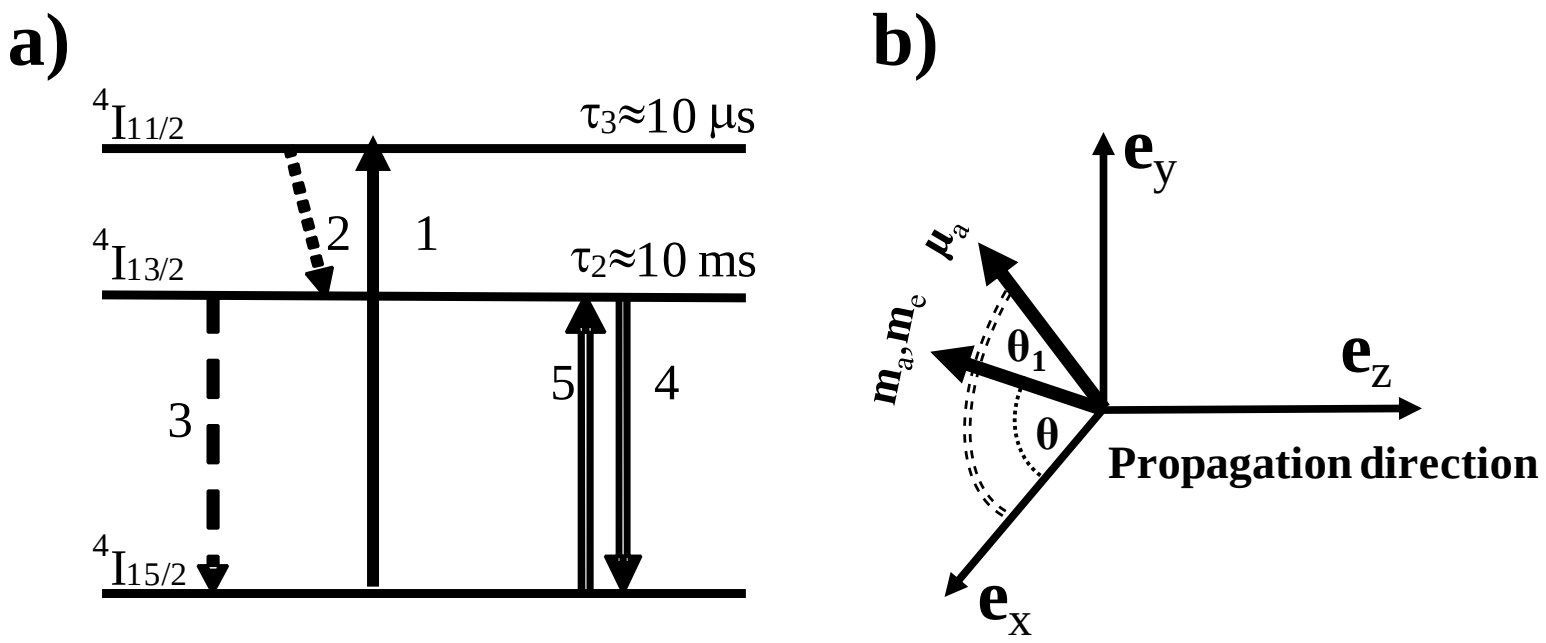
a)
$^4I_{11/2}$
$\tau_3 \approx 10\ \mu s$
$^4I_{13/2}$
$\tau_2 \approx 10\ ms$
$^4I_{15/2}$
1
2
3
4
5
b)
e_y
e_z
e_x
μ_a
m_a, m_e
θ_1
θ
Propagation direction

Fig.23

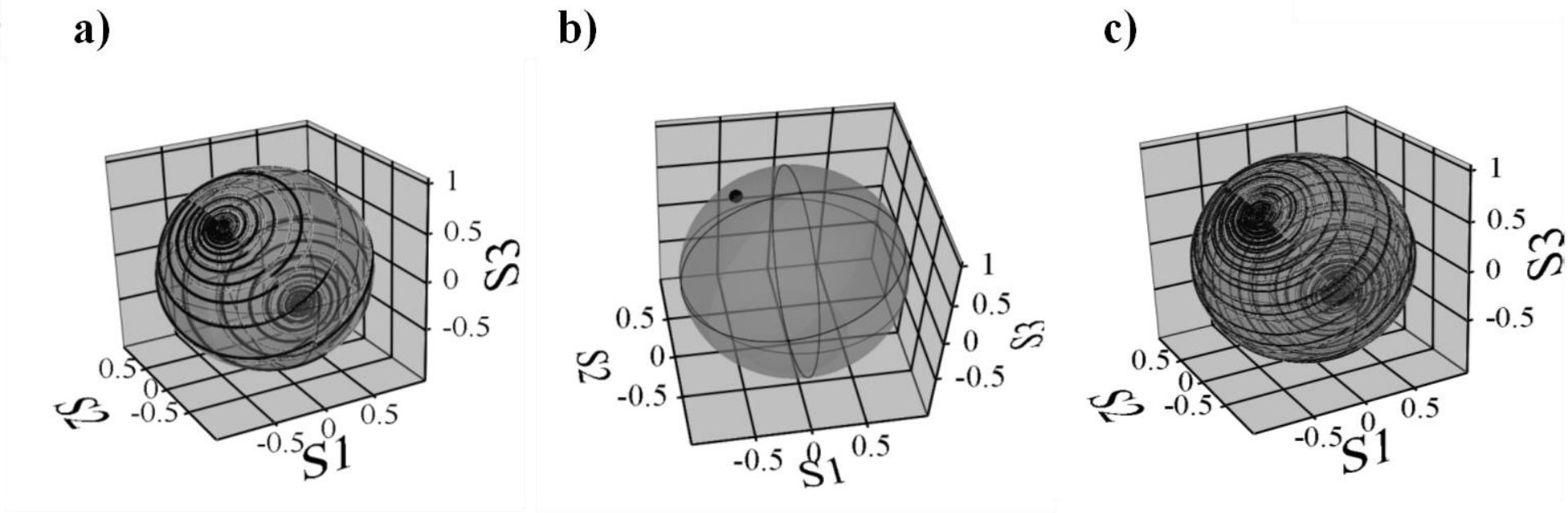

Fig.24

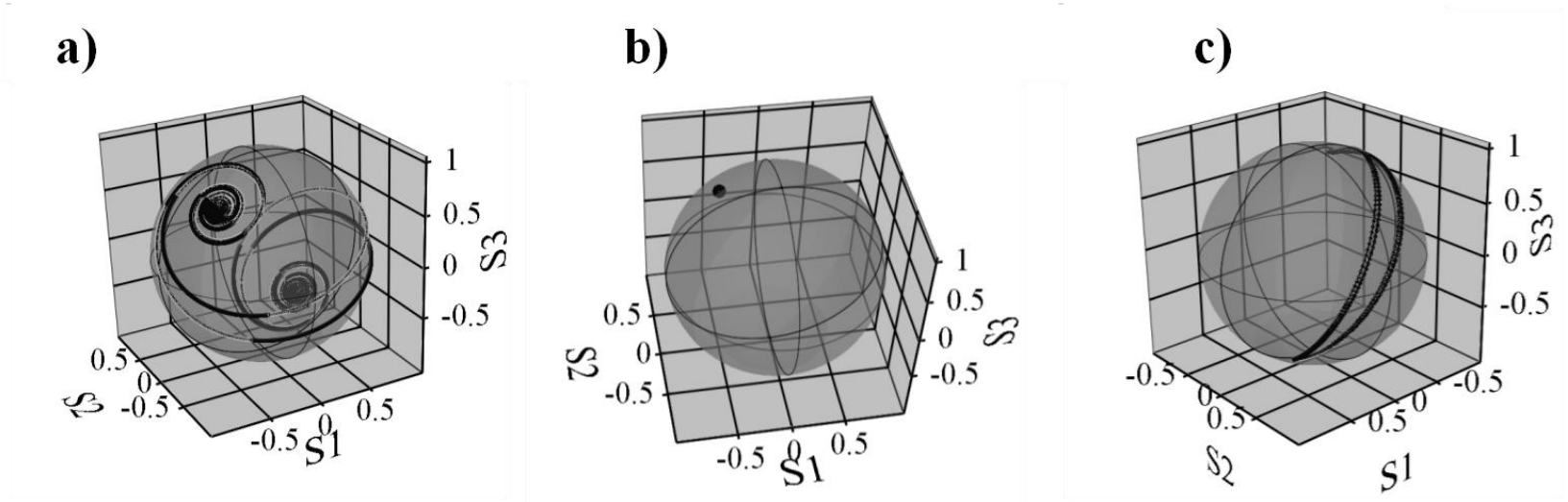

Fig.25

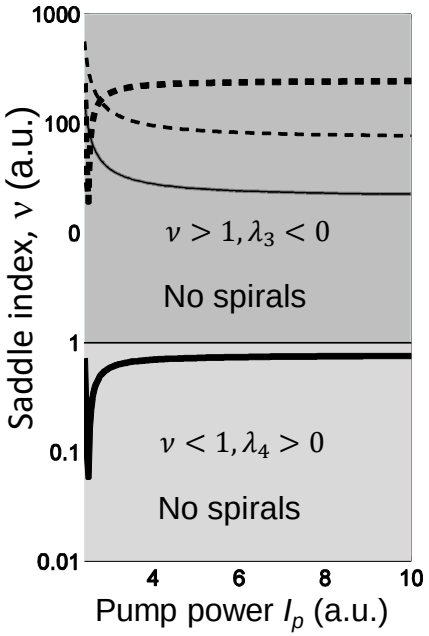
1000
100
0
1
0.1
0.01
Saddle index, ν (a.u.)
ν > 1, λ3 < 0
No spirals
ν < 1, λ4 > 0
No spirals
4
6
8
10
Pump power Ip (a.u.)

Fig. 26

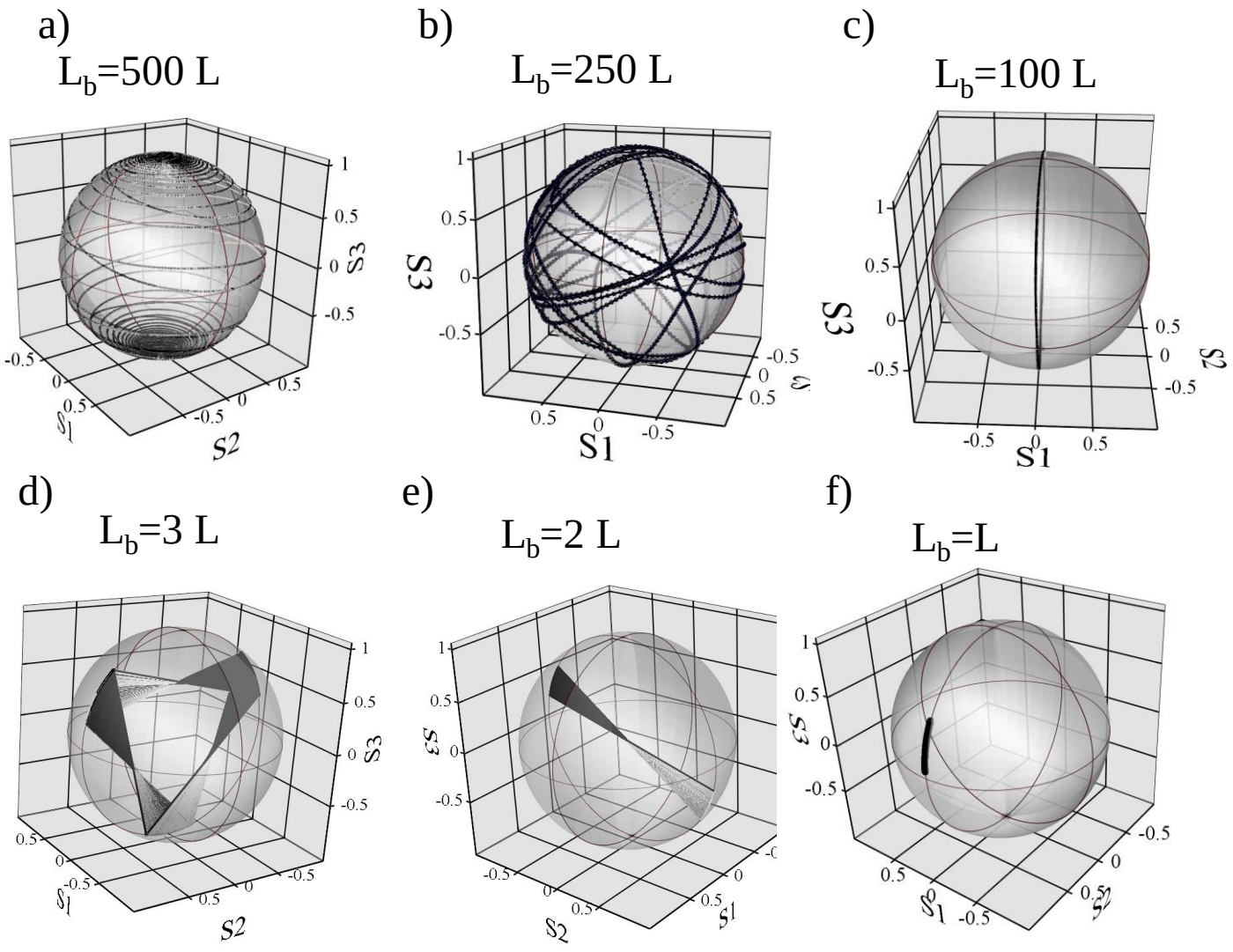

Fig. 27

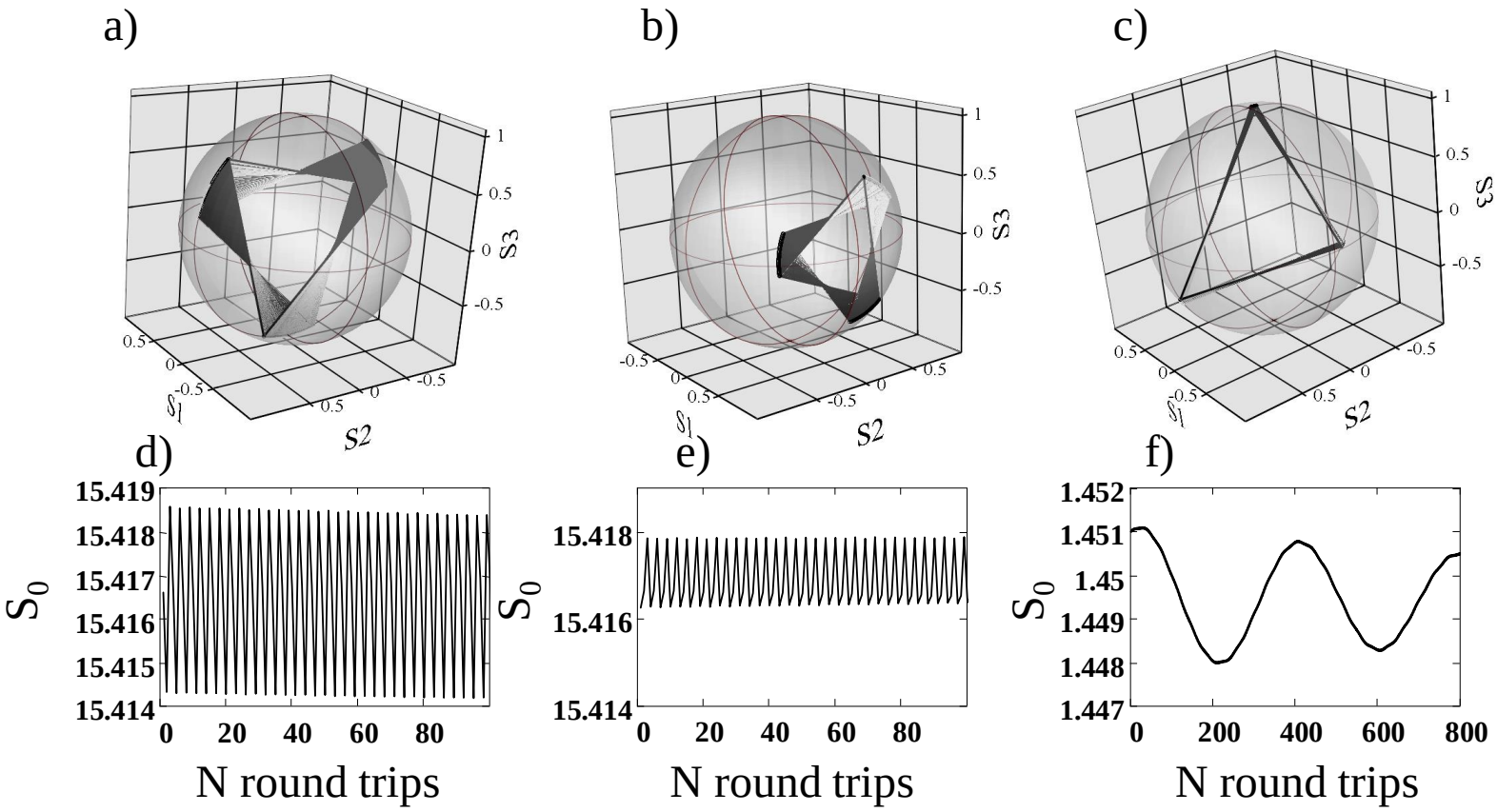
a)
b)
c)
S1
S2
S3
d)
e)
f)
S0
N round trips
15.419
15.418
15.417
15.416
15.415
15.414
1.452
1.451
1.45
1.449
1.448
1.447
0
20
40
60
80
200
400
600
800

Fig. 28

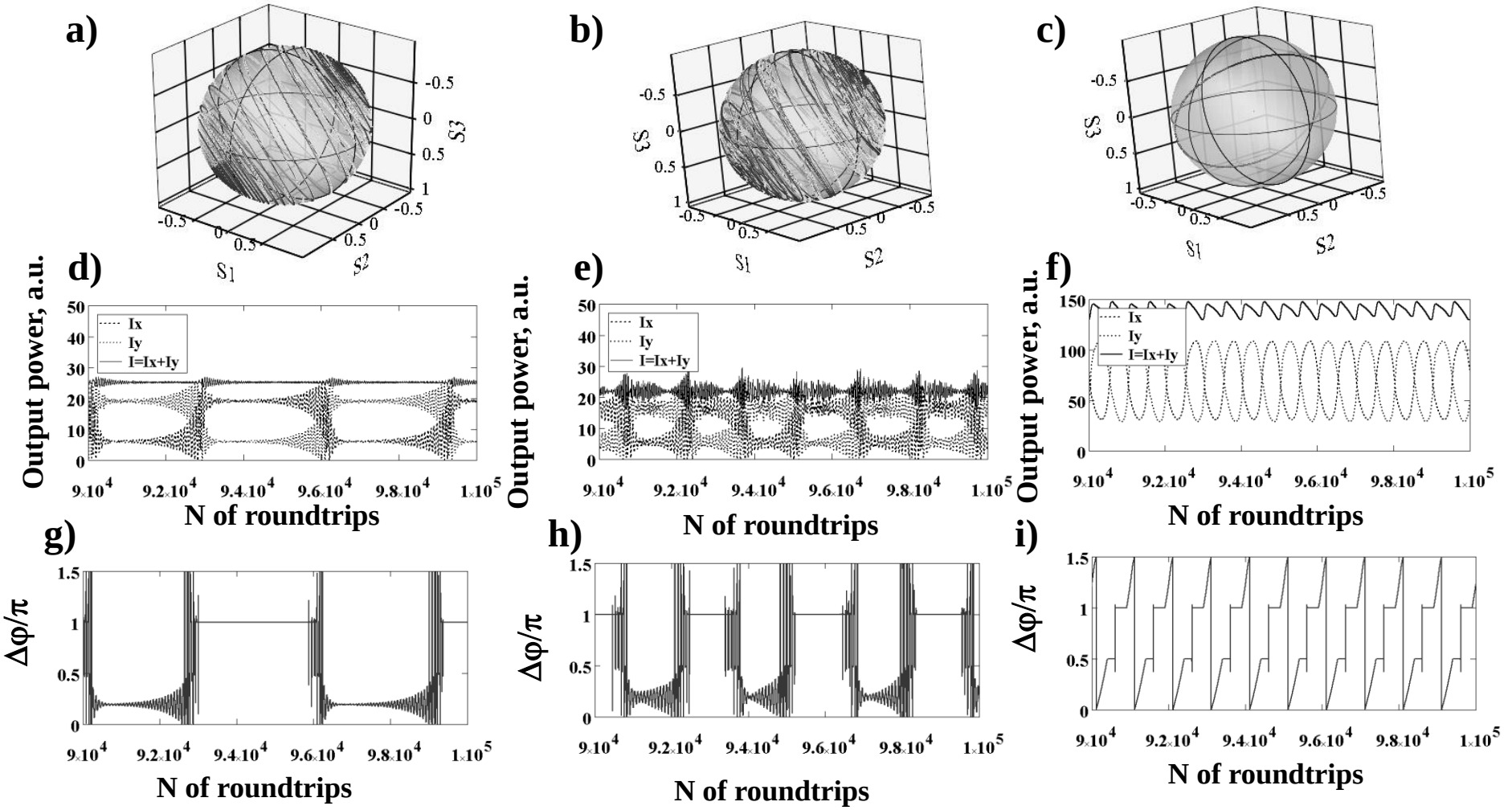
a)
b)
c)
S1
S2
S3
d)
e)
f)
Output power, a.u.
Ix
Iy
I=Ix+Iy
N of roundtrips
g)
h)
i)
Δφ/π
N of roundtrips

Fig. 29

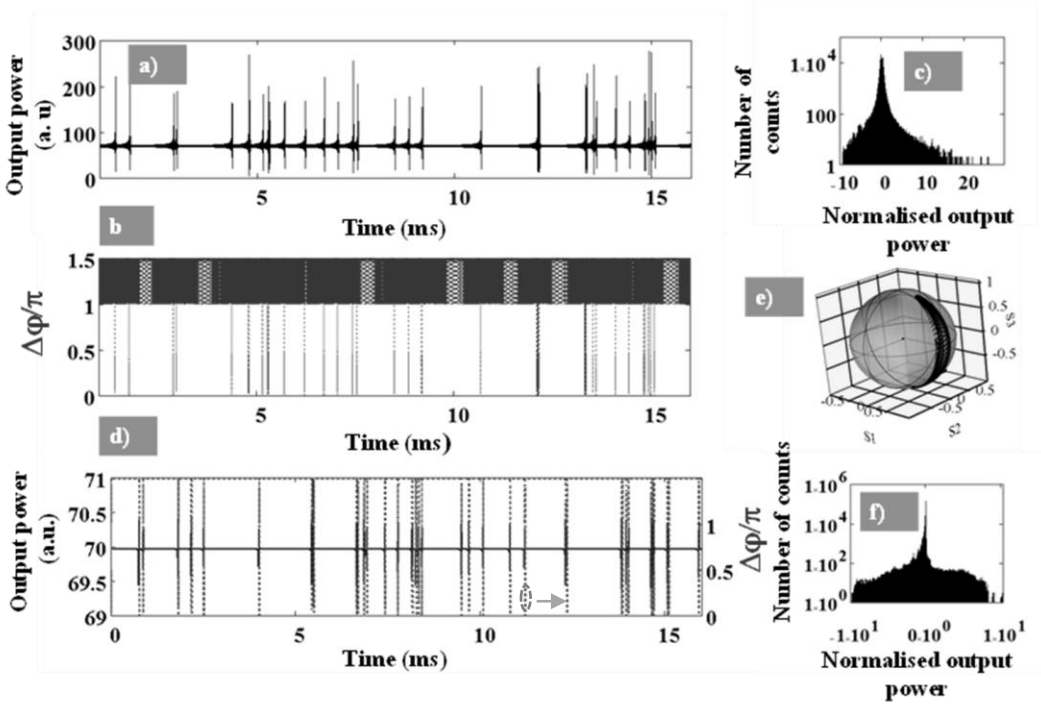
a)
Output power (a. u)
300
200
100
0
5
10
15
Time (ms)
b
Δφ/π
1.5
1
0.5
0
5
10
15
Time (ms)
d)
Output power (a.u.)
71
70.5
70
69.5
69
0
5
10
15
Time (ms)
1
0.5
0
Δφ/π
c)
Number of counts
1.10^4
100
1
-10
0
10
20
Normalised output power
e)
S1
S2
S3
f)
Number of counts
1.10^6
1.10^4
1.10^2
1.10^0
-1.10^1
0.10^0
1.10^1
Normalised output power

Fig. 30

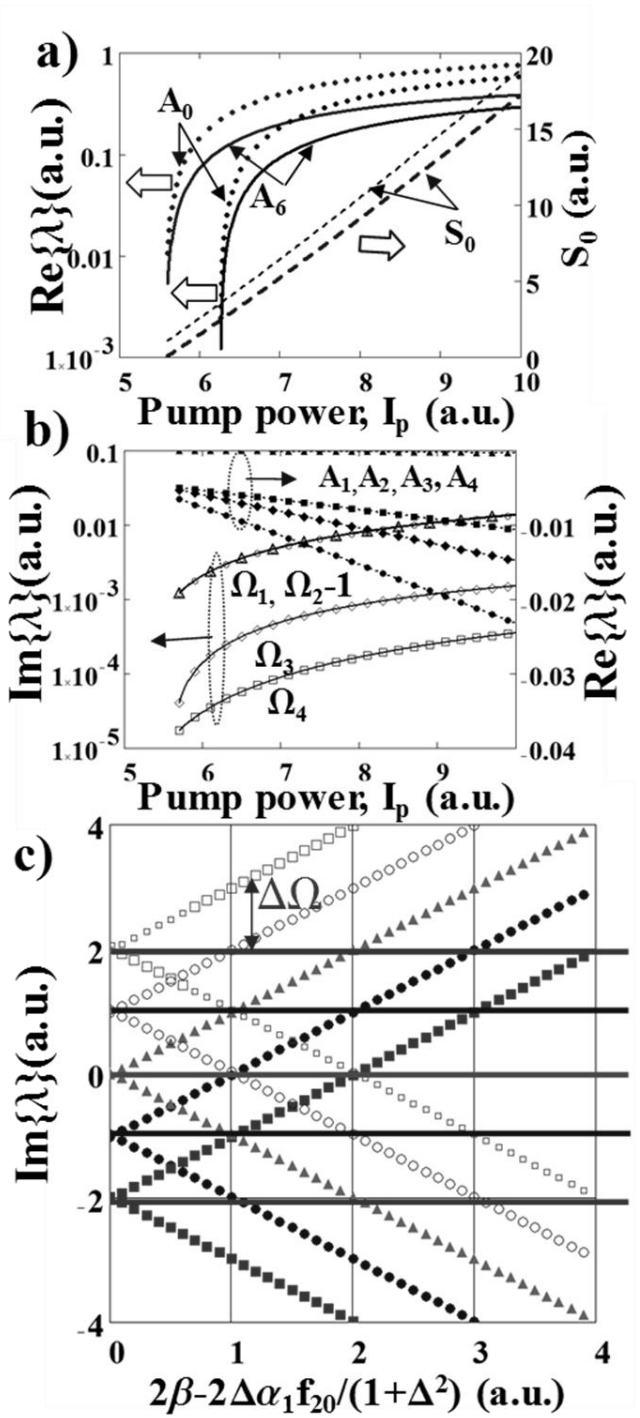
a)
A0
A6
S0
Re{λ}(a.u.)
S0 (a.u.)
Pump power, Ip (a.u.)
b)
A1, A2, A3, A4
Ω1, Ω2-1
Ω3
Ω4
Im{λ}(a.u.)
Re{λ}(a.u.)
Pump power, Ip (a.u.)
c)
ΔΩ
Im{λ}(a.u.)
2β-2Δα1f20/(1+Δ2) (a.u.)

Fig. 31

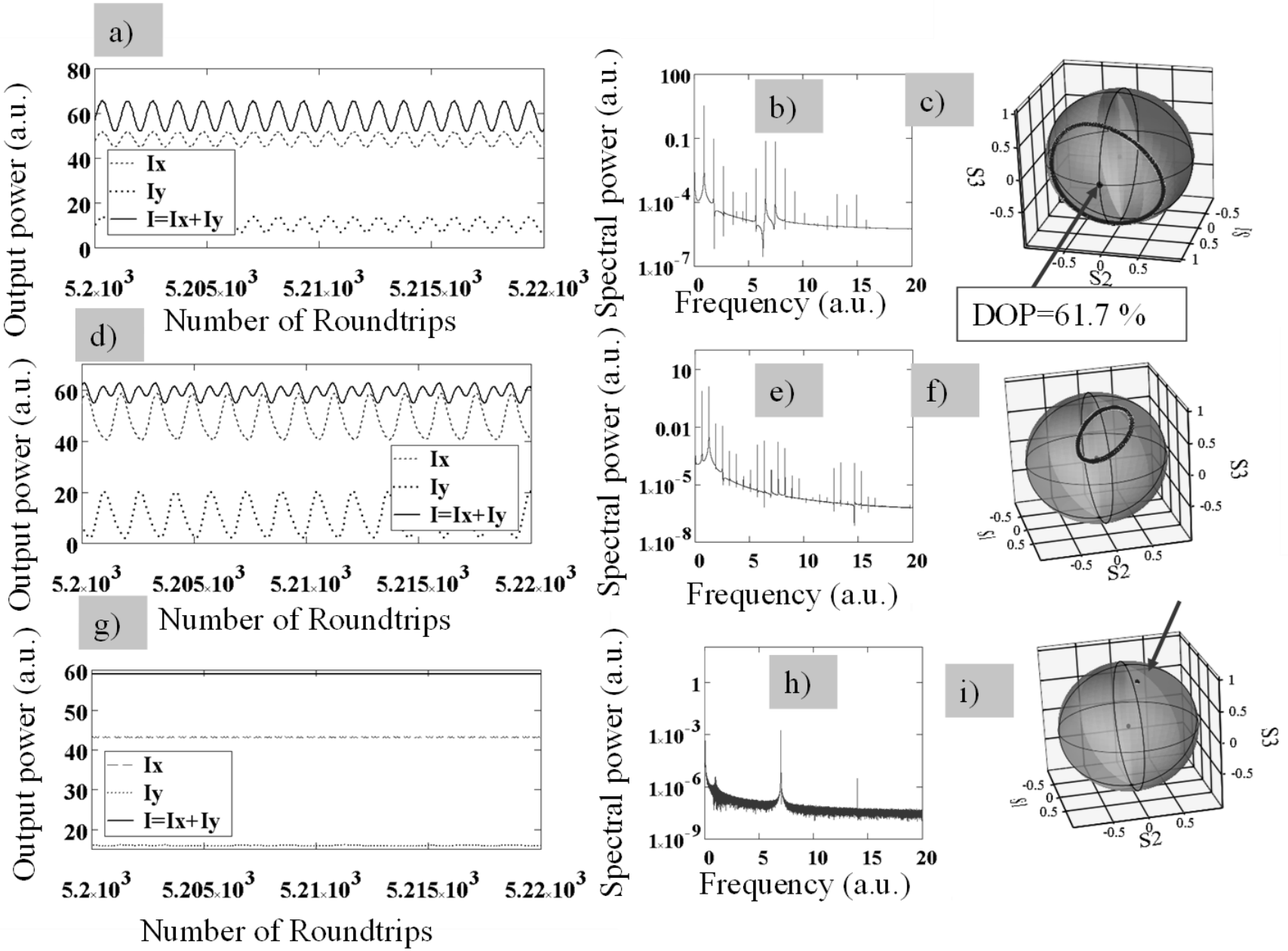
a)
Output power (a.u.)
Ix
Iy
I=Ix+Iy
Number of Roundtrips
b)
Spectral power (a.u.)
Frequency (a.u.)
c)
S1
S2
S3
DOP=61.7 %
d)
Output power (a.u.)
Ix
Iy
I=Ix+Iy
Number of Roundtrips
e)
Spectral power (a.u.)
Frequency (a.u.)
f)
S1
S2
S3
g)
Output power (a.u.)
Ix
Iy
I=Ix+Iy
Number of Roundtrips
h)
Spectral power (a.u.)
Frequency (a.u.)
i)
S1
S2
S3

Fig. 32

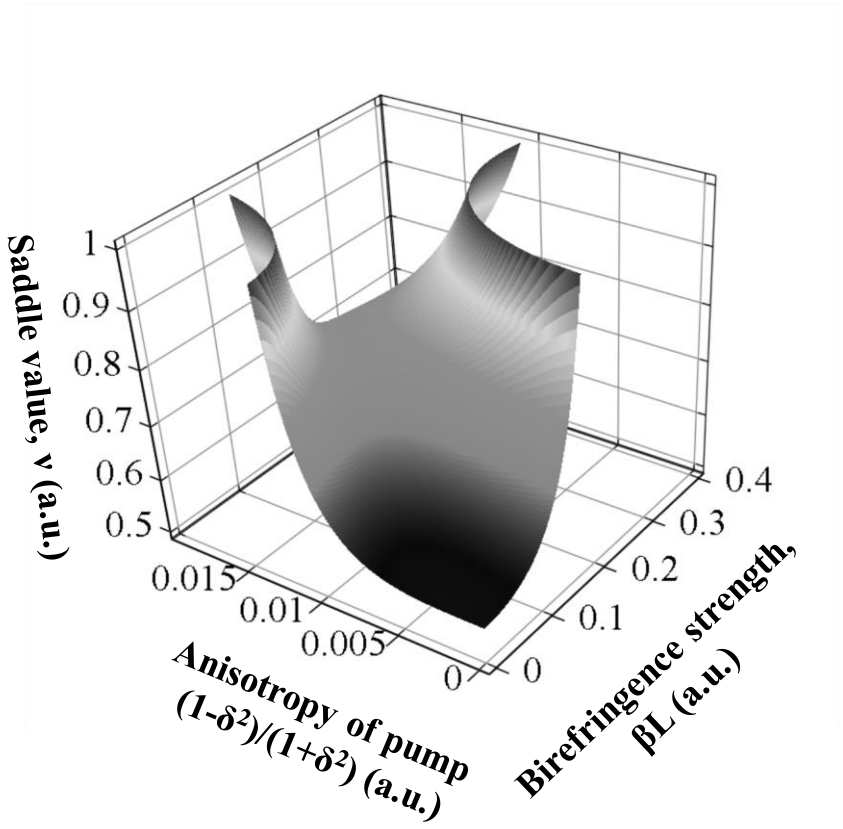
Saddle value, v (a.u.)
1
0.9
0.8
0.7
0.6
0.5
0.015
0.01
0.005
0
Anisotropy of pump
(1-δ²)/(1+δ²) (a.u.)
0
0.1
0.2
0.3
0.4
Birefringence strength,
βL (a.u.)

Fig. 33

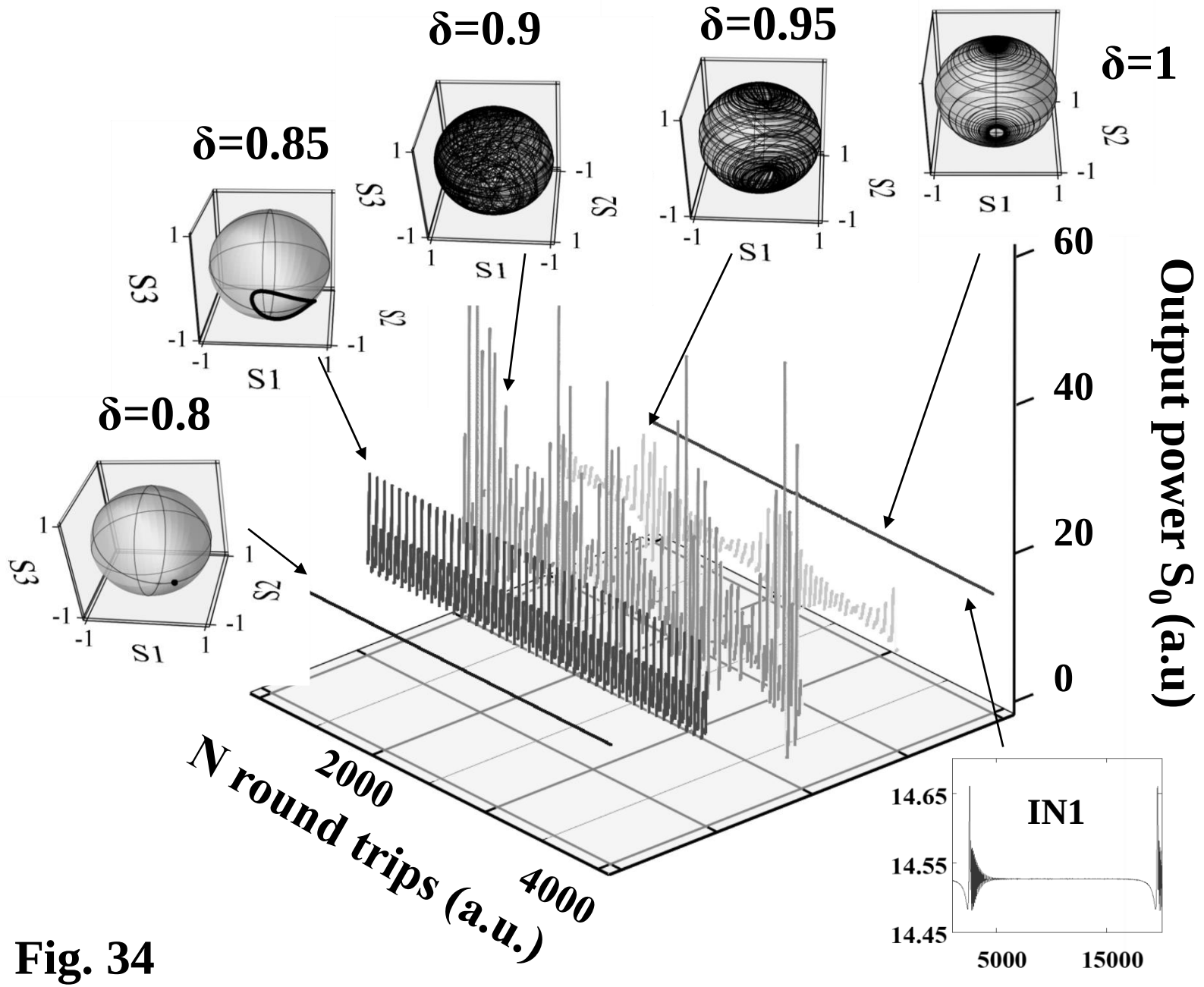
δ=0.8
δ=0.85
δ=0.9
δ=0.95
δ=1
S1
S2
S3
Output power S_0 (a.u)
60
40
20
0
2000
4000
N round trips (a.u.)
IN1
14.65
14.55
14.45
5000
15000

Fig. 34

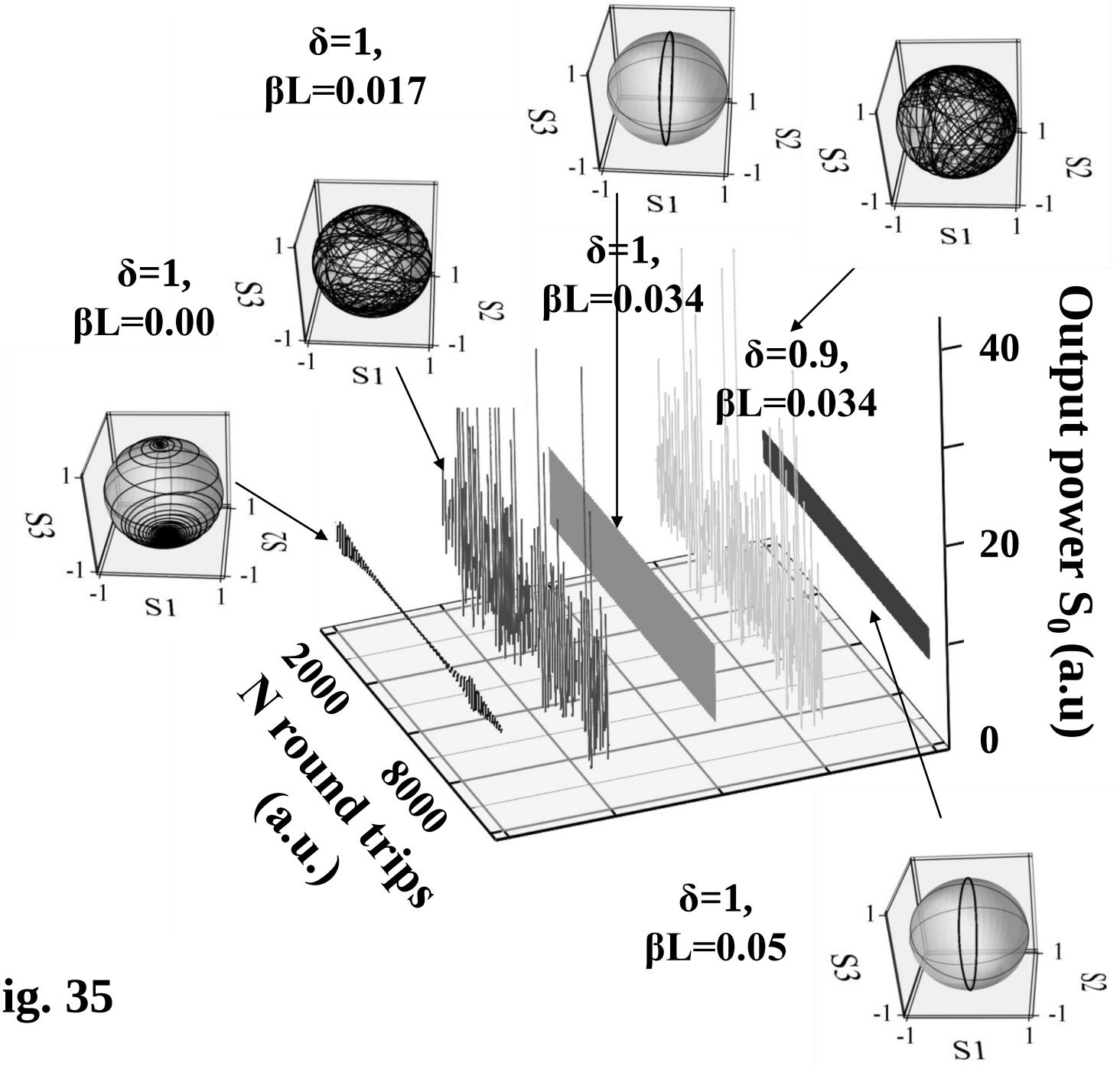
δ=1,
βL=0.017
δ=1,
βL=0.00
δ=1,
βL=0.034
δ=0.9,
βL=0.034
δ=1,
βL=0.05
S1
S2
S3
-1
1
2000
8000
N round trips
(a.u.)
0
20
40
Output power S0 (a.u)

Fig. 35

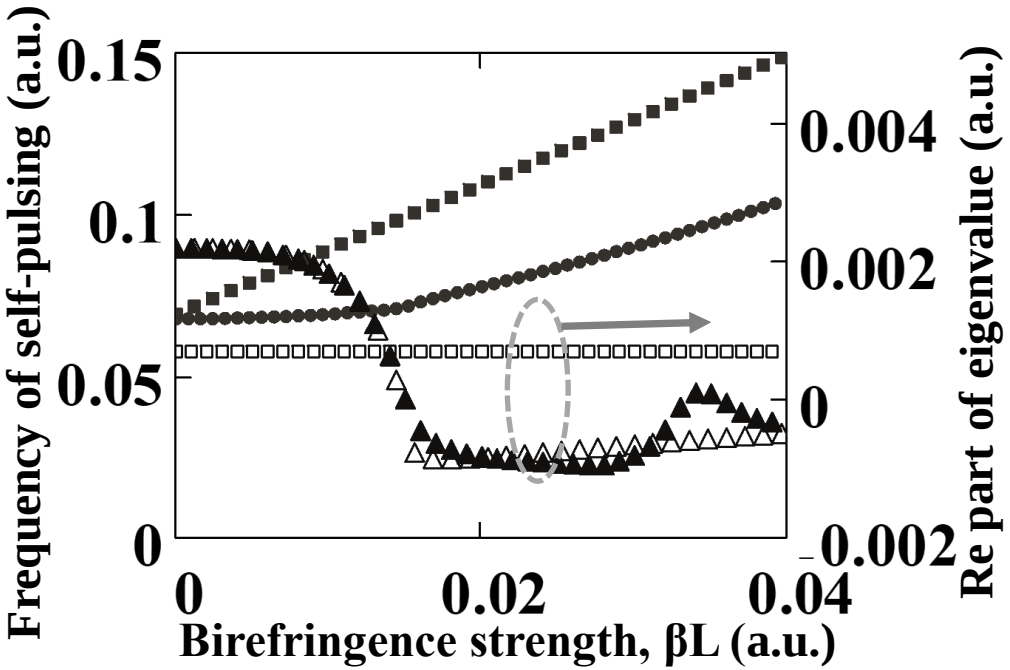
Frequency of self-pulsing (a.u.)
0.15
0.1
0.05
0
0
0.02
0.04
Birefringence strength, βL (a.u.)
0.004
0.002
0
−0.002
Re part of eigenvalue (a.u.)

Fig. 36

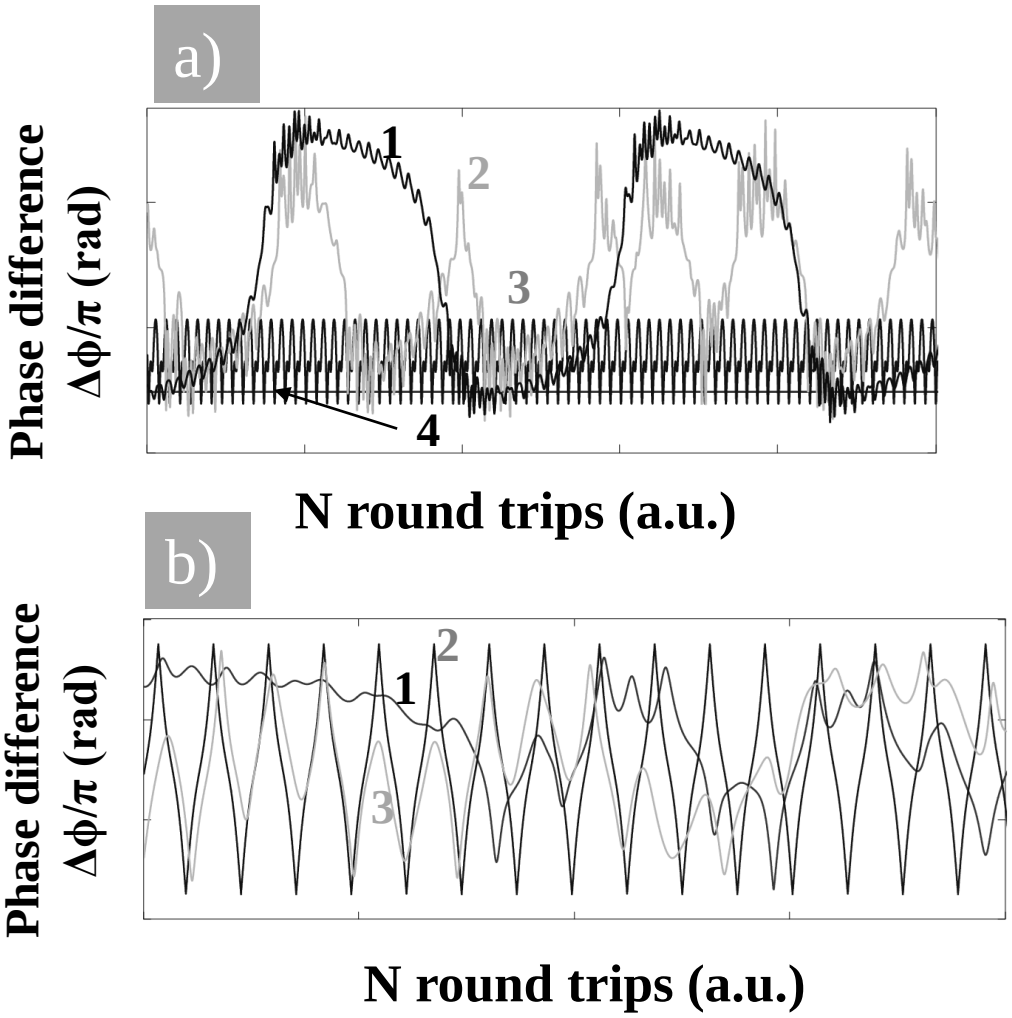
a)
Phase difference
Δϕ/π (rad)
1
2
3
4
N round trips (a.u.)
b)
Phase difference
Δϕ/π (rad)
1
2
3
N round trips (a.u.)

Fig. 37